In Phase III, the cutting equation is combined with an empirical jet spreading equation to determine conditions under which stand-off distance and feed rate (multipass cutting) can be optimized for maximum depth of cut, maximum volume removal of material and maximum cutting efficienty. In Phase IV the cutting equation at very high feed rates is combined with a revised model of material erosion and fracture by liquid drop impact. The combined nondimensional equations are solved and plotted graphically to give theoretical values of the depth of penetration for typical values of pulsed jet lengths and material properties.

ACKNOWLEDGEMENT

The author wishes to express his sincerest appreciation to Dr. M.P. duPlessis, Professor of Mechanical Engineering and Thesis Supervisor, for his continued interest and suggestions throughout the course of the work and in the preparation of the thesis.

TABLE OF CONTENTS

Table of Contents (cont'd.)

Table of Contents (cont'd.)

Table of Contents (cont'd.)

LIST OF TABLES

List of Tables (cont'd.)

List of Tables (cont'd.)

LIST OF FIGURES

List of Figures (cont'd.)

List of Figures (cont'd.)

List of Figures (cont'd.)

List of Figures (cont'd.)

LIST OF SYMBOLS

1. VARIABLES

A_n	cross-sectional area of nozzle exit
A_j	cross-sectional area of jet
A_{vc}	cross-sectional area of jet near vena contracta
A_c	cross-sectional area of cut
b_m	jet radius in the main region
b_c	difference between jet and core radii in initial jet region
C	velocity of longitudinal wave propagation
C_e	velocity of elastic wave propagation
C_p	velocity of plastic wave propagation
C_ℓ	velocity of shock wave in liquids
C_f	coefficient of friction
C_D	Coefficient of discharge (frictional)
C_{DO}	overall coefficient of discharge
C_V	coefficient of velocity
C_{VO}	overall coefficient of velocity
C_c	coefficient of contraction
d_n	nozzle diameter
d_j	jet diameter
d_d	diameter of liquid drop
E	modulus of elasticity
E_o	output jet energy
E_a	available jet energy

e'	difference between dry and wet specific gravities of wood
F_{th}	theoretical hydrodynamic force of jet impact
$F_{th.c}$	theoretical jet force including compressibility effects
F_{ex}	experimental jet force
$F_{s.mech.}$	mechanical force on surface of control volume
F_{sh}	shear resistance force
F_1	jet force
F_2	resistance of material
f	porosity
f_H	hardness coefficient
g	gravitational acceleration
K_x	stand off distance factor
K_s	absolute roughness
K_j	resistance coefficient of submerged jet
L	nondimensional length of a jet pulse
ℓ	length of jet pulse
ℓ_s	length of jet pulse for second stage of penetration
ℓ_δ	length of jet pulse to produce pit depth, δ
ℓ_j	length of jet pulse for second stage of penetration
ℓ_t	total length of jet pulse
M	mach number
mc	moisture content
$\dot{m}$	mass flow rate
$\dot{m}_{in}$	inlet mass flow rate to control volume
$\dot{m}_{ext}$	exit mass flow rate from control volume

N_1, N_2, N_3	nondimensional groups
N_u	feed rate number
N_s	specific gravity number
N_F	Froude number
N_W	Weber number
P	stagnation pressure
P_o	upstream stagnation pressure
P_1	stagnation pressure at nozzle exit
P_m	centerline stagnation pressure of jet
P_a	average stagnation pressure over jet effective width
P_{av}	average stagnation pressure over jet total width
P_c	critical pressure
P_r	reduced pressure
P_L	pressure loss in nozzle
Q	flow rate (volume)
Q_{th}	theoretical flow rate
$Q_{th.c}$	theoretical flow rate including compressibility effects.
Q_{ex}	experimental flow rate
$Q_{ex.p}$	experimental flow rate with polymer
R	ratio of length of jet initial region to nozzle diameter
r_s	ratio of compressive fracture to yield strengths
S	specific gravity
st	surface tension
SE	specific energy
sY	yield strength number (σ_y / P_1)

S_n	strength number
sc	compressive strength number (σ_c/P_1)
T	nondimensional time
u	feed rate
u_H	higher critical feed rate
u_L	lower critical feed rate
V	jet velocity
V_1	jet velocity at nozzle exit
V_2	jet velocity at exit from control volume
V_{th}	theoretical jet velocity
$V_{th.c}$	theoretical jet velocity including compressibility effects
V_{rn}	normal relative velocity
V_c	critical velocity
V_z	jet velocity at distance z from nozzle exit
V_{2r}	control volume relative exit velocity
$v_{A,B,C,F}$	particles velocity in regions A,B,C,F respectively
v_c	critical particle velocity
W	penetration rate = z
w	width of jet
w_e	effective width of jet
w_1	width of cut at the top of kerf
w_2	width of cut at the bottom of kerf
X	stand off distance
X_1	initial stand off distance
X_c	length of jet initial region
$X_{lim.}$	limiting stand off distance
Y	radial distance from jet centerline

Y_c	radius of jet core in jet initial region
Y_{eff}	effective radius of jet
Y_e	expansion coefficient
z	depth of cut
z_o	maximum depth of cut
z_a	cumulative depth of cut
z_t	total depth of cut
z_s	penetration depth during incompressibile stage of impact
$\dot{z}$	penetration rate
$\dot{z}_i$	initial penetration rate
Z	nondimensional depth of cut (z/d_n)
Z_ℓ	liquid acoustic impedance
Z_e	solid acoustic impedance
Z_p	solid plastic impedance = $\rho_m C_p$
γ	specific weight
δ	pit depth due to compressible stage of impact
ΔV	volume of material removed.
ε	strain
$\dot{\varepsilon}$	strain rate
ξ	nondimensional radial distance from jet centerline
η	damping coefficient based on force and deflection rate
η_{ss}	damping coefficient based on stress and strain rate
η_n	nozzle efficiency
η_c	cutting efficiency
θ	curvature angle of kerf
θ_o	angle of incidence
λ	permeability

μ	liquid dynamic viscosity
μ_w	coefficient of friction for cavitational drag
μ_r	internal coefficient of friction
ρ	liquid density
ρ_m	material density
ρ_{P_o}	liquid density at pressure P_o
σ	stress
σ_y	yield strength (compressive)
σ_c	compressive strength
σ_t	tensile strength
σ_s	shear strength
σ_a	mean strength value
σ_{yd}	dynamic yield strength
σ_d	dry wood strength value
σ_u	ultimate dynamic compressive strength
ϕ	pressure decay factor of jet spread
ψ	effective width factor of jet spread

2. CONSTANTS

A_1, A_2, a_1, a_2 , a_3

B_1, B_2, b

C_1, C_2, C_3, c

K , K_0, K_1, K_2

m , m_1

n , n_1

α , α_0, α_1

β , β_1

γ , γ_1

δ δ_1

3. SUBSCRIPTS

c.v	control volume
c.s	control surface
ex	experimental
ext	exit from control volume
in	inlet to control volume.
lim	limiting
mod	modified
th	theoretical
ex.v	exit vertical component from control volume
in.v	inlet vertical component to control volume

INTRODUCTION

Over the last ten years, the development of jet cutting technology has been stimulated by potential applications in mining, rock breaking, cleaning and continuous cutting of relatively soft materials. The advantages of jet cutting over conventional cutting are:

1. There is no tool wear in the ordinary sense; nozzle replacement costs are reasonable.
2. The cut can be started anywhere in the workpiece and complex contour and pattern cutting are relatively simple.
3. Programmed control of the cutting pass can be achieved by numerical control methods.
4. Reaction forces on the workpiece are low relative to those encountered in conventional cutting operations.
5. Dust and heat generation is reduced and mechanical noise can be kept at a low level if the pumping unit is located remotely.
6. Very narrow kerf cuts can be achieved.
7. There is good manoeuverability for cleaning applications.
8. Safety is improved in explosive working environments.

The study of jet cutting encompasses several traditional disciplines such as fluid mechanics, hydraulics, physics and solid mechanics. Past and current work in the U.S.A., U.S.S.R., Japan, U.K., Germany, China, New Zealand, France and Canada can be divided into

three major fields:

1. Development of high pressure equipment for continuous, pulsed, oscillating and rotating high velocity jets which involves problems such as fatigue, sealing and safety of transmission of the high fluid pressure.

2. a-The study of small diameter high velocity liquid jets, their spreading behaviour and the quantitative effect of polymer additives;

   b- The mechanics of deformation of liquid jets (or drops) upon impact on a solid surface and characterization of the lateral flow;

   c- The study of the mechanics of high velocity cavitating jets.

3. The study of fracture mechanics of different materials under the impact of continuous, pulsating or cavitating jets.

Progress in jet cutting technology depends on the successful combination of advances in all three of the above fields. Successful application also requires the ability to optimize the cutting parameters in a particular application and to select those applications where jet cutting has technical and economic advantages over other technologies.

This thesis studies the jet interaction with solid materials. A model of the cutting process is used to develop a jet cutting equation which contains the material properties and jet properties as variables and can be used to optimize the cutting process. The factors con-

trolling the cutting mechanisms for continuous and pulsating jets are also considered. The first chapter reviews existing jet cutting equations. Chapter 2 describes the experimental apparatus used to study nozzle characteristics such as losses, power and efficiency. Systematic analysis of wood cutting data is presented in Chapter 3. The development of the jet cutting penetration model is presented in Chapter 4. In Chapter 5, the effect of stand off distance on depth of cut and volume removal, the analysis of multipass cutting and the effect of feed rate on cutting efficiency are presented. The final chapter presents the theoretical analysis of the effect of feed rate and pulsation on the mode of material fracture.

CHAPTER 1

SURVEY OF JET CUTTING EQUATIONS

The published cutting equations developed to date deal mainly with homogenous brittle materials such as rock and coal, metals such as aluminium, lead, copper and plastics. Little published work is available for fibrous non-homogeneous materials such as wood. Most of the cutting equations rely on characteristic constants that have to be determined experimentally. Table (1.1) summarizes existing cutting equations. Bryan (1) suggested that penetration during cutting results from two separate actions: 1- direct penetration occurs as a result of extreme stresses generated at the point of impact and, 2- secondary penetration or deepening of the kerf after initial penetration. Bryan used dimensional analysis to derive the cutting equation given in Table (1.1) which contains density as the only property defining the material. The equation contains two terms. The first term is related to the volume of the jet and the energy density at the point of impingement and the second term is related to the total energy per unit length of the jet. Two experimental constants have to be determined for each material, so that the equation cannot be extended to conditions and materials beyond the scope of the experimental investigation.

Kinoshita (2) used dimensional analysis to derive the equation in Table (1.1) for rock cutting. He characterized the mode of

fracture by the ratio of the velocity of the water jet (V) to the propagating velocity (C_e) of an elastic wave in the rock (V/C_e). For small values of (V/C_e) penetration is caused mainly by turbulent erosion resulting from the interaction of the back flow with the jet flow. When values of (V/C_e) are high (≥ 0.4), impulsive (water hammer) forces will cause fracture. A strength coefficient f_h and five other characteristics, α_0, α_1, β_1, γ_1, δ_1 (see Table 1.1) are required for each type of rock. Nikonov's (62) equation as correlated by Cooley (3) used material density to distinguish between the cutting of impermeable materials such as metals and plastics, and permeable materials such as rock and coal. Values of two empirical coefficients have been found for a wide range of materials but the equation does not satisfy limiting conditions such as maximum depth of cut at very low feed rates.

Cooley (4) in 1975, presented an improved equation which included additional variables such as the nozzle coefficient of discharge, endurance strength and a stand off distance correction factor.

Based on experimental study of the effect of individual parameters on depth of cut in granite, Matsumoto, et al (5) formulated an equation which is similar in form to Kinoshita's (2) equation. Six experimental constants are needed for each material. The compressive strength was the only material property used to distinguish between types of granite.

The equation proposed by Farmer and Attewell (6) gave a relationship between penetration depth, impact velocity and flow rate which

holds above a certain transitional velocity and uses an experimentally determined crater diameter. The material property used is the velocity of propagation of longitudinal waves in the rock. The equation excludes the effect of other material properties and cutting parameters such as stand off distance. The theory from which the equation is developed assumes that fracture results from momentum transfer of incremental mass quantities which impinge separately on the rock target.

The empirical equation of Frank and Lohn (7) for copper ore does not contain a material property and its application is therefore limited to that material and the particular conditions of the experimental investigation.

Mellor's equation (8), (9) includes nozzle size, stand off distance, pressure and cutting speed. The material properties are included implicitly in a characteristic constant (K) and the depth of cut at zero cutting speed. It satisfies the limiting conditions of zero and maximum cutting depths at infinite and zero cutting speeds respectively, but does not contain an explicit material property.

Zelenim, et al. (10) found that the depth of cut in different rocks is directly proportional to $(P_o - P_c)$ where P_c is a critical pressure which increases with feed rate. The shear strength was used to characterize the different types of rocks.

Crow's equation (11) which is based on the theory of cavitation and brittle fracture of granular material, uses permeability,

porosity, shear strength, a characteristic speed, surface average grain diameter and friction coefficient for cavitation drag. Application of the equation is limited to porous materials and requires experimental determination of several of the equation parameters. Also, the equation predicts a deeper cut when the liquid viscosity is reduced, which is contrary to experimental observations. Another limitation is that the model, which uses Darcy's law to relate pressure gradient in the cutting direction to the feed rate, fails when u equals zero.

The theory of Mohaupt and Burns (12) for unreinforced polymers equates the shear energy of the jet to that required for deformation, fracture and friction loss. Three experimental coefficients and a threshold pressure must be obtained for each material. The equation is limited to certain feed rate ranges and does not satisfy the physical meaning of the assumed energy balance when $u = 0.0$ since constants related to fracture energy and plastic deformation will be eliminated in this case.

Garret, et al. (13) used a hydrodynamic model to express the penetration depth of a jet of length ℓ in mild steel. The equation includes the material density but excludes nozzle or flow parameters such as nozzle size and pressure.

This survey shows that many attempts have been made to obtain experimental and semi-theoretical relationships for the depth of cut in terms of nozzle diameter, jet velocity or pressure, stand off distance, material properties and feed rate. Most of the work

applies to one type of material or a group of materials with similar physical properties. Each equation uses different physical properties and requires characteristic coefficients which have to be determined experimentally over a particular range of operating conditions.

NAME	EQUATION	MATERIAL	TEST CONDITIONS
Bryan (1)*	$z = N_u [a_1 N_S N_F d_n + a_2 N_w d_n]$ $N_S = \frac{I}{s}$, $N_F = \frac{V^2}{g d_n}$, $N_w = \frac{\rho d_n V^2}{\sigma_s}$ $N_u = \sqrt{\frac{V}{u}}$ g = gravitational acceleration	Wood Sugar Maple Red Oak Douglas Fir Poplar	p_o up to 344.5 MPa 50,000 psi d_n 0.076 mm 0.254 mm (0.003" → 0.01") u 0.381 → 1.57 m/min. (15 → 60 inch/min.)
Kinoshita (2)	$\frac{z}{d_n} = \frac{\alpha_o W_w^{\alpha_1}}{W_t^{\beta_1} \cdot (\ell/d_n)^{\gamma_1} \cdot \phi^{\delta_1}}$ $W_w = \frac{d_n V^2}{st}$, $W_t = \frac{d_n u^2}{st}$ $\phi = \frac{f_h d_n}{st}$ st = surface tension of water in air	Rocks Sand Stone Diorite Basalt Granite	p_o 202 → 1721 MPa (29400 → 249900 psi) d_n 0.25 → 0.5 mm (0.0098 → 0.0196 inch) u 1.5 m/sec. (59 inch/sec.)
Cooley (3) and Nikonov (62)	$\frac{z}{d_n} = B_1 \left(\frac{P_o}{\sigma_c} - 0.2\right) \left(\frac{u}{V}\right)^{-m_1}$ B_1, m_1 = material constants	Coal Different materials	Based on published experimental results from many sources.

* Numbers between brackets indicate reference numbers.

Table 1.1 Summary of Cutting Equations

(continued)

NAME	EQUATION	MATERIAL	TEST CONDITIONS
Cooley (4)	$\frac{z}{d_n} = 0.2\ C_D^{1.5} \left[\frac{K_x P_o}{\sigma_e} - 1\right] \sqrt{\frac{\rho v}{\rho_m u}}$ σ_e = endurance strength ≐ 20% - 50% unconfined compressive strength $K_x = 1.12\ (\frac{d_n}{X})^{0.11}$ for $10 < \frac{X}{d_n} < 70$	Rocks Coal Concrete Plastics Ice	The test conditions were general
Matsumoto (5)	$\frac{z}{d_n} = K_2 \frac{d_n^{2\delta_2}\ V^{3\delta_2}}{X^{\beta_2}\ u^{\delta_2}} \cdot \frac{1}{\sigma_c^{E_2}}$ X = stand-off distance. δ_2, β_2, γ_2, E_2, K_2 are material constants.	Granite	Submerged jet $10 < X < 100$ mm. $5 < u < 100$ mm/sec. $0.69 < d_n < 1.03$ mm. $325 < V < 700$ m/sec. $400 < \sigma_e < 1570$ Kg/cm^2

Table 1.1 Continued

NAME	EQUATION	MATERIAL	TEST CONDITIONS
Farmer (6)	$\dot{z} = \Sigma \frac{k}{A_j} \dot{m} (V - V_c)$ K = constant, A_j = jet area V_c = critical velocity $z = K d_c (\frac{V}{C})^n$ | $V > 300$ m/sec. C = longitudinal wave velocity d_c = diameter of crater $\dot{z} = (\frac{d}{t}) = K'Q$ $V > 500$ m/sec. $\dot{z}$ = average rate of penetration Q = jet flow rate	Rocks Carrara Marble Annhydrite Non-igneous rocks	$P_o \rightarrow V \rightarrow$ 500 m/sec. (1640 fps) $d_n \rightarrow$ 1.19 → 4.7 mm (0.0468 → 0.185 inch)
N. Frank P.D. Lohn (7)	$\frac{z}{d_n} = C_o [\frac{V}{u}]^{K=0.2}$, $C_o = [\frac{P_o}{1131}]^{0.7}$ P in bars	Copper Ore	$P_o \rightarrow$ 552 MPa (800000 psi) Q → 88 ml/sec. $d_n \rightarrow$ 0.02 cm (0.078 inch) $u \rightarrow$ 1.1 → 16.9 cm/sec. (0.43 → 6.6 inch/sec.)

Table 1.1 - Continued

NAME	EQUATION	MATERIAL	TEST CONDITIONS
Mellor (8), (9)	$z = z_o\left[1 - e^{\frac{KP_o^2 d_n}{u}}\right]$ $z_o = 1200\, d_n - X$ X = stand off distance z = depth of cut at feed rate u z_o = depth of cut when u = 0.0	Ice	P_o 17.2 MPa, 689 MPa 2500 100000 psi d_n 0.2 0.58 mm 0.008 0.023 inch u 0.2 76 mm/min. 0.66 250 fpm
Zelenin (10)	$z = d_n \frac{P_o - P_c}{\sigma_s} f(u)$ P_c = critical P, $f(u) = u^{-0.33}$	Granite Limestone Marble	P_o 202 MPa (29400 psi) V 454 m/sec. (1500 fps)
Crow (11)	$z = 2\mu_w \frac{d_n P_o}{\sigma_s} \int_0^{\theta_o} \frac{e^{\mu w (\theta - \theta_o)} \sin\theta}{1 + (\frac{u}{c}) \sin\theta} d\theta$ $c = \frac{\lambda \sigma_s}{\mu f \mu_r d_g}$ λ = permeability σ_s = shear stress μ = viscosity f = porosity θ = local cutting angle d_g = grain dia.	Wilkeson Sand Stone	P_o 138 MPa d_n 0.76 mm (0.0299 inch)

Table 1.1 Continued

NAME	EQUATION	MATERIAL	TEST CONDITIONS
Mohaupt and Burns (12)	$z = \frac{P_o - P_c}{(\frac{C_1}{d_n}) + (C_2\, d_n + C_3)\,\frac{u}{Q}}$ C_1 related to friction between jet and material C_2 related to fracture energy absorbed C_3 related to plastic deformation Q flow rate	Plexiglass Delrin Polycarbonate	$P_o \rightarrow$ 414 MPa (60,000 psi) $V \rightarrow 6.6*10^4$ cm/sec. (2100 fps) $d_n \rightarrow$ 0.076 mm → 0.178 mm (0.003 → 0.007 inch) $u \rightarrow$ 1 → 4 cm/sec. (0.39 → 1.57 inch/sec.)
Garrett (13)	$z = \ell\sqrt{\frac{\rho}{\rho_m}}$ ℓ = length of the jet ρ_m = material density	Mild Steel	$V \rightarrow$ 9000 m/sec. (29500 fps)

Table 1.1 Continued

CHAPTER 2

EXPERIMENTAL EQUIPMENT, MEASUREMENTS, CHARACTERISTICS AND EXPERIMENTAL DESIGN

2.1 EXPERIMENTAL EQUIPMENT AND MEASUREMENTS

The purpose of the experimental investigation was to study the nozzle and jet behaviour and to obtain cutting test data.

2.1.1 Equipment

The test equipment consists of four air driven pumps that are connected in parallel to provide flow rates up to 13.5 cc/sec. (0.82 in^3/sec.) at a pressure of 207 MPa (30 Ksi) with a 0.203 mm (0.008 inch) diameter nozzle. The pumps are manufactured by the Haskel and Supply Co. Each pump is a single acting reciprocating piston pump driven by a pilot controlled continuously cycling double acting air cylinder. The air requirement is about 28 standard liters/sec. (60 scfm) when delivering 4 cc/sec. (0.25 in^3/sec.) of water at 276 MPa (40 Ksi). Nozzles with sapphire orifices from 0.076 mm (0.003 inch) to 0.203 mm (0.008 inch) diameter were used. Tests were conducted with water containing 0.25% polyethyleneoxide (polyox). The feed table is driven either pneumatically for high feed rates (greater than 1 m/sec.) or mechanically with a motor and leed screw for slower feed rates (0.2 - 4 cm/sec.). The experimental apparatus is shown in Figs. 2.1 and 2.2. Fig. 2.3 is a schematic diagram of the system. A 0.45 liter (27.5 in^3) accumulator dampens the

1. Pump
2. Nozzle
3. Pneumatic Feed Table
4. Mechanical Feed Table
5. Water Tank
6. Accumulator
7. Limit Sensor
8. Rotameter
9. Transducer

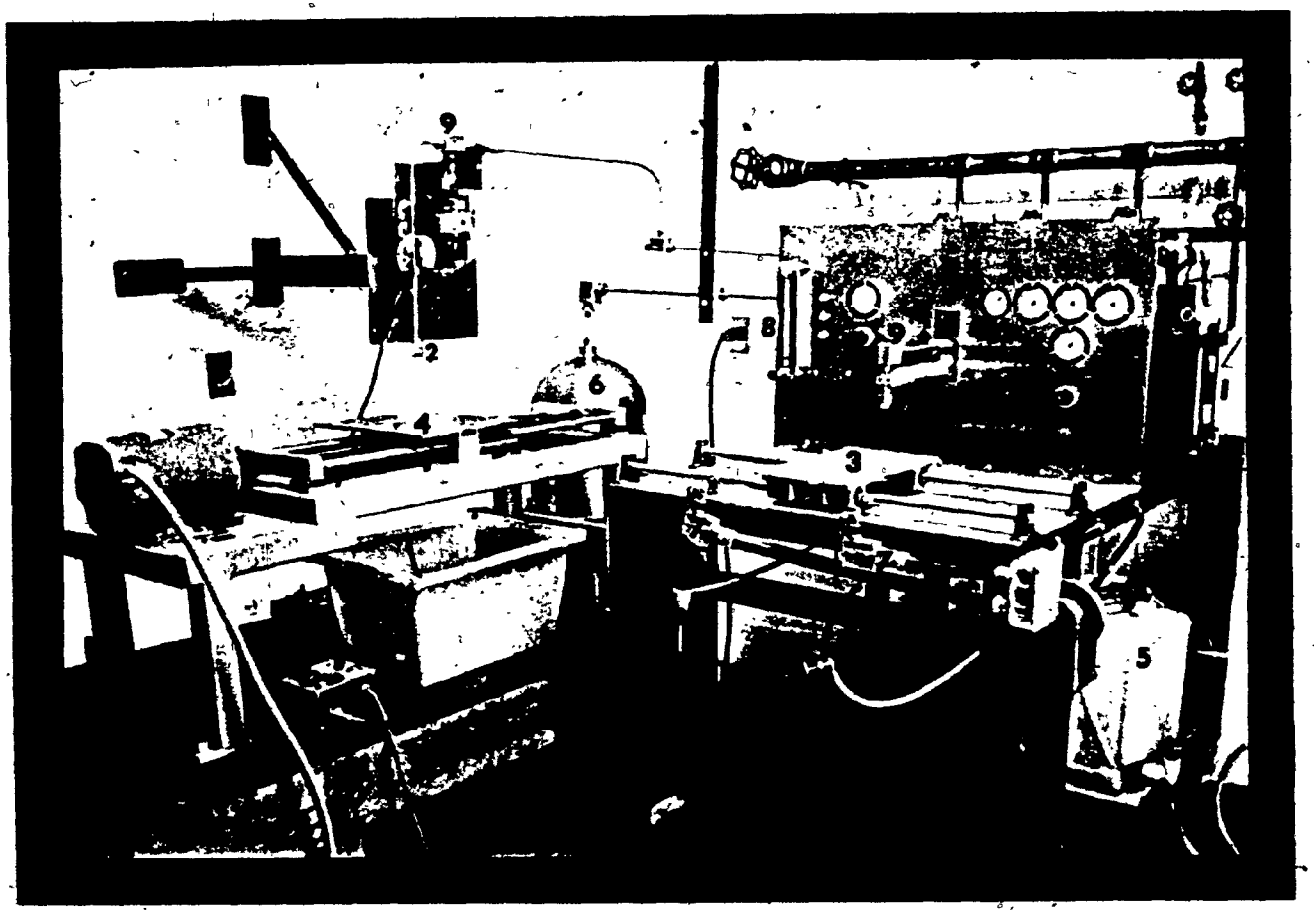

Fig. 2.1 Experimental Equipment.

1. Pump
2. High Pressure Water Line
3. Air Valves
4. Inlet Air Pressure Indicators
5. Feed Rate Control Knob
6. Rotameter
7. Inlet Water Pressure Control Knob

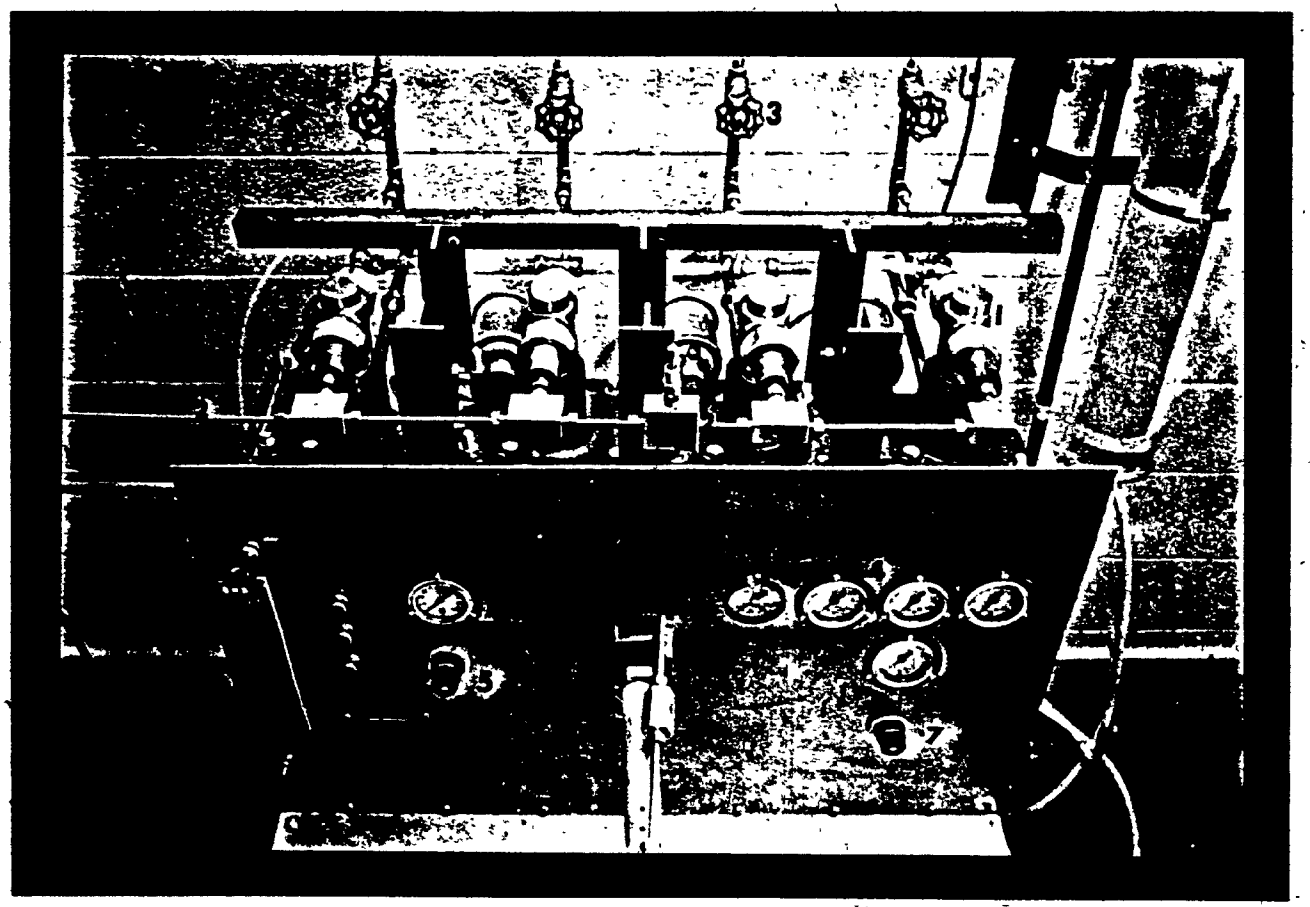

Fig. 2.2 Top View of Pumps Arrangement

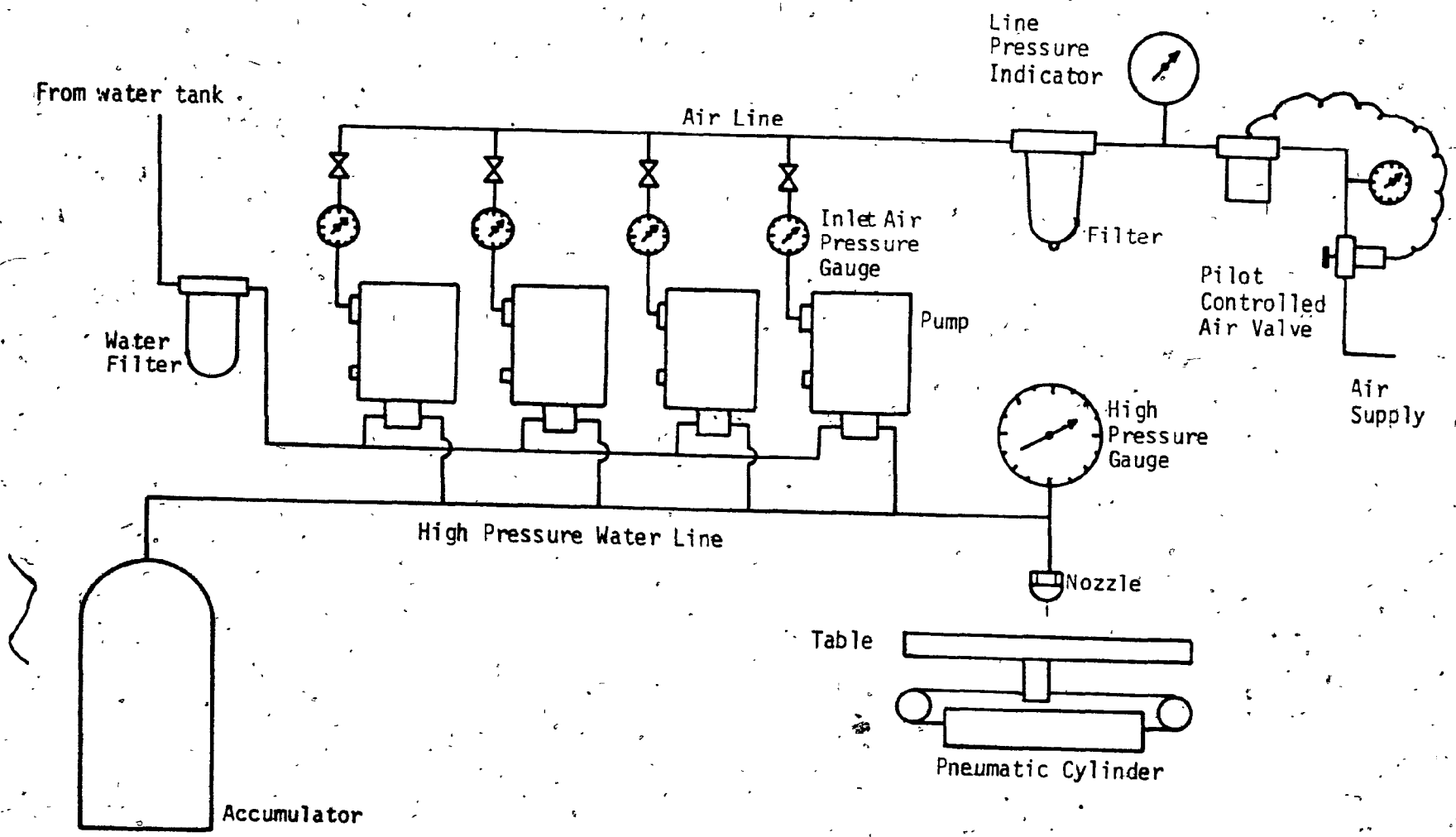

Fig. 2.3 Schematic Diagram of the Experimental Equipment.

pressure fluctuations of the reciprocating pumps. The nozzles were provided by the High Speed Aerodynamics Laboratory of the National Research Council of Canada. The nozzle holder and sapphire orifice dimensions are shown in Fig. 2.4.

2.1.2 Measurement of Cutting Parameters

a- Feed Rate. The speed of the pneumatically driven table is measured by electrical switches connected to a timer, the switches are set one foot apart and the timer has an accuracy of 0.01 sec. The linear speed of the mechanically driven table is set by the electric motor speed control dial which is calibrated accurately over a wide range of feed rates.

b - Pressure Measurement. A statically calibrated high pressure dial gauge is used to measure the nozzle supply pressure. A check of the steadiness of pressure supply by a Kistler high pressure transducer (Model 607-A with a dual amplifier Model 504-E) on an oscilloscope showed a maximum deviation of ± .35 MPa (52 psi).

c - Flow Measurement. A calibrated rotameter connected on the low pressure side of the pumps in the water line gives direct flow readings. In tests where more accurate flow measurements are required, the water volume drawn from the water supply tank is measured over time periods of several minutes.

d - Orifice Diameter. A measuring microscope with 100 to 500 magnification mounted on a vernier scale was used to check the

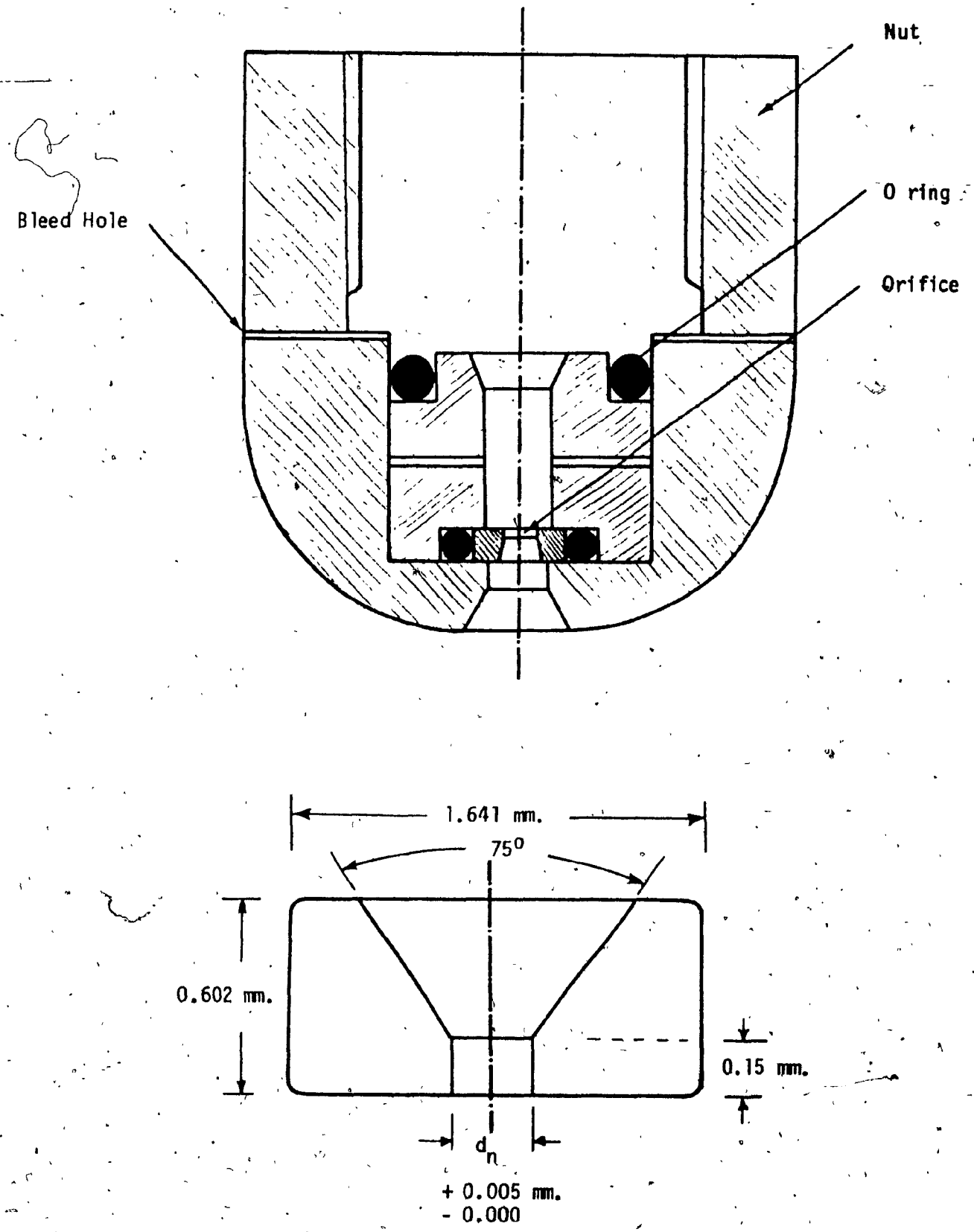

Fig. 2.4 The Nozzle Holder and the Sapphire Nozzle Dimensions

orifice diameters of sapphires in two perpendicular directions. The manufacturing tolerance for the orifices is:

+ 0.0002 inch

- 0.0000 inch.

e - Depth of Cut. Cutting tests were carried out with different types of wood. These results together with published results of cutting tests with a wide range of other materials were used in the theoretical analysis. For each sample of wood, the depth of cut was measured at four different locations along the cut using a measuring magnifying lens equipped with a vernier scale. This involved mechanically cutting each sample in three pieces after the tests and measuring the depth at the edges of each cut. This method was adopted after several other depth gauge methods were tried with less satisfactory results.

f - Force Measurement. Direct measurement of the force exerted by the jet on a target was used to calculate the jet contraction coefficient in the following section. A Kistler force transducer (Model 931-A) with a charge amplifier and oscilloscope were used. Force measurements could be obtained with an accuracy of ±0.044 Newton. A 2.5 cm diameter target disc was mounted on the transducer. The transducer and target disc assembly were clamped to the table with the disc surface exactly normal to the jet axis.

g - Polymer Characteristics. The effect of a polymer additive on the nozzle performance was investigated for only one type

of polymer and one concentration was used. Details are as follows:

Polymer commercial name:	Polyox
Polymer chemical name:	Polyethyleneoxide
Grade:	Coagulant
Solution concentration:	0.25%
Kinematic viscosity: at 15°C	2.5×10^{-5} m^2/sec.

h - Width of the Jet. The jet diameters at distances greater than 25 mm. were measured from enlarged photographs for different nozzle sizes.

2.2 INVESTIGATION OF NOZZLE AND JET CHARACTERISTICS

The purpose of the investigation is to determine nozzle efficiency and jet spreading characteristics and the effect of the polymer additive. The efficiency with which a particular nozzle converts pressure energy to kinetic energy can be expressed as a nozzle discharge coefficient which is affected by viscosity, compressibility and polymer additives. The literature contains little quantitative information on these effects at pressures above 60 MPa (10 Ksi). Since this investigation is only indirectly related to the objective of the thesis, a limited number of experiments were conducted to obtain the necessary quantitative information on specific energy, stand off distance and multipass cutting. These equations are used in the theoretical analysis or are predicted from the theoretical cutting equation.

The experimental investigation consisted of the following:

Group (1): Flow rates and jet thrusts were measured for three different nozzle sizes at different pressures using water with and without polymer additive. The measured quantities are compared with calculations including and excluding compressibility and the results are presented as nondimensional plots of discharge coefficient versus Reynold's number.

Group (2): The width of the jet at different stand off distances were measured for three nozzle sizes at a supply pressure of 103.5 MPa (15000 psi). Experimental results for Group (1) are shown in Figs. 2.7, 2.8, 2.9, 2.14 and 2.15 and for Group (2) in Fig. 2.18.

2.2.1 Nozzle Flow Coefficients

The nozzle assembly used for the tests is shown in Fig. 2.4. The sapphire orifice is mounted with the conical side facing downstream, so that flow occurs through a sharp edge orifice. For incompressible frictionless flow with zero approach velocity, the theoretical velocity and flow at the vena contract are

$$V_{th} = \sqrt{2P_o/\rho} \tag{2.1}$$

$$Q_{th} = A_{vc}\sqrt{2P_o/\rho} = C_c\, A_n\sqrt{2P_o/\rho} \tag{2.2}$$

where ρ is the water density at standard conditions, A_{vc} is the vena contracta area and C_c is the contraction coefficient. The actual flow is less than the theoretical flow, and coefficients of velocity and discharge are used to relate experimental to theoretical values

$$V_{ex} = C_{vo}\sqrt{2P_o/\rho} \tag{2.3}$$

$$Q_{ex} = C_{Do}\sqrt{2P_o/\rho} \cdot A_{vc} \tag{2.4}$$

The overall coefficients of velocity (C_{vo}) and discharge ($C_{D}o$) can be expressed in terms of frictional coefficients (C_v, C_D for velocity and discharge respectively) and a compressibility coefficient (Y_e) which is frequently called an expansion coefficient. Eqns. (2.3) and (2.4) then take the forms

$$V_{ex} = C_v \cdot Y_e \sqrt{2P_o/\rho} \tag{2.5}$$

$$Q_{ex} = C_D \cdot Y_e \sqrt{2P_o/\rho} \cdot A_{vc} \tag{2.6}$$

The expansion factor Y_e can be eliminated from the equations if the compressibility is taken into account in calculating the theoretical velocity. Bernoulli's equation for inviscid steady compressible flow is

$$\frac{V^2}{2} + \int \frac{\partial P}{\rho} = \text{constant} \tag{2.7}$$

From Eqn. (2.7), the theoretical compressible velocity $V_{th.c.}$ can be determined if the equation of state $\rho = f(P)$ of water is given. The literature contains several empirical forms for the equation of state.

Bryan (1) used the relationship:

$$^{\rho}P_o = \frac{100\ \rho}{100 - 0.312\ P_r - 0.00187\ P_r^2} \tag{2.8}$$

$^{\rho}P_o$ = density at pressure P_o

$P_r = P_o/1000$, P_o in psi

Solving Eqns. (2.7) and (2.8) gives

$$V_{th.c.}\ (fps) = \sqrt{1485(100P_r - 0.0156\ P_r^2 - 0.0062\ P_r^3} \qquad (2.9)$$

In Ref. (5), another form of the equation of state is

$$\gamma = 318.6 \quad (\frac{P_o}{14.5} + 2942)^{1/7} \qquad (2.10)$$

γ = specific weight in kg/m^3

P_o = supply pressure in psi

The theoretical compressible velocity calculated from Eqns. (2.10) and (2.7) is

$$V_{th.c.}(fps) = \sqrt{8431(P_o/14.5 + 2942)^{1/7} - 940} \qquad (2.11)$$

$V_{th.c.}$ can also be calculated from the arithmetic mean density value, ρ_m

$$V_{th.c.} \doteq \sqrt{2P_o/\rho_m}$$

$$\rho_m = \frac{\rho + \rho_{P_o}}{2} \qquad (2.12)$$

where values of ρ_{P_o} can be obtained from tables such as Bridgman's Tables (14).

The expansion factor Y_e can be calculated for any pressure range from the equation

$$Y_e = V_{th.c.}/V_{th}$$

using Eqns. (2.9), (2.11) or (2.12) for $V_{th.c.}$

The results are shown in Fig. 2.5 as a plot of Y_e vs. nozzle pressure up to 414 MPa. Eqn. (2.8) represents an average of the other two equations and it is used further with Eqn. (2.9) to calculate the jet flow Mach number,

$$M = V_{th.c.} / \sqrt{\frac{\partial P}{\partial \rho}} \qquad (2.13)$$

These equations enable the calculation of the quantitative effect of compressibiljty on the coefficient of discharge. The effect of compressibility expressed in terms of either M or Y_e on the percentage change of the coefficient of discharge if compressibility were neglected, is plotted in Fig. 2.6. An error of 3.68% in the coefficient of discharge would have resulted if compressibility were neglected at $M = 0.54$ or $Y_e = 0.9633$ and $P_o = 207$ MPa (40 Ksi). If the maximum error allowed in flow calculation (or C_D) is 1%, then the expansion coefficient should be used in Eqn. (2.6) if the Mach number exceeds 0.29 (i.e. $P_o > 138$ MPa). Below this pressure, neglecting compressibility will cause a maximum error of 1% in flows calculated from nozzle pressures.

A comparison of experimental and theoretical flow rates is shown in Figs. 2.7 to 2.9 for three nozzle sizes. The effect of polymer (polyox 0.25%) on improving the flow is also shown. The results are presented as dimensional plots of pressure and flow rate. Figs. 2.10, 2.11 and 2.12 are plots of the pressure and coefficients of discharge. The frictional coefficient of discharge $C_D = Q_{ex}/Q_{th.c.}$ tends to have a constant value at high pressures for all three nozzles, while the overall coefficient of discharge $C_{Do} = Q_{ex}/Q_{th.} = Y_e\ C_D$ first increases and then decreases slightly because of the effect of

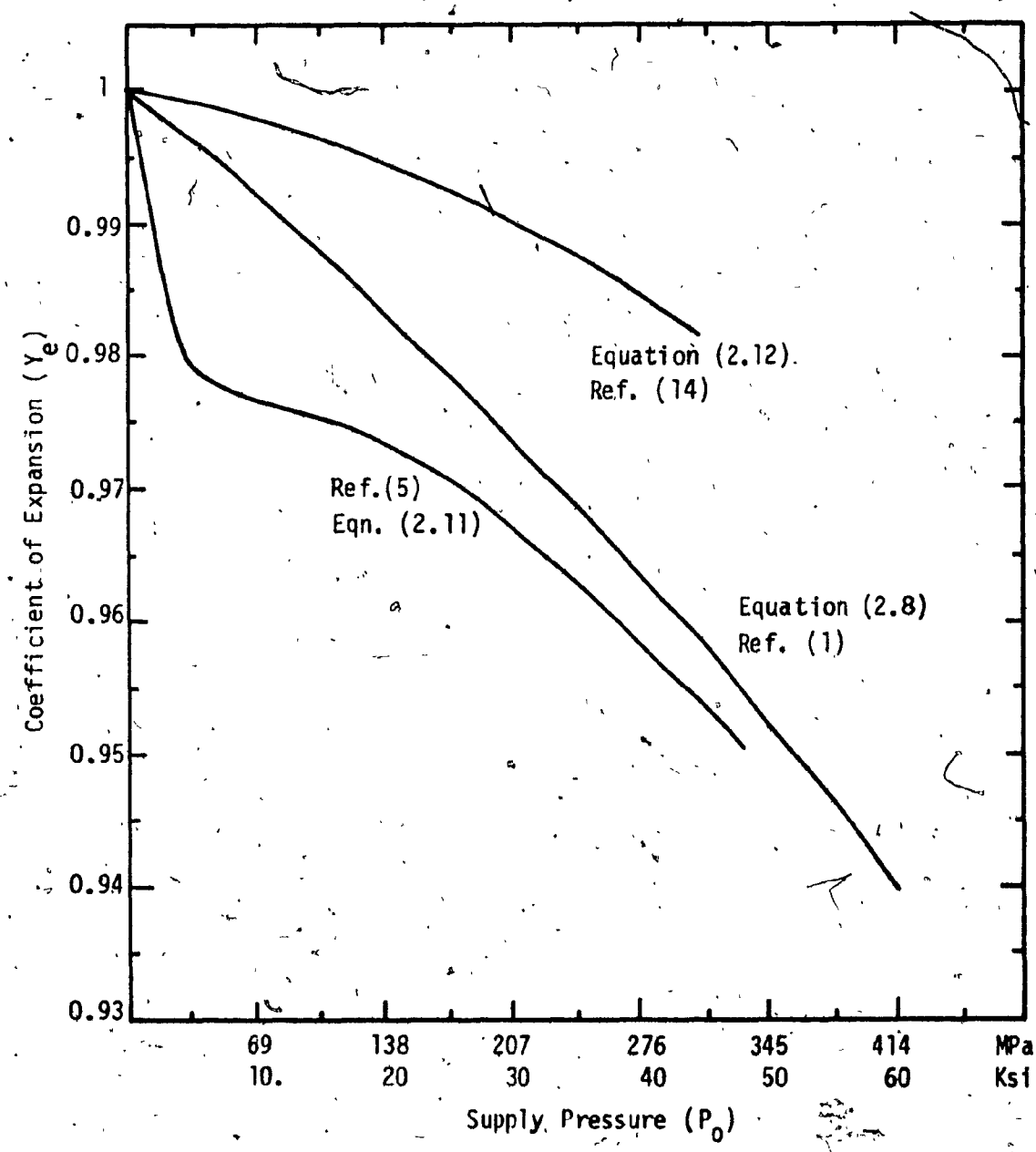

Fig. 2.5 The Coefficient of Expansion as a Function of Supply Pressure

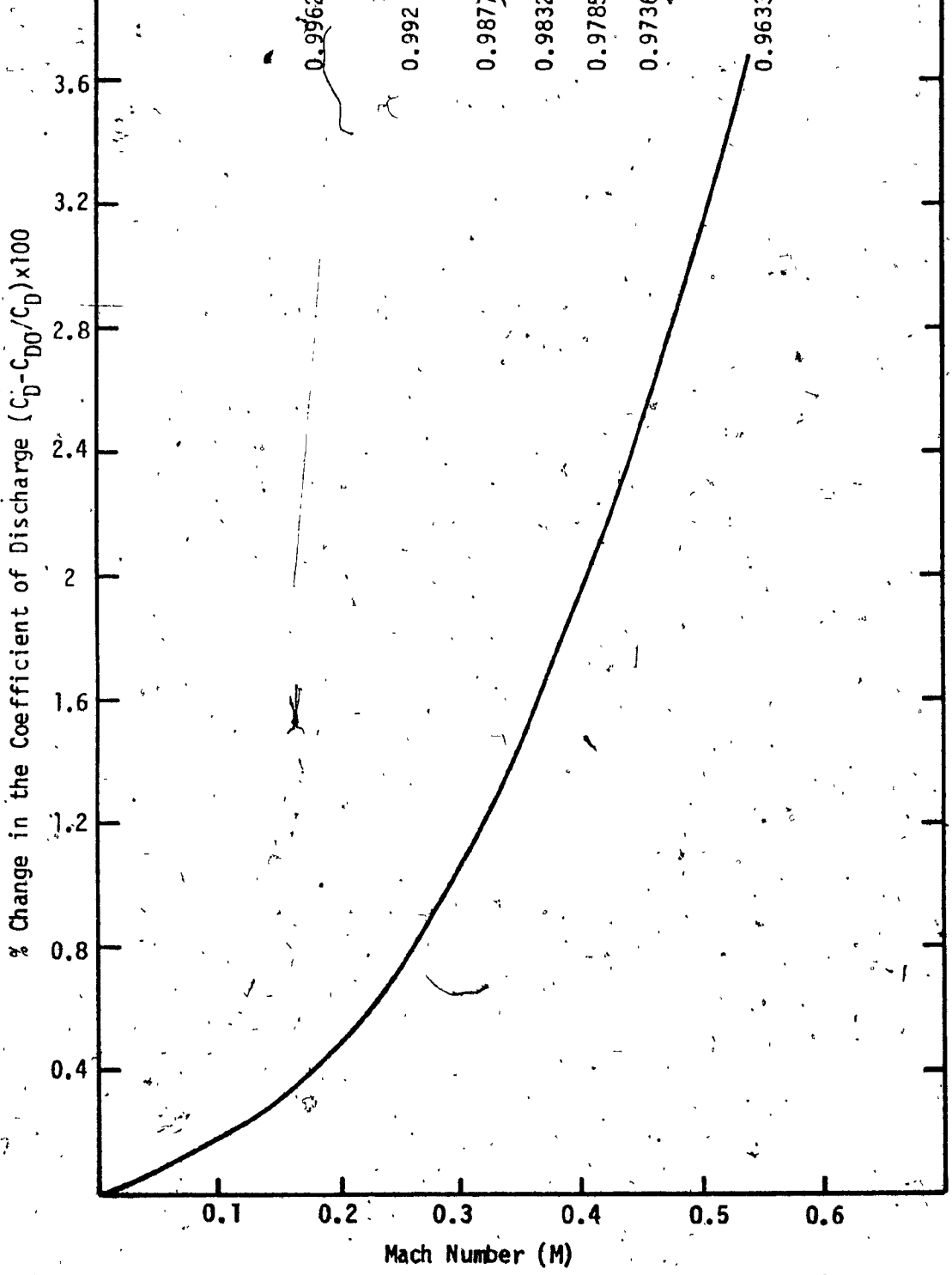

Fig. 2.6 Percentage Change of the Coefficient of Discharge as a Function of Mach Number or the Expansion Coefficient.

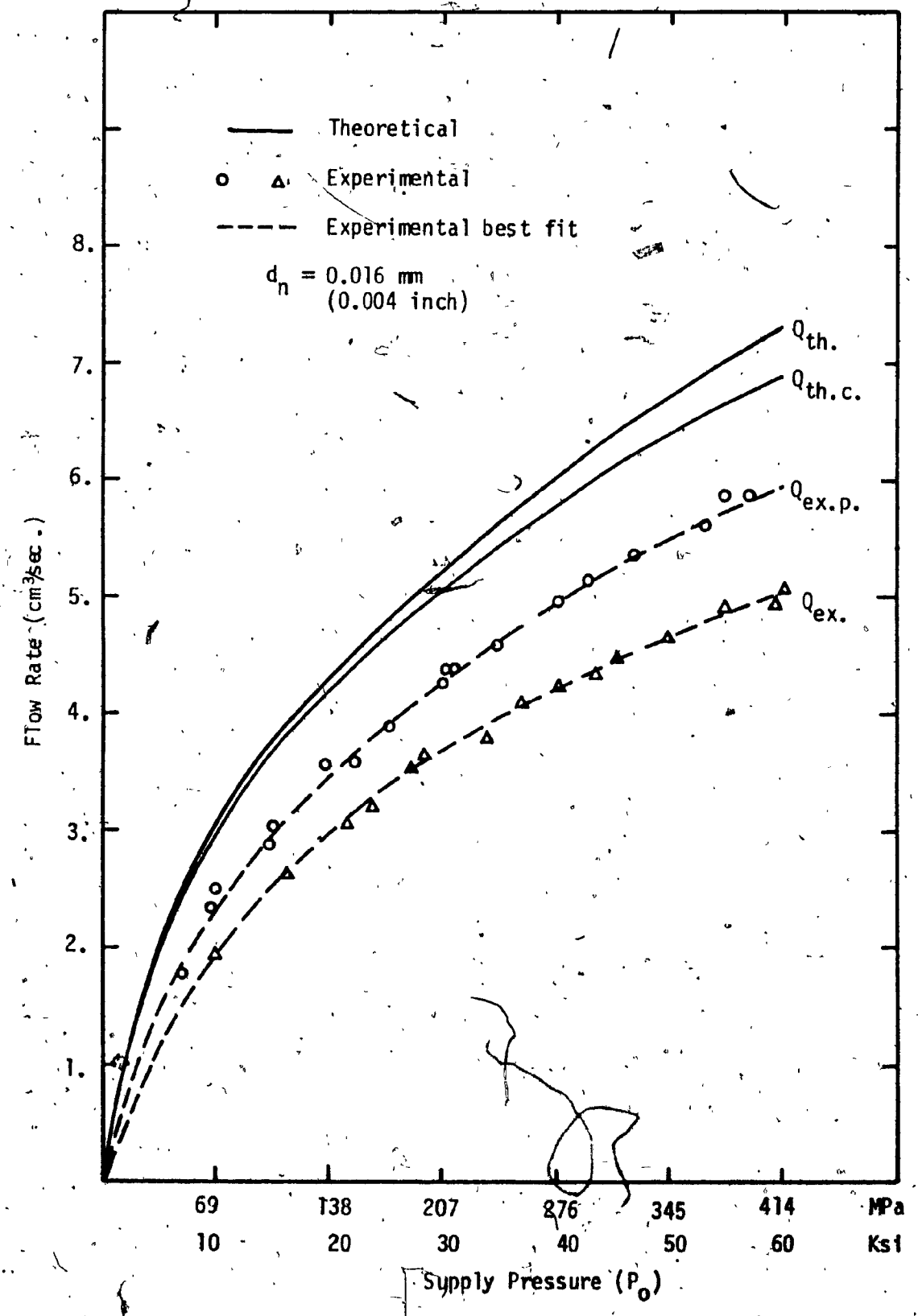

Fig. 2.7 Effect of Supply Pressure on Flow Rate when Using a Nozzle of 0.1016 mm. Diameter.

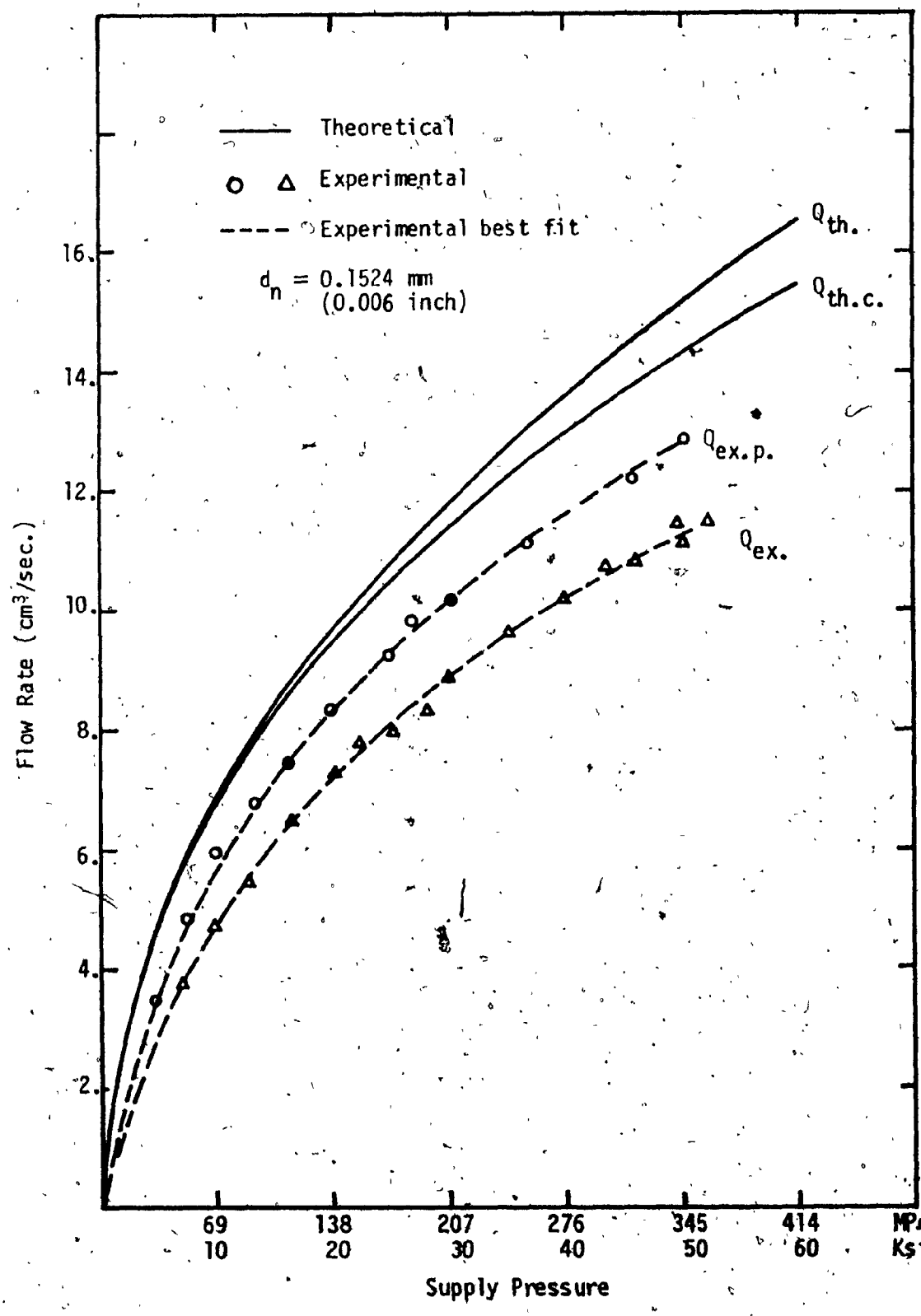

Fig. 2.8 Effect of Supply Pressure on Flow Rate when Using a Nozzle of 0.1524 mm. Diameter.

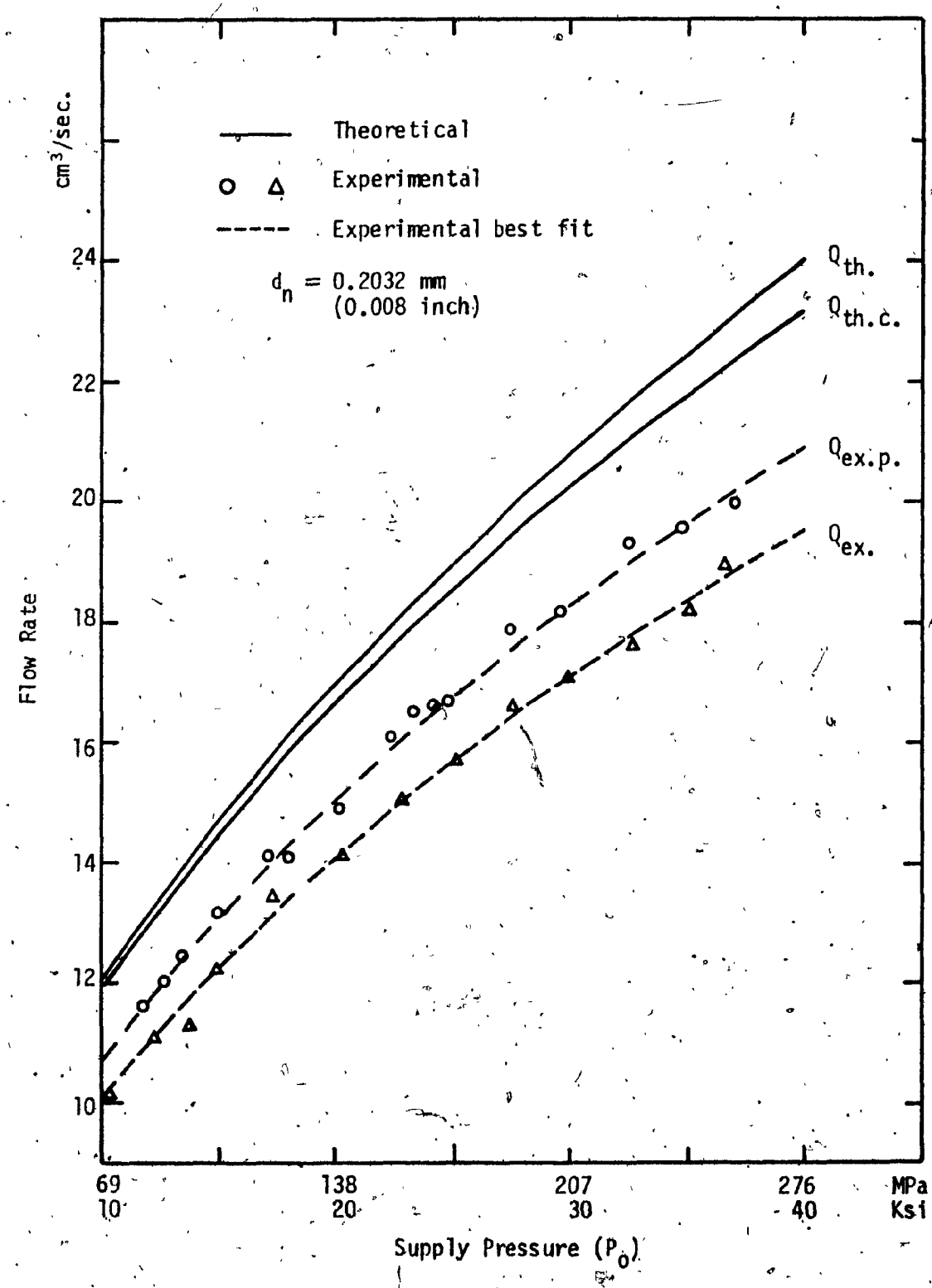

Fig. 2.9 Effect of Supply Pressure on Flow Rate when Using a Nozzle of 0.2032 mm. Diameter.

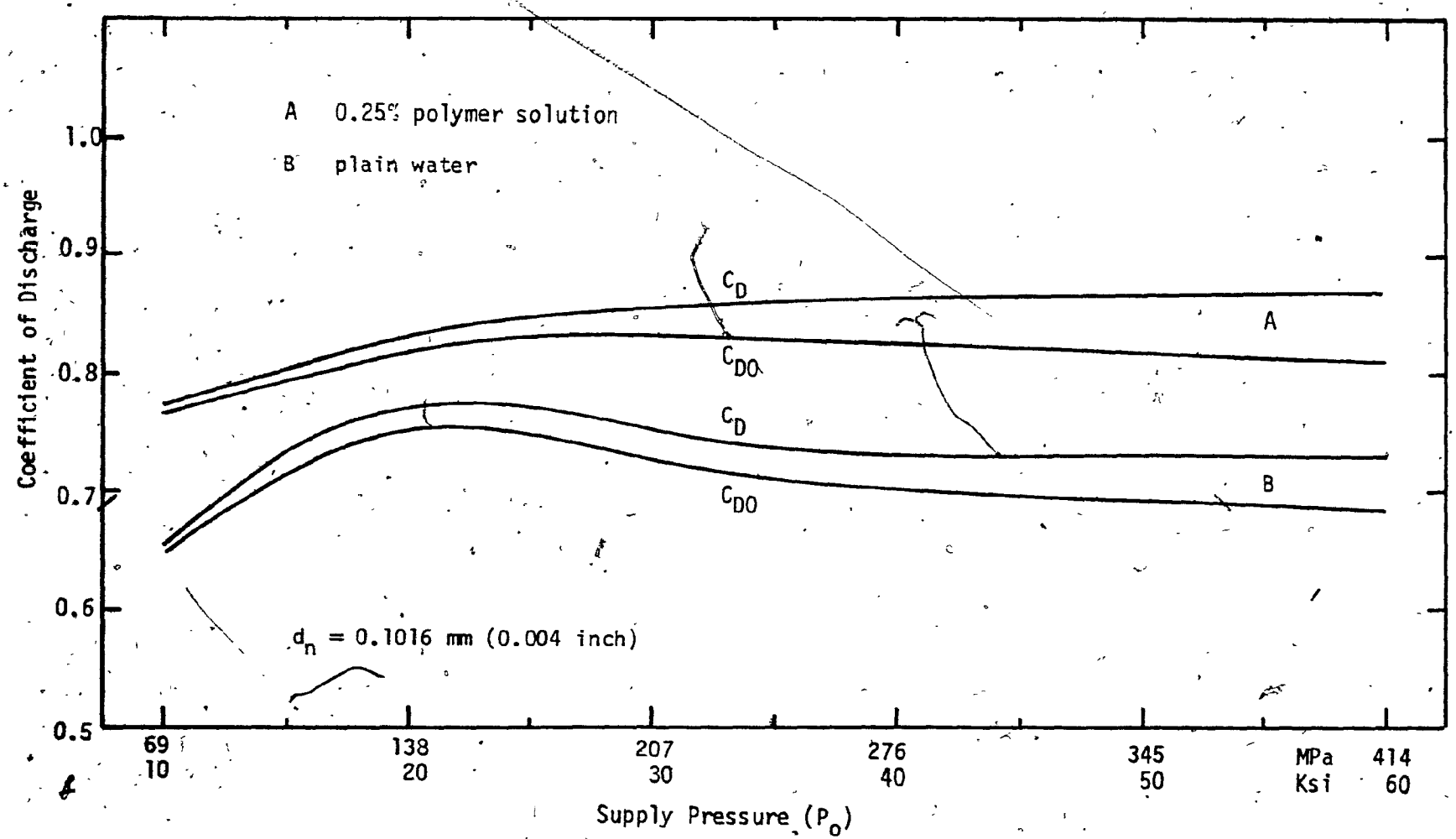

Fig. 2.10 Effect of Supply Pressure on the Coefficients of Discharge for 0.1016 mm. Nozzle Diameter.

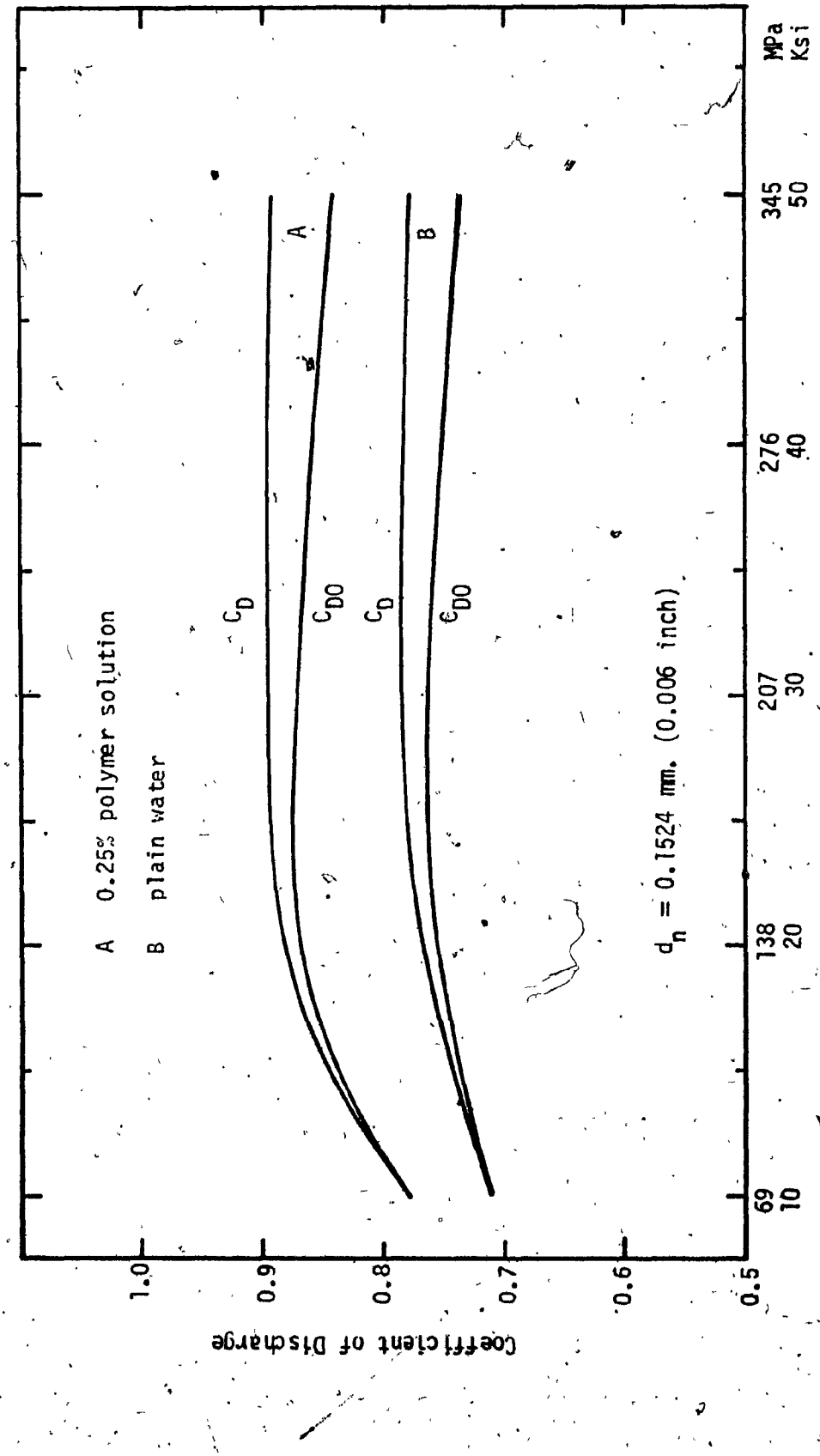

Fig. 2.11 Effect of Supply Pressure on the Coefficients of Discharge for 0.1524 mm. Nozzle Diameter.

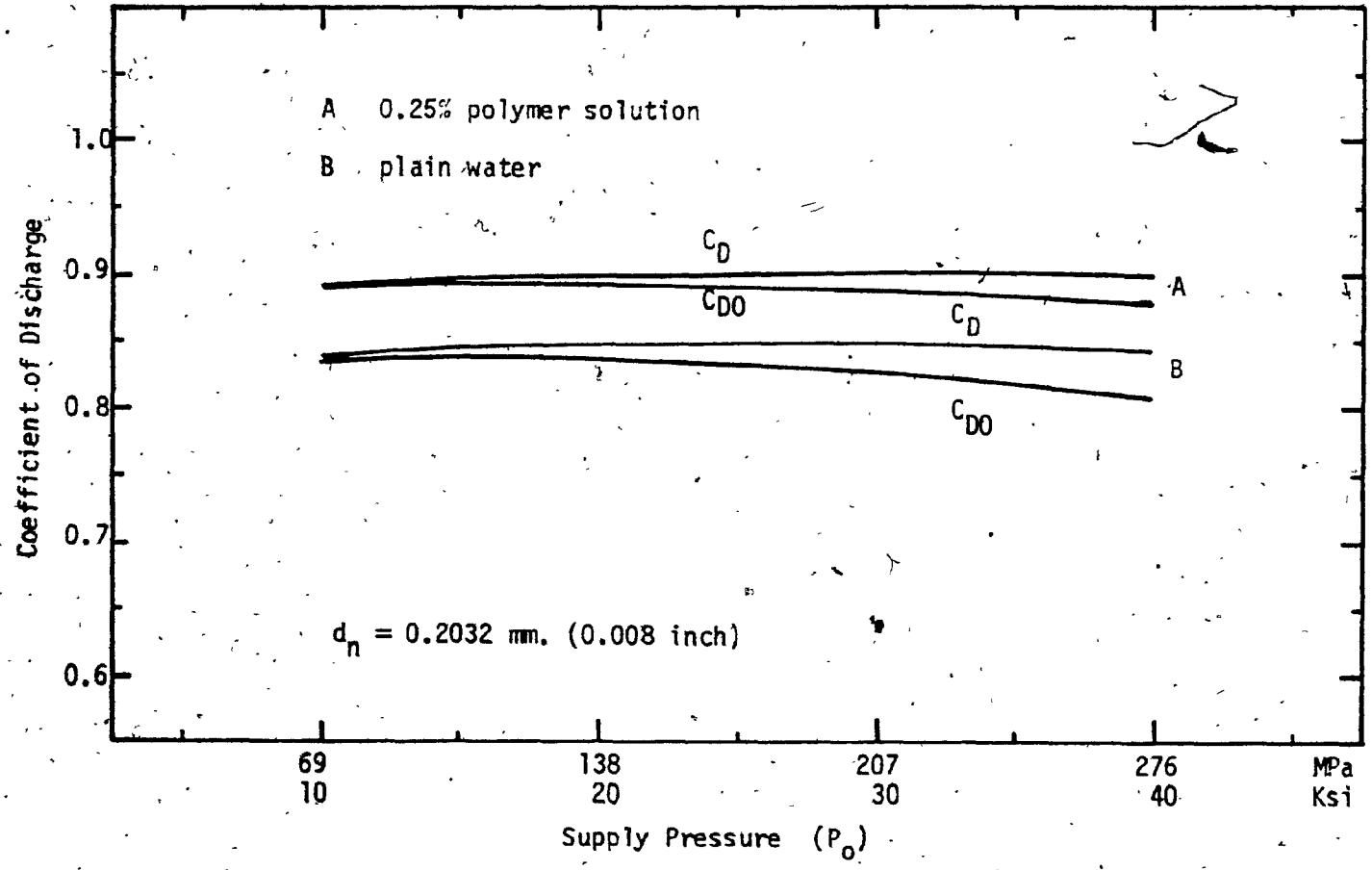

Fig. 2.12 Effect of Supply Pressure on the Coefficients of Discharge for 0.2032 mm. Nozzle Diameter.

the expansion coefficient Y_e which decreases with increasing pressure. Consequently, C_{Do} tends to have a maximum value over the pressure range of 140 MPa to 200 MPa. The existence of maximum values is more pronounced for the smaller nozzle sizes. The polymer additive increases the values of C_D by about 18%, 14% and 6.5% for the 0.1016 mm, 0.1524 mm and 0.2032 mm nozzle diameters respectively but the trend is similar to that with water alone. The overall discharge coefficients C_{Do} are presented as nondimensional functions of Reynold's number in Fig. 2.13. Some published data are also presented. The in-house data with water and data published by Harris (17) display maximum values of C_{Do} for Reynold's number between 40,000 and 70,000. The higher viscosity of the polymer solution decreases the Reynold's number range for maximum values of C_{Do} to between 2000 and 3500.

2.2.2 Force Measurement and Contraction Coefficients

The hydrodynamic jet force F_{ex} was measured as close to the nozzle exit as was practically possible (4 mm from sapphire exit surface). F_{ex} was compared to the expected value F_{th} from the measured flow (Q_{ex}) using the equation

$$F_{th} = \rho \frac{Q_{ex}^2}{A_n} \tag{2.14}$$

Figs. 2.14 and 2.15 show the results of plain water and water with polymer. In all cases, F_{ex} was greater than F_{th}. The explanation is that for the same mass flow rate ρQ_{ex}, the forces are inversely proportional to the areas of flow and that the actual area of flow is

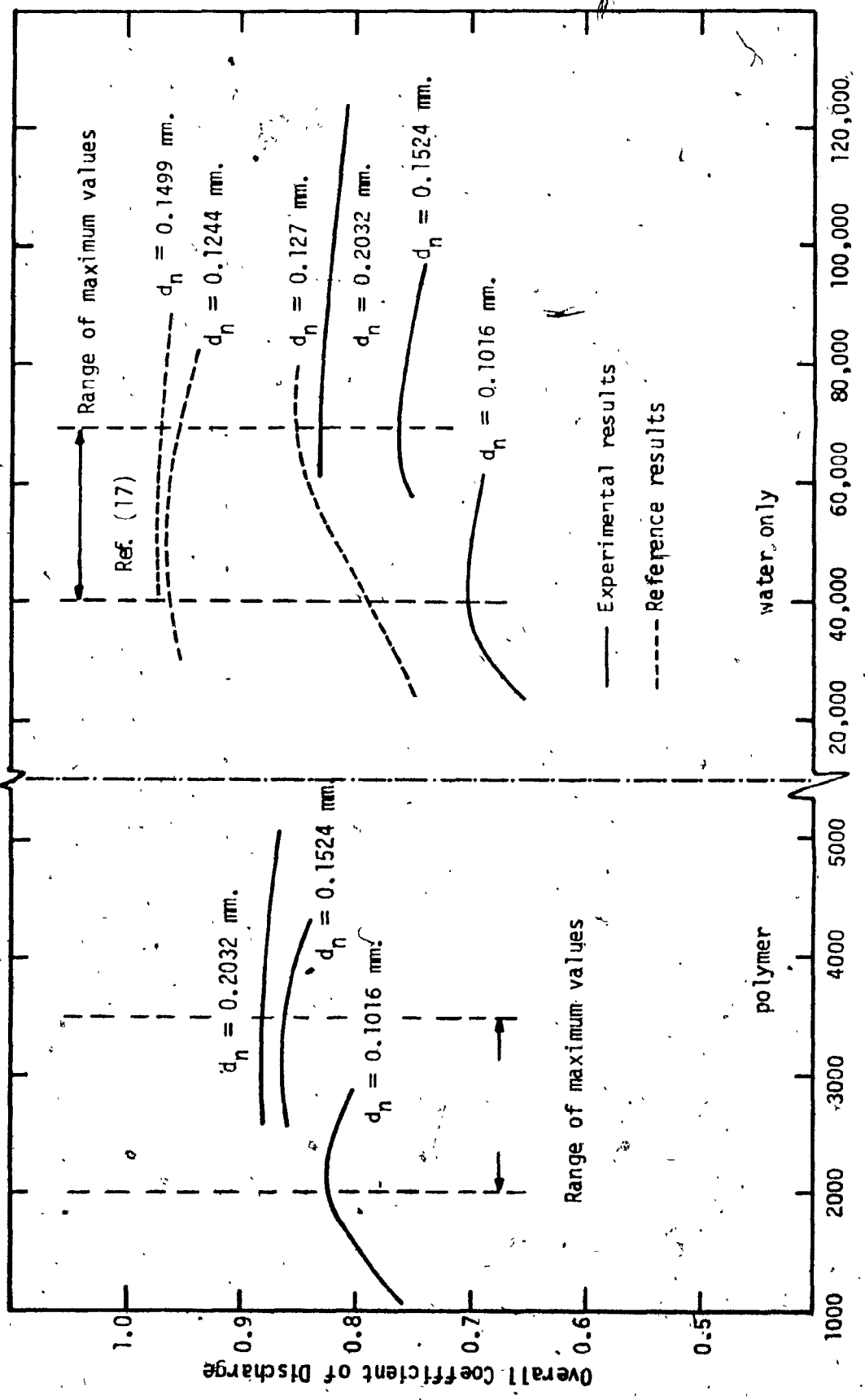

Fig. 2.13 Overall Coefficient of Discharge Versus Reynold's Number for Different Nozzle Diameters.

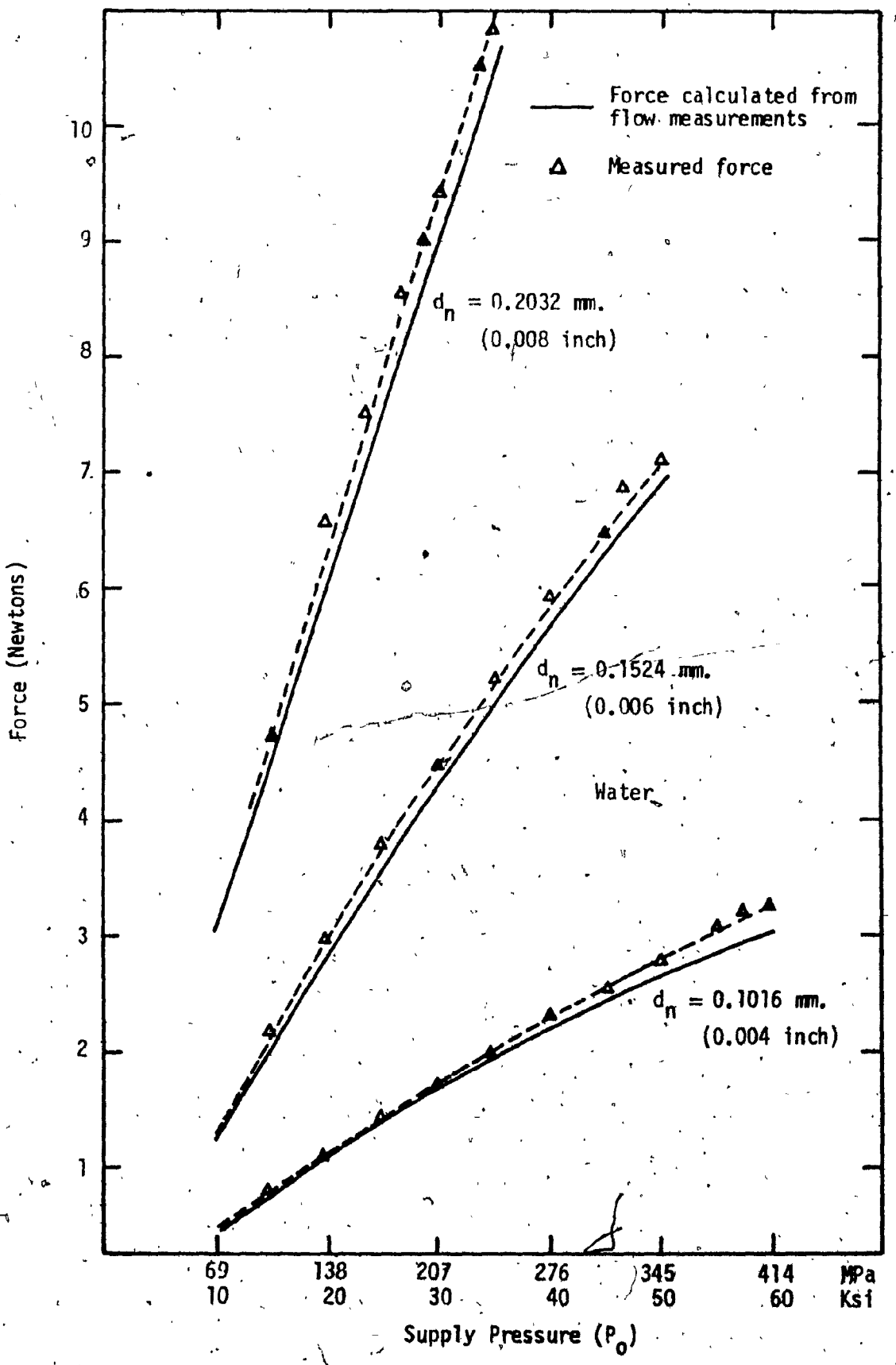

Fig. 2.14 Effect of Supply Pressure on Jet Hydrodynamic Force Using Plain Water.

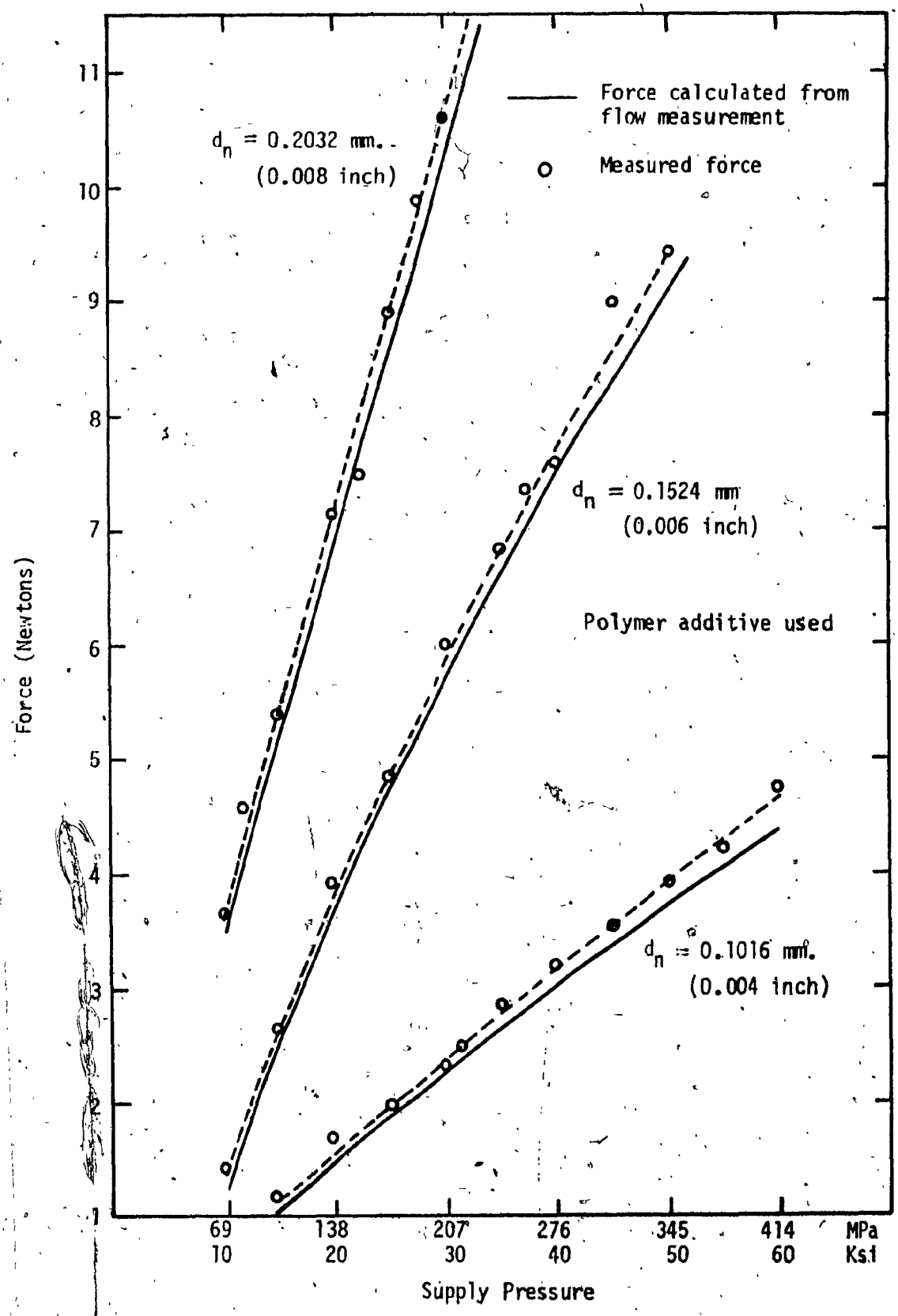

Fig. 2.15 Effect of Supply Pressure on Jet Hydrodynamic Force when Using 0.25% Polymer Solution.

less than the nozzle exit area A_n due to jet contraction in the vicinity of the vena contracta. The conversion of pressure to kinetic energy is maximum at the vena contracta, so that the total momentum of the jet near the vena contracta must be related to the measured force by

$$F_{ex} = \rho \frac{Q_{ex}^2}{A_{vc}} \tag{2.15}$$

where A_{vc} is the reduced area of the jet due to contraction. The coefficient of contraction, C_c, can be calculated from

$$C_c = \frac{A_{vc}}{A_n} = \frac{F_{th}}{F_{ex}} \tag{2.16}$$

Typical values of C_c at 241 MPa (35 Ksi) are listed in Table 2.1 following, together with values of C_D for water with and without polymer.

d_n		Water			Polymer		
inch	mm	C_D	C_c	C_V	C_D	C_c	C_V
0.004	0.1016	0.728	0.961	0.7575	0.86	0.94	0.915
0.006	0.1524	0.7803	0.97	0.804	0.89	0.951	0.9726
0.008	0.2032	0.845	0.985	0.858	0.9	0.97	0.928

Table 2.1 Values of Flow and Contraction Coefficients at Pressure 241.5 MPa (35 Ksi).

Comparison of the values for water and polymer clearly show the effect of the polymer at a fixed value of the nozzle pressure. Comparison of C_V shows that polymer increases the velocity by 17%. Comparison of C_c shows that polymer increases jet contraction by about 2%. The overall effect is that polymer increases the flow rate by a

maximum of 13%. These values are used in the following section to determine nozzle efficiences and head losses.

2.2.3 Nozzle Efficiency and Head Loss

The efficiency with which a nozzle converts pressure energy into kinetic energy is given by

$$\eta_n = \frac{\text{power output } E_o}{\text{available power } E_a}$$

where $$E_o = \frac{1}{2} \rho A_{vc} V_{vc}^3$$

$$E_a = \frac{1}{2} \rho A_n V_{th}^3$$

and $$V_{vc} = C_v Y_e V_{th}$$

then $$\eta_n = C_c (C_v Y_e)^3 \qquad (2.17)$$

which is affected by contraction, friction and compressibility. The pressure loss in the nozzle is a frequently used term which is given by

$$P_L = P_o - \frac{\rho V_{vc}^2}{2}$$

where $$V_{vc} = C_v \cdot Y_e \cdot \sqrt{2p_o/\rho}$$

Substituting V_{vc} from the second equation in the first equation and dividing by P_o, gives

$$\frac{P_L}{P_o} = 1 - (C_v Y_e)^2 \qquad (2.18)$$

All the terms on the right hand side of Eqns. (2.17) and (2.18) are functions of pressure as presented in Sections 2.2.1 and 2.2.2 Figs. 2.16a, 2.16b and 2.17 show the effect of pressure on the efficiency, power delivered and coefficient of pressure loss. Figs. 2.16a and 2.16b show an optimum efficiency at pressures from about 140 to 200 MPa. However, nozzle size has a far greater effect on efficiency which increases from 40% to 60% when the nozzle diameter increases from 0.1 to 0.2 mm. Polymer addition (0.25% polyox) improves the efficiency by maximum values of 72%, 60% and 25% for the three nozzle sizes 0.1016 mm, 0.1524 mm and 0.2032 mm respectively. The efficiency range when using water (Fig. 2.16a) is from 30% to 60% while the efficiency range when using polymer (Fig. 2.16b) is from 50% to 75%. Fig. 2.17 shows the coefficient of pressure loss (Eqn. (3.18)) which has the values of 0.3 to 0.55 when using water alone and from 0.1 to 0.35 when using polymer.

2.2.4 Spreading Characteristics of the Jet

Fig. 2.18 compares the experimental results obtained with the three nozzle sizes with the relationship proposed by Yanaida (15):

$$w = 0.335 \sqrt{d_n X} \qquad (2.19)$$

There is reasonable agreement between Eqn. (2.19) and the experimental values. Better agreement is obtained when the vena contracta diameter is used in Eqn. (2.19). Yanaida's equation was derived for low pressure water jets (up to 30 MPa), and the agreement

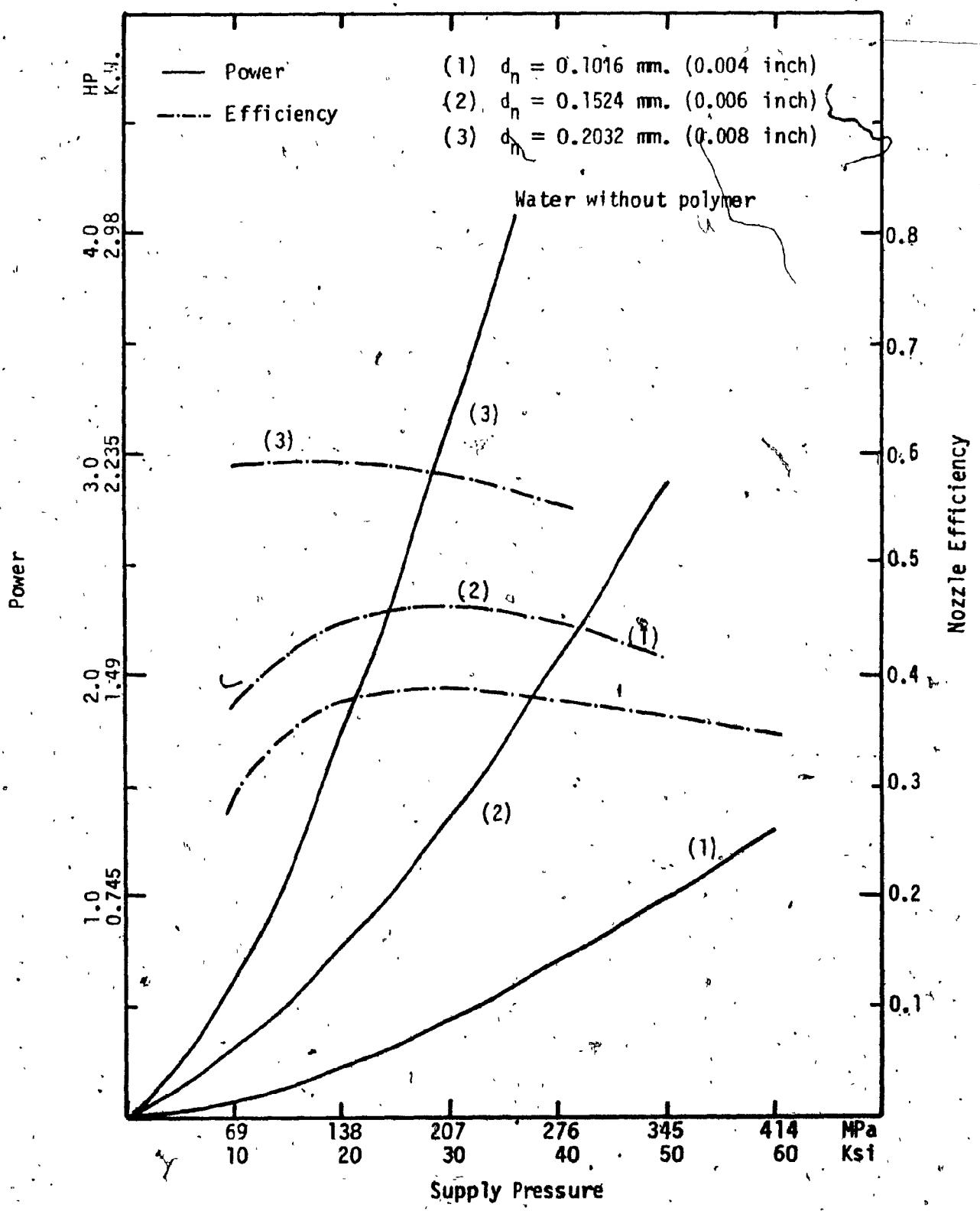

Fig. 2.16a Power and Nozzle Efficiency at Different Nozzle Diameters and Supply pressures for Plain Water.

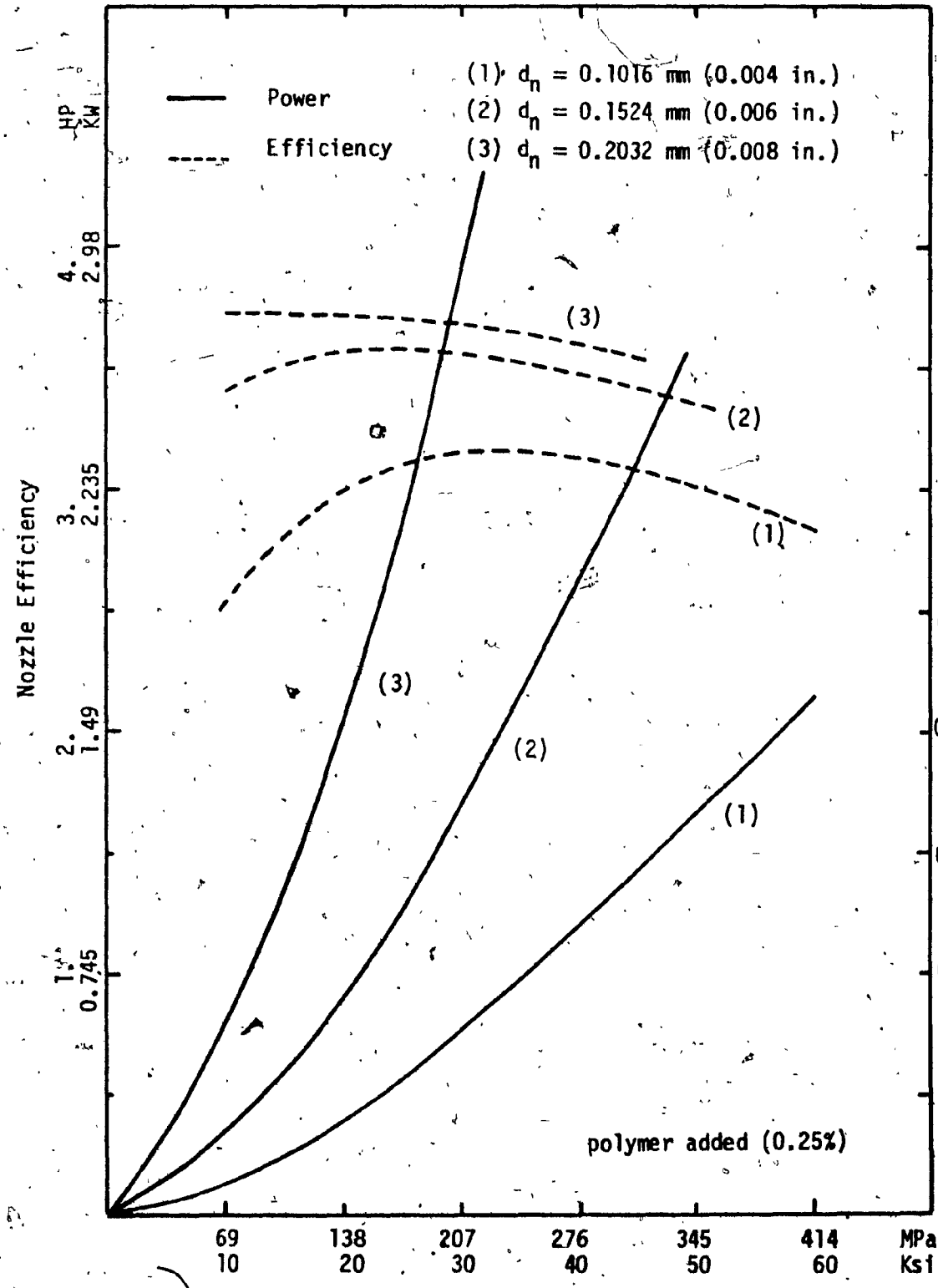

Fig. 2.16b Power and Nozzle Efficiency at Different Nozzle Diameters and Supply Pressures when using Polymer.

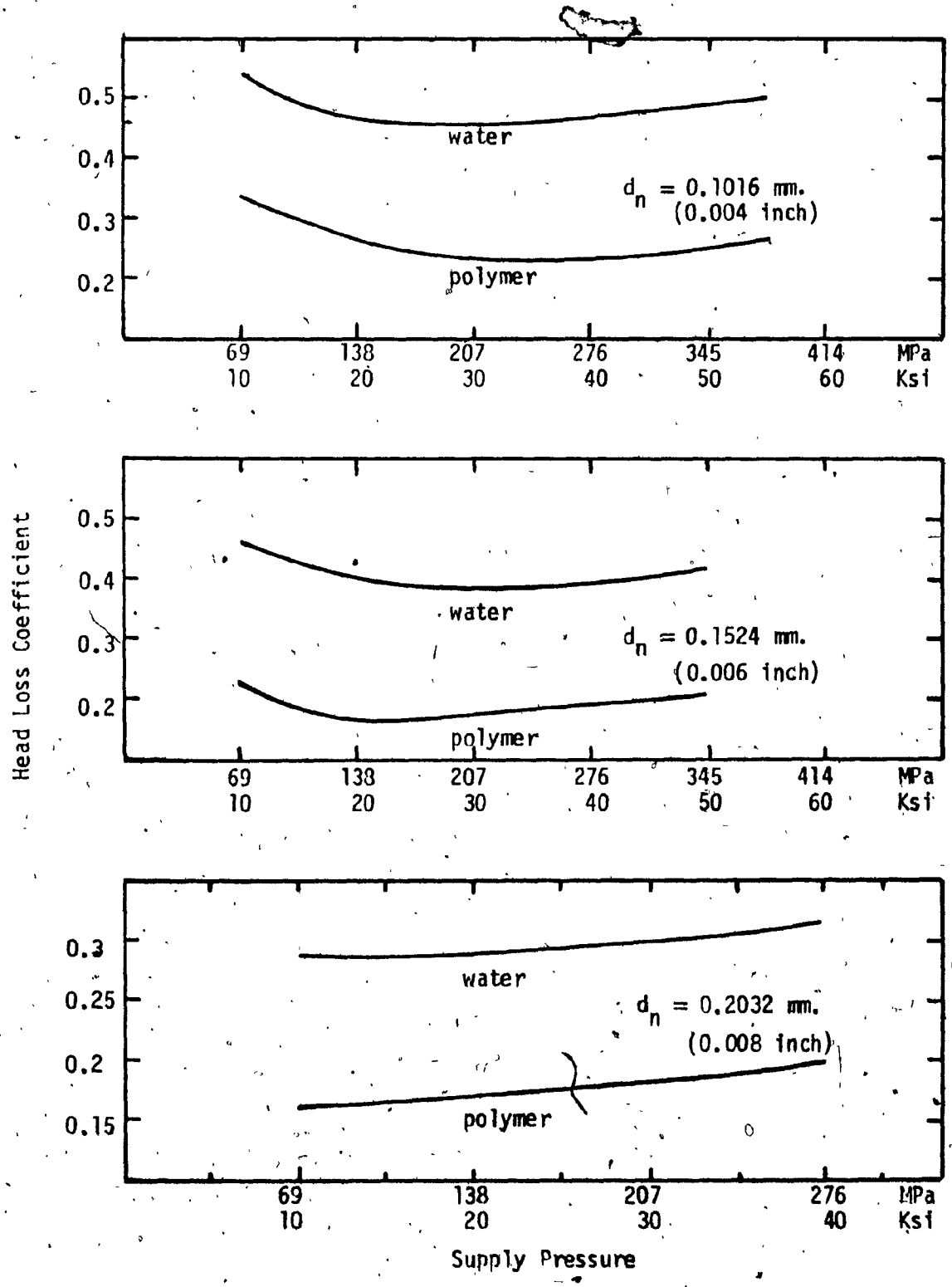

Fig. 2.17 Head Loss Coefficient at Different Pressures and Nozzle Diameters when Using Plain Water or 0.25% Polymer-Water Solution.

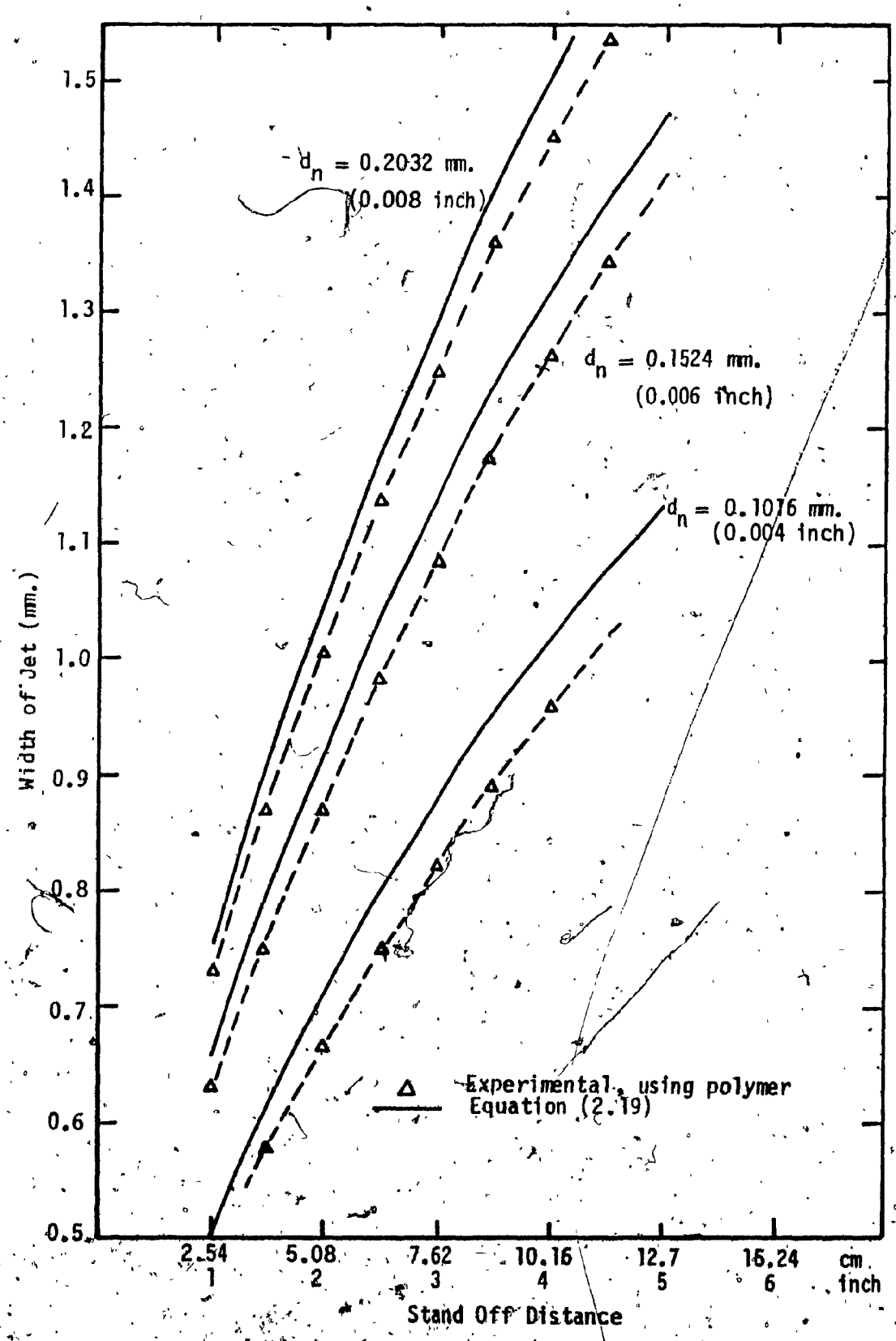

Fig. 2.18 Effect of Stand Off Distance on Jet Width for Three Different Nozzle Diameters.

with the present high pressure data indicates that polymer counteracts the rapid jet dispersion that occurs with high pressure water jets. These high pressure jets with polymer have spreading characteristics similar to the low pressure water jets which are adequately represented by Eqn. (2.19). Fig. 2.19 shows the difference between the physical appearance of the jets with and without polymer.

2.2.5 Conclusions

In summary, the findings of the investigation of nozzle and jet characteristics are:

1. Typical nozzle flows have Reynold's numbers of 20,000 to 80,000 and Mach numbers of 0.25 to 0.5 so that their performance is affected by both viscous and compressibility effects.

2. Frictional characteristics are conveniently quantified by numerical values of the velocity coefficient C_V and the flow coefficient C_D while the expansion factor Y_e quantifies compressibility effects. Eqns. (2.5), (2.6), (2.17) and (2.18) give the required relation between these coefficients and the jet velocity, jet flow, nozzle power efficiency and pressure loss coefficient. The equations are useful because the nozzle flow characteristics can be calculated at any particular pressure if the values of the appropriate coefficients are known.

3. There is considerable variation in the values of C_V, C_D and C_{D_o} at corresponding values of Reynold's number and Mach number. Nozzle size appears to have the dominant effect on the numerical

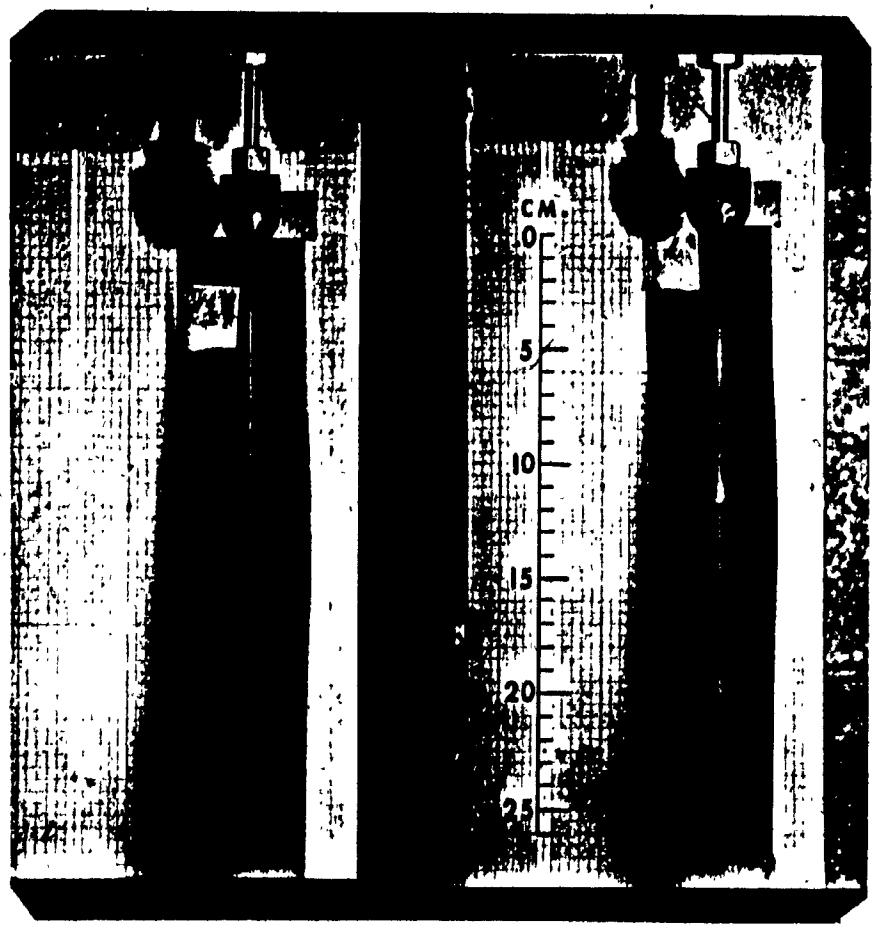

(1) (2)

Fig. 2.19

The Effect of Polymer on the Physical Appearance of the Jet.

P_o = 276 MPa (40,000 psi)
d_n = 0.127 mm. (0.005 inch)

(1) Plain Water
(2) Polyox added to the water with 0.25% concentration

values of these coefficients. Typical values of C_{D_o} at R_e = 60,000 are 0.69, 0.75 and 0.83 for 0.1, 0.15 and 0.2 mm nozzle diameters respectively using plain water.

4. The maximum values of the overall coefficients of discharge and velocity occur in the pressure range 140 - 200 MPa and R_e = 40,000 to 65,000. Typical maximum values of C_{D_o} are 0.7, 0.76 and 0.83 for nozzle diameters 0.1, 0.15 and 0.2 mm respectively.

5. The use of polymer (0.25% polyox) has the following effects:

   a - Increases the flow rate at 276 MPa (40 Ksi) by 17.6%, 12.7% and 6.6% for nozzle diameters 0.1, 0.15 and 0.2 mm respectively;

   b - The percentage pressure loss in the nozzle improves from the range of 30% - 55% for water, to 10% - 35% when using polymer.

   c - The momentum delivery is improved when using polymer because of the increase in flow rate and the lower contraction coefficient values. The reduction in the jet cross-sectional area is 2%, 1.9% and 1.5% for nozzle diameters 0.1, 0.15 and 0.2 mm respectively when using polymer.

   d - The increase in the nozzle efficiency when using polymer is 72%, 60% and 25% and the increase in the overall coefficient of discharge is 17%, 14% and 6.5% for nozzle diameters 0.1, 0.15 and 0.2 mm respectively.

6. The width of the jet with polymer has been found proportional to the square root of distance from nozzle exit as suggested in the reference data for low pressure values.

2.3 INVESTIGATION OF THE CUTTING PROCESS. SCOPE AND SOURCE OF DATA.

2.3.1 Cutting Variables

The variables that describe the cutting process are:

1. Jet parameters; jet velocity (or nozzle pressure and C_c, C_v, Y_e), nozzle diameter and stand off distance.
2. Cutting parameters; feed rate, number of passes, depth of cut, volume of material removed and specific energy (or cutting efficiency).
3. Material properties; density, porosity and strength parameters such as compressive, yield, shear and other strength properties.

2.3.2 Scope and Source of Data

Because of the large number of variables involved and the complexity of the cutting process, the investigation encompassed high speed photography to physically observe the cutting process, in-house cutting data and analysis. The different phases of the work are summarized below and the sources of the data used are listed in Table 2.2 followed by a detailed listing of all the experimental data in Tables 2.3 to 2.22.

Phase I.

Experimental investigation and dimensional analysis with one type of material (wood) to determine the dominant material properties and to develop an empirical equation which relates the depth of cut to the nozzle and material parameters.

Phase II.

Formulate a model of the cutting process and develop a general theory which is used with in-house data and published test results to determine the material properties that dominate the cutting process and that are also common to the different types of material.

Phase III.

Investigate the effect of stand off distance and multipass cutting on cutting results. Combine the general cutting equation with the empirical jet spreading equation of section 2.2.4 to determine the conditions under which stand off distance can be optimized for maximum depth of cut and maximum volume removal of material.

Phase IV.

Combine the steady state cutting equation at very high feed rate with existing models of material erosion by drop impact to develop cutting equations for pulsed jets.

Phase	No.	Material	Ref.	Variables and Purpose
I	1	Poplar	author	Depth of cut as a function of nozzle diameter, jet velocity and feed rate. Determine dominant material properties. data used in Chapters 3, 4.
	2	Maple	author	
	3	Elm	author	
	4	Douglas Fir	(1)	
	5	Red Oak	(1)	
II	1	Phase I - 1,2,3	author	Depth of cut as a function of nozzle diameter, jet velocity and feed rate. Development of theoretical cutting model.
	2	Sugar Maple	(1)	
	3	Indiana Limestone	(18)	
	4	Coal	(20),(21)	
	5	Red Woolten	(25)	
	6	Concrete	(22)	
	7	Polycarbonate	(12)	
	8	White Granite	(23)	Data used in Chapter 4.
	9	Wilkeson S.S.	(23)	
	10	Limestone	(19)	
	11	Ice	(24)	
	12	Plastic	author	High speed photography.
III	1	Poplar	author	Effects of stand off distance, feed rate and multipass cutting on depth of cut, volume removal & specific energy. Data used in Chapter 5.
	2	Maple	author	
	3	Elm	author	
	4	Limestone	(19)	
	5	Aluminium	(26)	
	6	Coal	(27)	

Table 2.2 Data used in Different Phases of the Investigation.

PHASE I. WOOD CUTTING RESULTS.

	d_n		P_o		u		Depth of Cut					
							Maple		Poplar		Elm	
	inch	mm	psi	MPa	in/sec	cm/sec	inch	cm	inch	cm	inch	cm
1	0.003	0.0762	56000	386.4	0.086	0.21844	0.355	0.9017	0.449	1.1405	0.275	0.6985
2					0.156	0.39624	0.29	0.7366	0.371	0.9423	0.249	0.6325
3					0.300	0.7620	0.208	0.5283	0.267	0.6782	0.191	0.4851
4			30000	207	0.086	0.21844	0.148	0.3759	0.198	0.5029	0.115	0.2921
5					0.156	0.39624	0.135	0.3429	0.167	0.4470	0.099	0.2515
6					0.300	0.7620	0.117	0.2972	0.141	0.3581	0.084	0.3124
7			40000	276	0.086	0.21844	0.280	0.7712	0.354	0.8992	0.205	0.5207
8					0.156	0.39624	0.229	0.5817	0.253	0.6426	0.142	0.3607
9					0.300	0.7620	0.159	0.4039	0.237	0.6020	0.119	0.3023
10	0.005	0.127	50000	345	0.086	0.21844	0.42	1.0663	0.699	1.7755	0.340	0.8636
11					0.156	0.39624	0.356	0.9042	0.51	1.2954	0.285	0.7239
12					0.300	0.7620	0.208	0.5283	0.391	0.9931	0.200	0.5080
13			40000	279	0.086	0.21844	0.411	1.0439	0.48	1.2192	0.318	0.8077
14					0.156	0.39624	0.325	0.8255	0.386	0.9804	0.257	0.6528
15					0.300	0.7620	0.29	0.7866	0.365	0.9271	0.175	0.4445
16			30000	207	0.086	0.21844	0.28	0.7712	0.334	0.8484	0.256	0.6502
17					0.156	0.39624	0.232	0.5893	0.305	0.7747	0.204	0.5181
18					0.300	0.7620	0.21	0.5334	0.240	0.6096	0.168	0.4140
19	0.007	0.1778	35000	241.5	0.086	0.21844	0.552	1.4021	0.670	1.7018	0.370	0.9398
20			34000	234.6	0.156	0.39624	0.417	1.0592	0.474	1.2040	0.270	0.6858
21			30000	207	0.300	0.7620	0.331	0.8407	0.415	1.0541	0.230	0.5842
22			21000	144.9	0.086	0.21844	0.266	0.6756	0.366	0.9296	0.210	0.5334
23					0.156	0.39624	0.200	0.5080	0.278	0.7061	0.163	0.4140
24					0.300	0.7620	0.129	0.3277	0.221	0.5613	0.137	0.3480
25			14000	96.5	0.086	0.21844	0.15	0.3810	0.156	0.3962	0.131	0.3327
26					0.156	0.39624	0.127	0.3226	0.150	0.3810	0.090	0.2286
27					0.300	0.7620	0.109	0.2767	0.140	0.3556	0.054	0.1372

Table 2.3 Effect of Supply Pressure, Feed Rate and Nozzle Diameter on the Depth of Cut of Poplar, Maple and Elm.

Table 2.4 Results of Cutting of Douglas Fir and Red Oak Ref. (1).

No.	d_n		P_o		u		Depth of Cut			
							Douglas Fir		Red Oak	
	inch	mm	psi	MPa	in/sec	cm/sec	inch	cm	inch	cm
1	0.005	0.127	10000	69	0.25	0.6125	0.06	0.1524	0.05	0.127
2	0.005	0.127	20000	138	0.25	0.6125	0.19	0.4836	0.16	0.4064
3	0.005	0.127	30000	207	0.25	0.6125	0.35	0.889	0.33	0.8382
4	0.005	0.127	40000	276	0.25	0.6125	0.45	1.143	0.45	1.143
5	0.005	0.127	50000	345	0.25	0.6125	0.7	1.778	0.65	1.651

PHASE II CUTTING DATA FOR DIFFERENT MATERIALS.

No.	d_n		P_o		u		z	
	inch	mm	psi	MPa	in/sec	cm/sec	inch	cm
1	0.005	0.127	35000	241.5	0.25	0.6125	0.23	0.5842
2	0.005	0.127	35000	241.5	0.5	1.27	0.2	0.508
3	0.005	0.127	35000	241.5	1.0	2.54	0.16	0.4064
4	0.005	0.127	10000	69	0.25	0.635	0.01	0.0254
5	0.005	0.127	20000	138	0.25	0.635	0.13	0.3302
6	0.005	0.127	30000	207	0.25	0.635	0.62	1.5749
7	0.005	0.127	40000	276	0.25	0.635	0.47	1.1938
8	0.005	0.127	50000	345	0.25	0.635	0.24	0.6098

Table 2.5 Cutting Results of Sugar Maple Ref. (1).

No.	d_n		P_o		u		z	
	inch	mm	psi	MPa	in/sec	cm/sec	inch	cm
1	0.008	0.02032	20000	138	0.264	0.6706	0.3	0.762
2	0.008	0.02032	20000	138	2.28	5.7912	0.175	0.4445
3	0.01	0.0254	20000	138	0.264	0.6706	0.4	1.016
4	0.008	0.02032	40000	276	0.264	0.6706	0.625	1.5875
5	0.008	0.02032	40000	276	2.28	5.7912	0.3	0.762
6	0.001	0.0254	40000	276	0.624	1.5849	0.82	2.0828
7	0.008	0.02032	60000	414	0.264	0.6706	1.1	2.794
8	0.008	0.02032	60000	414	2.28	5.7912	0.5	1.27
9	0.008	0.02032	60000	414	0.612	1.5545	0.8	2.032

Table 2.6 Cutting Results of Indiana Limestone Ref. (18).

No.	d_n		P_o		u		z	
	inch	mm	psi	MPa	in/sec	cm/sec	inch	cm
1	0.0197	0.5001	124000	855.6	16	40.64	1.87	4.7498
2	0.0197	0.5001	139000	959.1	4	10.16	1.68	4.2672
3	0.0197	0.5001	132000	910.8	4	10.16	1.55	3.937
4	0.0197	0.5001	151000	1083.3	4	10.16	1.43	3.6322
5	0.0197	0.5001	112000	772.8	4	10.16	1.75	4.445
6	0.0197	0.5001	42000	289.8	4	10.16	1.37	3.4798
7	0.0197	0.5001	87000	600.3	4	10.16	1.3	3.302
8	0.0197	0.5001	89000	614.1	4	10.16	1.0	2.540
9	0.0197	0.5001	150000	1039	4	10.16	1.87	4.7498
10	0.0197	0.5001	126000	869.4	4	10.16	1.81	4.5974

Table 2.7 Cutting Results of Limestone Ref. (19).

No.	d_n		P_o		u		z	
	inch	mm	psi	MPa	in/sec	cm/sec	inch	cm
1	0.0196	0.500	5000	34.5	3.28	8.3312	0.39	0.9906
2	0.0196	0.500	10000	69	3.28	8.3312	0.93	2.3622
3	0.196	0.500	15000	103.5	3.28	8.3312	0.97	2.4638
4	0.023	0.5842	10000	69	3.28	8.3312	0.98	2.4892
5	0.023	0.5842	15000	103.5	3.28	8.3312	1.56	3.9624
6	0.026	0.6604	5000	34.5	3.28	8.3312	0.425	1.0795
7	0.026	0.6604	10000	69	3.28	8.3312	0.846	2.1945
8	0.026	0.6604	15000	103.5	3.28	8.3312	1.93	4.9022
9	0.026	0.6604	20000	138	3.28	8.3312	2.7	6.858
10	0.03	0.762	5000	34.5	3.28	8.3312	0.56	1.4224
11	0.03	0.762	10000	69	3.28	8.3312	1.27	3.2258
12	0.03	0.762	15000	103.5	3.28	8.3312	2.44	6.1976
13	0.035	0.889	10000	69	3.28	8.3312	2.34	5.9436
14	0.0397	1.0084	5000	34.5	3.28	8.3312	1.24	3.1496

Stand off distance = 3.8 cm (1.496 inch)

Table 2.8 Cutting Results of Coal Ref. (20).

No.	P_o		u		z/d_n
	psi	MPa	in/sec	cm/sec	---
1	2940	20.286	11.79	29.95	50
2	2640	18.216	11.79	29.95	35
3	2940	20.286	29.47	74.85	28
4	2640	18.216	29.47	74.85	15
5	2640	18.216	78.6	199.64	19

Stand off distance = 2.54 cm (1 inch)
Data were given as z/d_n values.

Table 2.9 Cutting Results of Coal Ref. (21).

No.	d_n		P_o		u		z	
	inch	mm	psi	MPa	cm/sec	cm/sec	inch	cm
1	0.007	0.1778	30000	207	16	40.64	0.04	0.1016
2	0.007	0.1778	30000	207	8.5	21.59	0.05	0.127
3	0.007	0.1778	30000	207	2	5.08	0.065	0.1661
4	0.007	0.1778	50000	345	16	40.64	0.075	0.1906
5	0.007	0.1778	50000	345	8.5	21.59	0.09	0.2286
6	0.007	0.1778	50000	345	2	5.08	0.15	0.381
7	0.007	0.1778	70000	483	16	40.64	0.1	0.254
8	0.007	0.1778	70000	483	8.5	21.59	0.13	0.3302
9	0.007	0.1778	70000	483	2	5.08	0.2	0.508

Table 2.10 Cutting Results of Concrete Ref. (22).

No.	d_n		P_o		u		z	
	inch	mm	psi	MPa	in/sec	cm/sec	inch	cm
1	0.003	0.0762	30000	207	0.4	1.016	0.05	0.127
2	0.003	0.0762	40000	276	0.4	1.016	0.1	0.254
3	0.003	0.0762	50000	345	0.4	1.016	0.13	0.3302
4	0.003	0.0762	60000	414	0.4	1.016	0.18	0.4572
5	0.005	0.127	60000	414	0.8	2.032	0.3	0.762
6	0.005	0.127	50000	345	1.2	3.048	0.2	0.508
7	0.005	0.127	30000	207	0.8	2.032	0.1	0.254
8	0.007	0.1778	30000	207	0.4	1.016	0.19	0.4826
9	0.007	0.1778	60000	414	0.8	2.032	0.5	1.27
10	0.007	0.1778	50000	345	1.2	3.048	0.3	0.762

Table 2.11 Cutting Results of Polycarbonate Ref. (12).

No.	d_n		P_o		u		z	
	inch	cm	psi	MPa	in/sec	cm/sec	inch	cm
1	0.03	0.762	19000	131.1	0.13	0.3302	1.51	3.8354
2	0.03	0.762	19000	131.1	0.21	0.5334	1.45	3.683
3	0.03	0.762	19000	131.1	0.33	0.8382	1.26	3.2
4	0.03	0.762	19000	131.1	0.53	1.3462	1.06	2.6924
5	0.03	0.762	19000	131.1	0.85	2.159	1.01	2.5654
6	0.03	0.762	19000	131.1	1.33	3.3782	0.91	2.3114

Table 2.12 Cutting Results of Wilkeson Sandstone Ref. (23).

No.	d_n		P_o		u		z	
	inch	mm	psi	MPa	in/sec	cm/sec	inch	cm
1	0,014	0.3556	60000	414	0.6	1.524	0.77	1.9558
2	0.014	0.3556	60000	414	1.0	2.54	0.74	1.8795
3	0.014	0.3556	60000	414	1.6	4.064	0.7	1,778
4	0.014	0.3556	60000	414	2.5	6.35	0.51	1.2954
5	0.014	0.3556	60000	414	4.0	10.16	0.44	1.1176
6	0.014	0.3556	60000	414	6.0	15.24	0.37	0.9398

Table 2.13 Cutting Results of White Granite Ref. (23).

No.	d_n		P_o		u		z	
	inch	mm	psi	MPa	in/sec	cm/sec	inch	cm
1	0.02	0.508	100000	690	50	127	3.75	9.525
2	0.02	0.508	100000	690	51.4	130.56	6	15.24
3	0.012	0.3048	60000	414	37.8	96.01	2.75	6.985
4	0.012	0.3048	60000	414	16.66	42.32	3	7.62
5	0.012	0.3048	60000	414	11.78	29.92	4.5	11.53
6	0.016	0.4064	60000	414	18.4	46.75	5	12.5
7	0.016	0.4064	60000	414	13.92	35.36	6.5	16.51
8	0.016	0.4064	60000	414	13.2	33.53	6.5	16.51

Table 2.14 Cutting Results of Ice Ref. (24).

No.	d_n		P_o		u		z	
	inch	mm	psi	MPa	in/sec	cm/sec	inch	cm
1	0.039	0.9906	28000	193.2	19.6^8	49.784	1.65	4.191
2	0.039	0.9906	43000	296.7	19.6^8	49.784	2.55	6.477
3	0.039	0.9906	51000	393.3	19.6^8	49.784	3.34	8.436
4	0.039	0.9906	72000	496.8	19.6^8	49.784	3.93	8.6106
5	0.039	0.9906	39000	269.1	15.7	39.878	2.75	6.985
6	0.039	0.9906	49000	338.1	47	119.38	1.96	4.064

Table 2.15 Cutting Results of Red Woolten Ref. (25).

PHASE III EFFECT OF STAND OFF DISTANCE AND MULTIPASSES ON CUTTING RESULTS.

No.	X		Depth of Cut					
			Poplar		Maple		Elm	
	inch	cm	inch	cm	inch	cm	inch	cm
1	0.6	1.524	0.46	1.18	0.326	0.83	0.236	0.60
2	0.8	2.032	0.41	1.05	0.295	0.75	0.22	0.56
3	1.0	2.54	0.385	0.98	0.275	0.70	0.2	0.51
4	1.2	3.048	0.338	0.86	0.259	0.66	0.189	0.48
5	1.4	3.556	0.315	0.80	0.236	0.60	0.157	0.40
6	1.6	4.064	0.303	0.77	0.228	0.58	0.145	0.37
7	1.8	4.572	0.29	0.74	0.208	0.53	0.141	0.36
8	2.0	5.08	0.267	0.68	0.204	0.52	0.137	0.35
9	2.2	5.558	0.263	0.67	0.189	0.48	0.118	0.3
10	2.4	6.096	0.244	0.62	0.185	0.47	0.11	0.28
11	2.6	6.604	0.24	0.61	0.177	0.45	0.106	0.27
12	2.8	7.112	0.232	0.59	0.165	0.42	0.102	0.26

d_n = 0.1016 mm (0.004 inch)

P_o = 276 MPa (40,000 psi)

u = 0.2 cm/sec. (0.074 inch/sec.)

Table 2.16 Effect of Stand Off Distance on Depth of Cut for Wood (Poplar, Maple, Elm).

No.	P_o = 241.5 MPa (35000 psi)				No.	P_o = 172.5 MPa (25000 psi)			
	X		z			X		z	
	inch	cm	inch	cm		inch	cm	inch	cm
1	1.0	2,54	0.0145	0.0368	7	1.0	2.54	0.007	0.0178
2	2.0	5.08	0.02	0.0508	8	2.0	5.08	0.011	0.0279
3	3.0	7.62	0.018	0.0457	9	3.0	7.62	0.01	0.0254
4	4.0	10.16	0.0145	0.0368	10	4.0	10.16	0.007	0.0178
5	5.0	12.70	0.009	0.0229	11	5.0	12.70	0.0045	0.0114
6	6.0	15.24	0.003	0.0076	12	6.0	15.24	0.001	0.0025

Test conditions: d_n = 0.254 mm (0.01 inch)

u = 2.54 cm/sec. (1 inch/sec.)

Table 2.17 Effect of Stand Off Distance on Depth of Cut of Aluminium Ref. (26).

No. of Passes	Poplar				Maple				Elm			
	Feed Rate*				Feed Rate				Feed Rate			
	1	2	3	4	1	2	3	4	1	2	3	4
1	0.6	0.51	0.2	0.1	0.5	0.356	0.1	0.05	0.3	0.285	0.09	0.05
2	1.15	0.7	0.32	0.19	0.8	0.4	0.25	--	0.63	0.4	0.22	0.1
3	--	0.9	--	--	1.3	0.76	0.36	0.18	0.98	--	0.28	--
4	2.05	1.2	0.7	0.33	1.5	0.9	0.46	0.25	1.2	0.78	0.42	0.2
8	3.3	2.2	1.3	0.66	2.5	1.55	0.87	0.45	2.75	1.2	0.7	0.34
11	--	--	--	0.87	--	1.9	1.18	--	--	1.6	0.96	--
14	--	3.05	--	1.05	--	--	1.38	0.8	--	--	--	--
15	--	--	--	--	--	2.4	1.4	--	--	--	--	0.6
16	--	3.3	2.0	1.12	--	2.49	1.5	0.86	--	0.2	1.2	0.65

* (1) u = 0.198 cm/sec. (0.078 in/sec.)
(2) u = 0.396 cm/sec. (0.156 in/sec.)
(3) u = 0.792 cm/sec. (0.312 in/sec.)
(4) u = 1.584 cm/sec. (0.624 in/sec.)

P_o = 345 MPa (50,000 psi)
d_n = 0.1524 mm (0.006 inch)
X_1 = 6.35 mm (0.75 inch)

Table 2.18 Number of Passes and Accumulated Depth of Cut of Wood at Different Feed Rates.

No.	u in/sec.	Number of Passes 1	2	4	8	16
1	2	2.81	4.72	6.38	11.54	14.33
2	4	--	4.16	5.1	6.988	11.77
3	10	1.44	2.53	3.6	4.86	6.53
4	20	1.03	1.64	2.72	4.34	6.34
5	32	1.78	0.83	3.09	1.91	4.6

Depth of cut is in inches (1 inch = 2.54 cm)
P_o = 69 MPa (10,000 psi)
d_n = 1 mm (0.0393 inch)

Table 2.19 Effect of Multipass Cutting on Depth of Cut of coal Ref. (27).

X inch	Poplar w_1 cm	Poplar w_2 cm	Poplar ΔV cm^3	Maple w_1 cm	Maple w_2 cm	Maple ΔV cm^3	Elm w_1 cm	Elm w_2 cm	Elm ΔV cm^3
0.6	0.108	0.034	0.084	0.106	0.033	0.058	0.13	0.03	0.048
0.8	0.127	0.038	0.087	0.13	0.038	0.063	0.13	0.031	0.045
1.0	0.129	0.044	0.085	0.146	0.042	0.066	0.136	0.036	0.044
1.2	0.15	0.045	0.084	0.137	0.042	0.059	0.136	0.039	0.042
1.4	0.163	0.047	0.084	0.141	0.045	0.056	0.16	0.04	0.04
1.6	0.16	0.05	0.081	0.115	0.047	0.055	0.176	0.04	0.04
1.8	0.168	0.05	0.081	0.152	0.051	0.054	0.163	0.042	0.037
2.0	0.176	0.053	0.078	0.146	0.05	0.051	0.157	0.043	0.035
2.2	0.185	0.056	0.081	0.158	0.05	0.05	0.176	0.045	0.033
2.4	0.189	0.059	0.077	0.155	0.053	0.049	0.169	0.045	0.03
2.6	0.19	0.059	0.076	0.164	0.053	0.049	0.198	0.046	0.033
2.8	0.194	0.06	0.075	0.165	0.054	0.046	0.167	0.048	0.028

Depth of cut is given in Table 2.16.
d_n = 0.1061 mm (0.04 inch)
P_o = 276 MPa (40,000 psi)
u = 2 cm/sec. (0.079 in/sec.)

Table 2.20 Effect of Stand Off Distance on volume Removal of Wood.

No.	u		Poplar			Maple			Elm		
			z	w_1	SE	z	w_1	SE	z	w_1	SE
	in/sec	in/sec	cm	cm	J/CC	cm	cm	J/CC	cm	cm	J/CC
1	0.2032	0.08	1.05	0.127	93554	0.75	0.13	127948	0.56	0.13	171359
2	0.4064	0.16	0.53	0.126	93407	0.47	0.12	123759	0.3	0.129	161175
3	0.8128	0.32	0.26	0.13	92274	0.21	0.12	123759	0.15	0.13	159935
4	1.6256	0.64	0.145	0.127	84683	0.11	0.12	118134	0.073	0.123	173669
5	3.2512	1.28	0.072	0.13	83299	0.055	0.119	119127	0.04	0.129	151102
6	6.5024	2.56	0.036	0.13	83299	0.03	0.117	111066	0.022	0.119	148908

X =2.032 cm (0.8 inch)
d_n =0.1016 mm (0.004 inch)
P_o =276 MPa (40,000 psi)

Table 2.21- Effect of Feed Rate on Specific Energy of Wood.

No.	P_o		z	w_1	E	SE	Volume
	MPa	Ksi	cm	cm	Joules	J/cm^3	cm^3
1	959	139	4.28	0.317	66338	6030	11
2	911	132	3.96	0.317	61724	5143	12
3	1083	157	4.44	0.396	47669	3666	13
4	290	42	3.3	0.317	32695	4086	8
5	614	89	2.54	0.317	34146	4878	7
6	1035	150	4.76	0.396	74171	5297	14
7	869	126	4.6	0.317	57451	4419	13

u = 10.16 cm/sec. (4 inch/sec.)
X = 2.54 cm (1 inch)
d_n = 0.5 mm (0.0197 inch)

Table 2.22 Effect of Pressure on Specific Energy of Limestone. Ref. (19)

CHAPTER 3

INVESTIGATION OF JET CUTTING PROCESS WITH WOOD - PHASE I

3.1 INTRODUCTION

In order to evaluate the potential of jet cutting in a particular application, it is necessary to relate the depth of cut that can be achieved with different nozzle sizes and pressures to the cutting speed and to the known properties of the material. The literature contains many examples of cutting theories that apply to particular types of materials. Most theories contain coefficients that have to be determined experimentally for each type of material. In general, these values cannot be related to known material properties such as compressive; shear and tensile strengths. This Chapter describes an experimental investigation of jet cutting of different types of woods used in the furniture manufacturing industry. The objective is to determine the most important physical properties of wood that affect the depth of cut at different cutting speeds and the hydraulic power needed to achieve these cutting depths.

3.2 PHYSICAL PROPERTIES OF WOOD

Published data for wood (28) list 14 different properties as shown in Table 3.1 for three types of wood commonly used in different furniture manufacturing operations. Moisture content effects the values of wood properties. As shown in Fig. 3.1, the compressive strength changes from 78.28 MPa (11400 psi) to 39.14 MPa (5700 psi)

			POPLAR				MAPLE				ELM			
			1	2	3	4	1	2	3	4	1	2	3	4
specific gravity	basic*	volume green / oven dry weight	0.372	88	8.7	---	0.466	78	4.7	---	0.625	632	10.3	---
	nominal	volume air dry / oven dry weight	---	---	---	0.415	0.507	---	---	---	0.661	---	---	---
	oven dry	volume oven dry / oven dry weight	0.416	36	6.4	---	0.53	36	5.3	---	0.73	78	15.2	---
compression parallel to grain	proportional limit, psi		1200	26	29	2400	2860	36	23.9	3890	2920	223	25	4390
	max. crushing stress psi		2390	75	13.1	4750	3800	28	13	6120	4080	632	18.9	7460
	modulus of elasticity 1000 psi		1210	26	18.5	1650	1350	36	13.4	1430	1500	223	20.9	1910
compression perpendicular to grain, proportional limit $(\sigma_c)^*$, psi			212	29	21.9	473	564	23	15.1	830	813	272	25.4	1287
shear parallel to grain $(\sigma_s)^*$, psi			789	47	12.1	1098	1265	36	11.4	1755	1438	332	16.5	2148
cleavage $(\sigma_{CL})^*$, psi			202	49	22.1	260	395	36	15	495	499	324	20.1	523
tension perpendicular to grain $(\sigma_t)^*$, psi			412	50	35.4	581	790	35	24.7	765	973	322	20.6	1051

* values used in the analysis

four statistics are included (1) green condition (2) number of specimens (3) coefficient of variation (4) air dry condition

(1000 psi = 6.9 MPa)

TABLE 3.1, Wood Properties (28)

when moisture contents change from 8% to 20% (29). Wood properties are usually specified at a standard moisture content of 12%. Considerable variation exists in the value of a property for one type of wood as shown in Table 3.1. The properties further depend on the direction in which the wood is stressed relative to the grain direction. Electron-microscopy of wood fibres cut by water jets (30) suggests that the cutting action is a complex mechanism which involves compression-, shear- and tension-failure of the wood fibres. Bryan (1) suggests that cutting results from direct penetration as a result of extreme stresses at the point of impact followed by secondary deepening of the kerf which is directly related to the total energy per unit length of the jet.

3.3 EXPERIMENTAL INVESTIGATION

To evaluate the potential of jets for cutting wood, an equation is required to predict the cutting depth that can be obtained with different types of wood at different cutting speeds and hydraulic power levels and the changes in depth that are caused by variations in the properties of one wood type when the cutting speed and power are constant.

As a first step towards developing such an equation, experiments were conducted to determine which wood properties are dominant in their effect on cutting depth and speed. Previous work by Bryan (1) identified specific weight of wood as an important factor. His experimental constants (a_1, a_2 in Table 1.1) cannot be related to particular wood properties.

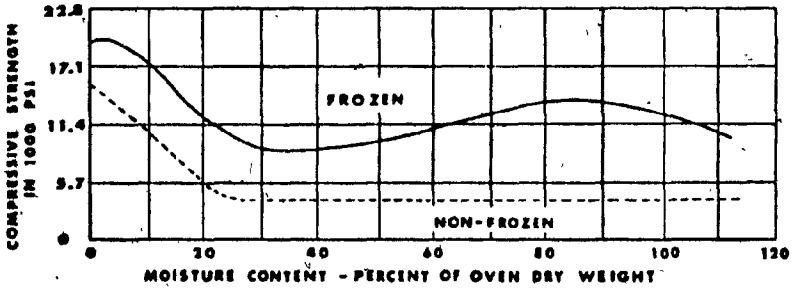

(1000 psi = 6.9 MPa)

Fig. 3.1 Effect of Moisture Content on Compressive Strength Parallel to Grain (29).

Tests were conducted with three types of wood, namely: Poplar, Maple and Elm that are commonly used in different furniture manufacturing operations. Their properties, listed in Table 3.1, cover a range normally classified as "soft to medium hard". The property showing the greatest variation between the three woods is compression perpendicular to the grain; the average values vary from 1.45 MPa (212 psi) for Poplar to 5.58 MPa (813 psi) for Maple. Samples were prepared for "cross-cutting" tests where both the jet axis and the cutting direction are perpendicular to the grain. Each sample was 2.54 cm x 2.54 cm by 15 cm long. The experimental investigation consisted of 81 tests with three orifice sizes, three pressures and three feed rates as listed in Table 2.3. Details of the depth of cut measurement procedure are described in Section 2.1.2e.

The effect of moisture content on the depth of cut was investigated first. Fig. 3.2 shows results obtained with wood cured at room humidity and samples that were submerged in water for 48 hours. The results show that the effect of moisture content increases with the cutting speed. At 0.76 cm/sec. (0.3 inch/sec.) cutting speed, the wet wood depth of cut is 0.038 cm (0.015 inch) or 3% greater than the dry wood depth of cut. This indicates that the wetting process during cutting may be an important parameter for some wood types at higher cutting speeds. A choice had to be made in planning the experiments. The first choice is to control and standardize the moisture of the samples before testing and then to measure the moisture content of the kerf area after the tests. The second choice is to try to minimize the effects of initial moisture content of the sample and wetting during the cutting process by performing tests on saturated samples. This represents wood in the "green" condition. The second method was adopted for this study to avoid the practical difficulties associated with measuring the local moisture content and its variation during the cutting process. The results with saturated wood may be applied to wood with other moisture contents using the empirical relationship (29) of moisture content effect on the strength properties.

$$\sigma = \sigma_d \cdot 10^{\alpha - \beta \cdot mc} \qquad (3.1)$$

where σ_d is the strength property at air dry condition (12% moisture content), α and β are constants for each material and mc is the moisture content in the range up to and including saturation.

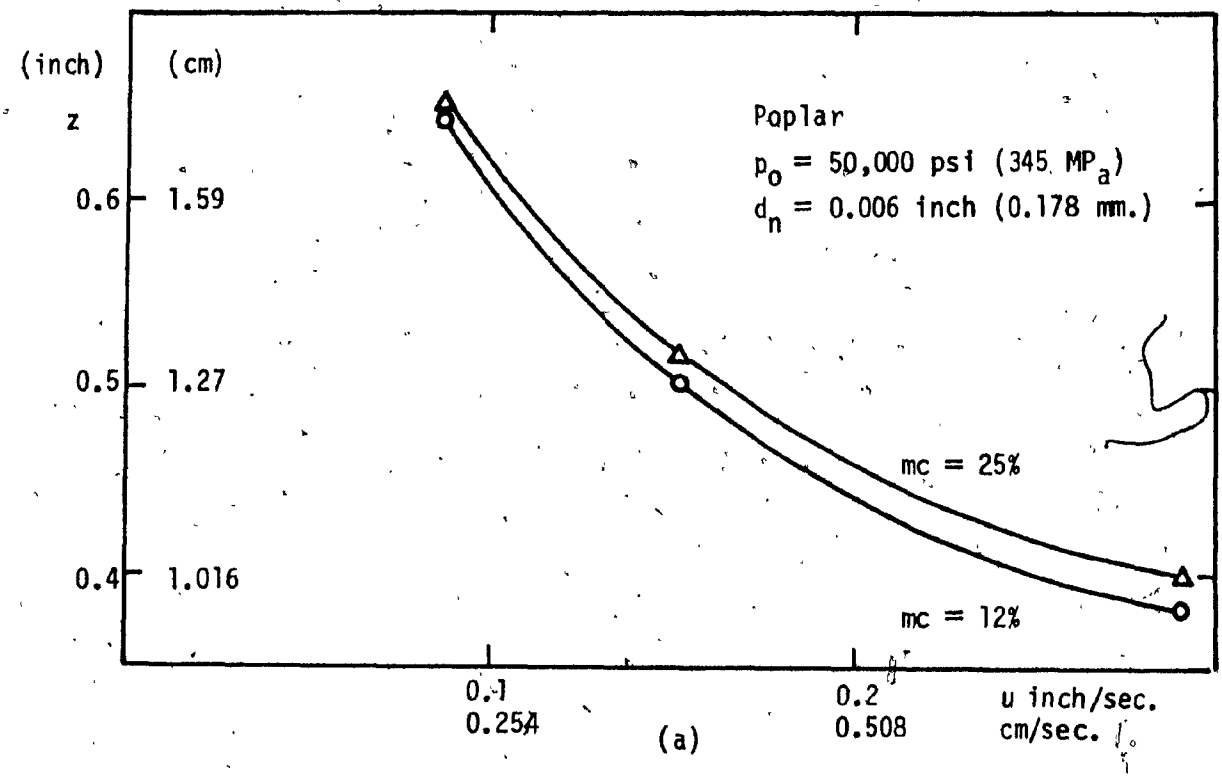

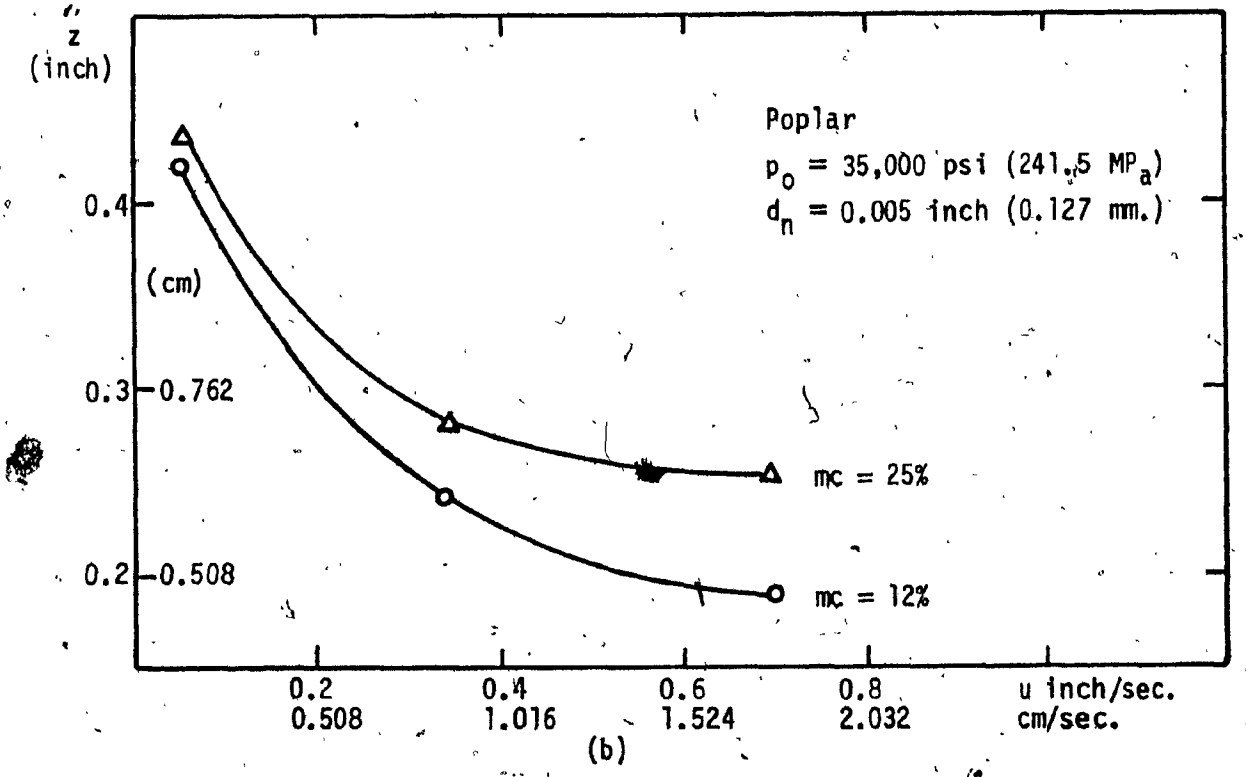

Fig. 3.2 Effect of Moisture Content (mc) on Depth of Cut (z) at Different Feed Rates (μ).

3.4 ANALYSIS OF EXPERIMENTAL DATA

The depth of cut (z) can be expressed as a function of the jet diameter (d_n), velocity (V) (or pressure), stand off distance (X), angle of incidence (Θ), the fluid density (ρ), the cutting speed (u) and the wood properties which, in the most general case, includes seven strength properties and the density (or specific gravity) which is obtained under three drying conditions. The purpose of this investigation is to find one strength property which is dominant in determining the depth and speed of jet penetration. This strength property, σ, must be identified from analysis of the experimental results. The required functional relationship for constant moisture content is:

$$z = f[d_n, V, \rho, X, \Theta, u, \rho_m, \sigma] \tag{3.2}$$

where ρ_m is the wood density.

For a fixed stand off distance and incidence angle and water with constant density, X, Θ and ρ can be eliminated and Eqn. (3.2) becomes:

$$z = f[d_n, V, u, s\rho, \sigma] \tag{3.3}$$

in which $s\rho$ is the wood density and s is the wood specific gravity. Dimensional analysis reduces the relationship between these six parameters to

$$\frac{z}{d_n} = f\left[\frac{u}{V}, \frac{s\rho V^2}{\sigma}\right] \tag{3.4}$$

in which both the mathematical form of the equation and the property σ must be obtained from the test results. In this equation, z/d_n is a

cutting depth number, u/V is a cutting speed and $\rho V^2/\sigma$ represents the ratio of cutting force per unit area to material strength. A systematic substitution for σ was carried out using each one of the seven strength properties and each one of the three densities listed in Table 3.1. The results indicated that none of the compressive-, shear- or tensile-strength properties taken by themselves results in a consistent mathematical function for Eqn. (3.4). Typically, non-dimensional results are shown in Figs. 3.3, 3.4 and 3.5 in which the cleavage strength (σ_{cL}) is used for σ and the basic (green volume weight over dry) density is used. This property may be considered to be representative of a complex failure mechanism similar to the jet cutting action. Although the results for each material have similar mathematical forms, there is no consistency in the numerical values of the non-dimensional parameter $\sigma_{cL}/s\rho V^2$ for different materials at corresponding values of v /u and $(z/d_n)_{ex}$. For instance, at fixed values of V/10000u of 10 and $(d/d_n)_{ex}$ of 50, the values of $(\frac{1000\ \sigma_{cL}}{s\rho V^2})$ are 0.041 for Poplar, 0.063 for Maple and 0.049 for Elm. The corresponding values at V/1000u = 30 and $(z/d_n)_{ex} = 70$ are 0.041, 0.074 and 0.049 for Poplar, Maple and Elm respectively, in which the "softer" Maple displays a higher strength to jet cutting force ratio than the "harder" Elm. Similar inconsistencies exist for each of the other strength characteristics.

The next step in the analysis of the data was to choose the mathematical form of the functional relationship, find the coefficients from the test data and then determine the combination of

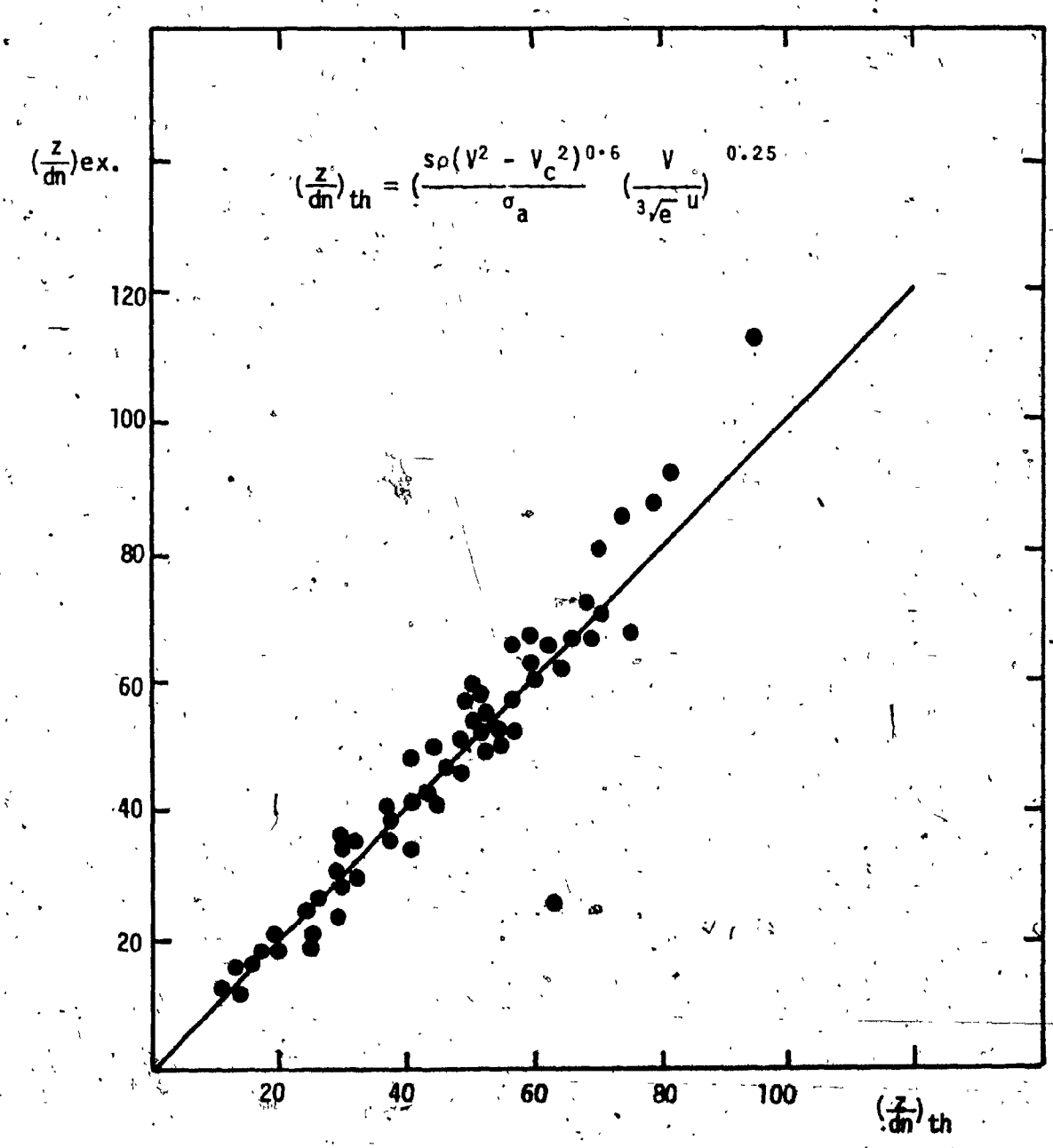

Fig. 3.7 Experimental vs. Theoretical Prediction of Depth of Cut Number (z/dn).

in which it is assumed that the kerf width equals the nozzle width. Substitution of $\frac{z}{d_n}$ from Eqn. (3.10) results in the following non-dimensional equation for the specific energy

$$\frac{SE}{\frac{\pi}{8}\rho V^2} = \left[\frac{\sigma_a}{s\rho(V^2 - V_c^2)}\right]^{0.6} \cdot \left[Re^{0.33}\left(\frac{V}{u}\right)^{0.75}\right]^{0.25} \qquad (3.12)$$

The effect of moisture content may be incorporated in Eqn. (3.11) by substituting from Eqn. (3.1)

$$\sigma_a = \sigma_d \, 10^{\alpha - \beta . mc} \qquad (3.13)$$

This leads to the final form of Eqn. (3.10)

$$\frac{z}{d_n} = \left[\frac{s\rho(V^2 - V_c^2)}{\sigma_d(10^{\alpha-\beta.mc})}\right]^m \left[\frac{V}{\sqrt[3]{\epsilon u}}\right]^n \qquad (3.14)$$

The constants α, β have to be determined by knowing the strength properties at two different moisture contents, the values are calculated based on the published data of Ref. (28).

Material	α	β
Poplar	0.15	1.25
Maple	0.11	0.924
Elm	0.143	1.199

3.5 CONCLUSIONS

The following conclusions are drawn:

1. The dominant properties that affect the depth of cut of wood are the density, the porosity and a root-mean-square value of the compressive, shear and tensile strengths normal and parallel to the grain .

2. The exponential Equation (3.14) with a threshold velocity below which no cutting occurs gives the best agreement with experimental results.

3. The nondimensional specific energy Equation (3.12) should be useful in estimating the energy requirements for other wood types with known physical properties.

CHAPTER 4

THEORETICAL AND EXPERIMENTAL INVESTIGATION OF CONTINUOUS JET PENETRATION OF SOLIDS - PHASE II.

4.1 INTRODUCTION

The process of material cutting and fracture by high velocity water jets is a complex series of phenomena which may involve compression, tension, shear, erosion, cracking, wave propagation, cavitation damage and wear. An exact analysis of the jet cutting process would be impossible because of the complexity of the interaction of these factors. In a particular application, the dominant mechanism depends on the following factors:

1. The type of load applied: water jets may be continuous or pulsating, the target may be moving or stationary and it could be very close to the nozzle exit or far from it. Fracture and cutting in each case may involve different mechanisms.
2. Type of material: cavitation may be an important mechanism in cutting granular materials with steady continuous jets. Tensile fracture may occur in cutting fibrous materials.
3. Feed rate: erosion and shear fracture may be the most important factors at fast feed rates while penetration at very slow feed rates may also involve other mechanisms such as compression failure and cavitation.

The purpose of this work is to find analytically the relationship between the parameters of a continuous jet, the material properties and the feed rate. The method used in the analysis involves the following:

1. Formulating a suitable control volume to determine the effect of the jet on the target.
2. Determining the hydrodynamic forces acting between the jet and the target.
3. Formulating models that describe the stress-strain relationships of the target materials when subjected to the hydrodynamic forces.

In each one of the steps, the particular method used must be adapted to suit the constraints of the other steps.

4.2 ANALYSIS

4.2.1 The Control Volume

Fig. 4.1 shows the control volume which surrounds the jet in the kerf. As the jet hits the target, it starts penetrating the material. The jet is resisted by the friction on the side walls of the cut and by the resistance of the material to fracture. The control volume is considered to be stationary in the horizontal plane because the depth of penetration in a small time interval is much greater than the horizontal displacement for most cutting applications. Typical experimental data are summarized in Table 4.1.

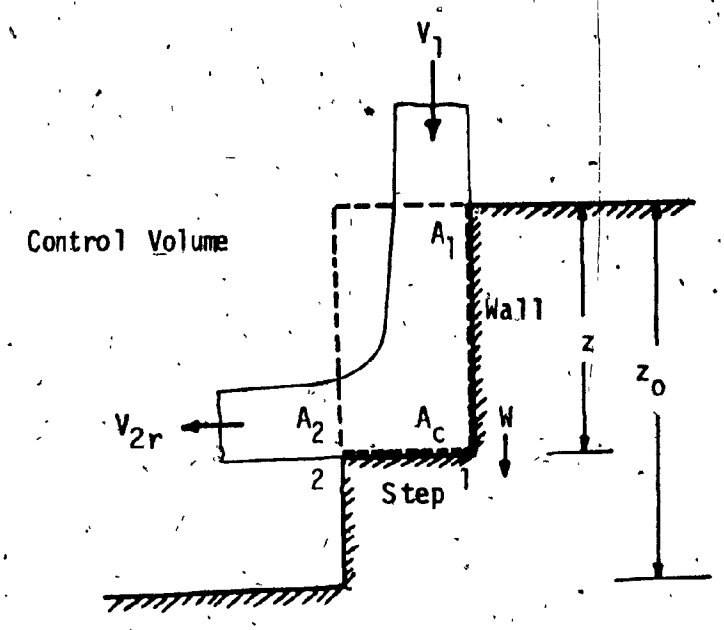

(a) The Control Volume

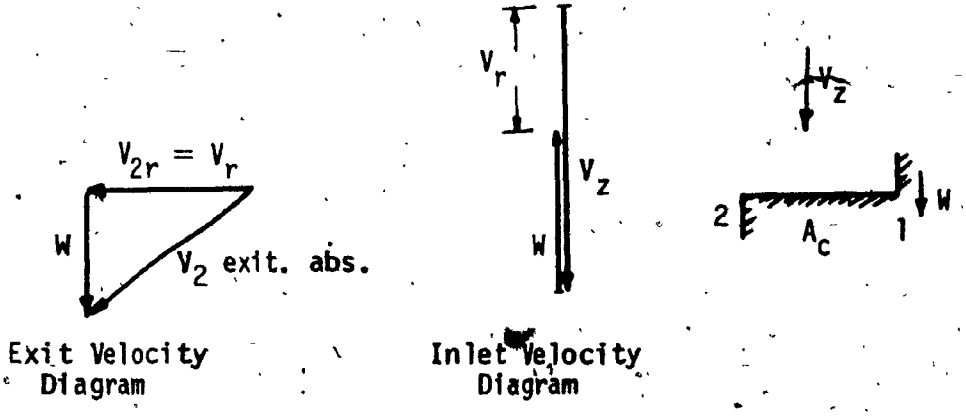

Exit Velocity Diagram

Inlet Velocity Diagram

(b) Velocity Diagrams

Fig. 4.1 The Control Volume and Velocity Diagrams.

Results with wood (1), (31), rocks (18), (19), (23), (25), coal (20), (21) and polymers (12) show that the mean velocity of penetration varies from 60 - 500 cm/sec. as compared to the lower feed rate range of 0.215 - 50 cm/sec.

Analysis of the cutting process therefore consists of determining the velocity W with which the control surface A_c advances into the material. The horizontal feed rate is approximated by a series of steps equal in size to the nozzle diameter which occur during the time required to reach the total depth of cut. This physical model of the cutting process was confirmed by high speed movie photographs taken during cutting tests in transparent plastic.

A typical film taken at a feed rate of 1.27 cm/sec. with a 0.0127 cm. diameter nozzle confirms the existence of a distinct cutting step A_c which deflects the jet through approximately 90^o. The cutting step moves vertically into the material with a quasi-steady downward velocity W during the time interval 0 to 10 microseconds. This physical observation supports the choice of a horizontally stationary control volume with one moving boundary A_c to model the cutting process.

Implicit in this model is the assumption that the cutting mechanism is governed by compressive forces that fracture the material on the cutting surface A_c. Shear stresses that act on the control surfaces decelerate the jet. As the kerf deepens, a critical velocity is reached where the compressive stress is insufficient to fracture

Ref. No.	Investigator	Material	Feed Rate inch/sec (u)	Mean Penetration Rate inch/sec (W)	Ratio W/u
	author	Elm	0.086	5.9	69
	author	Maple	0.3	15.6	52
	author	Poplar	0.156	14.4	92.3
1	Bryan	Sugar Maple	0.25	11.5	46
18	Harris	Indiana Limestone	2.28	142.5	62.5
21	Nikonov	Coal	11.79	589	50
20	Summers	Coal	3.28	342	74
25	Moodie	Red Woolten	19.6	1666	85
22	Northworthy	Concrete	2	56	28
12	Mohaupt & Burns	Poly-carbonate	0.8	34.3	43
23	Hurlburt & Crow	White Granite	1.6	80	50
23	Hurlburt & Crow	Wilkeson Sandstone	0.13	6.5	50
24	Galkins & Mellor	Ice	13.2	2431	187
19	Labus	Limestone	16	1504	94

inch/sec. = 25.4 mm/sec.

Table 4.1 Mean Value of Penetration Rate for Different Materials

the material and cutting stops. In typical cutting applications, approximate values of the shear stress calculated for turbulent boundary layers on rough walls (τ = 75 psi at z = 0.05 inch) are much lower than the shear strength of the material (σ_s = 500-5000 psi). The model is therefore based on the assumption that compression failure of the material is the dominant cutting mechanism.

4.2.2 Hydrodynamic Forces

The continuity and momentum equations for a deformable control volume (32) are used to determine the jet forces on the target.

The continuity equation

$$\frac{\partial}{\partial t} \int \rho dv = - \int_{c.s.} \rho V_{rn} \, dA \qquad (4.1)$$

reduces to

$$\dot{m}_{ext} = \rho [A_1 V_1 - A_c W] \qquad (4.2)$$

under the following assumptions (see Appendix A):

1. Density changes due to frictional heating can be neglected,
2. Area of cut A_c is constant.

The momentum equation is

$$g \int_{c.s.} \rho dv + F_{s.mech.} - \int_{c.s.} p.\vec{n}.dA + \int_{c.s.} \tau dA$$

$$= \frac{\partial}{\partial t} \int_{c.v.} \rho \vec{V} dv + \int_{c.v.} \rho . \vec{V} . V_{rn} \, dA \qquad (4.3)$$

The following assumptions are made to reduce the equation to the final form in the vertical direction:

1. The body force $g\,dv$ for a typical control volume of .02 cm^3 can by neglected.
2. The pressure force $\int_{c.s.} p.\tilde{n}.dA$ caused by small pressure gradients in the kerf can be neglected.
3. The shear force $F_{sh} = \int_{c.s.} \tau dA$ can be expressed as

$$F_{sh} = C_f \cdot A \cdot \frac{\rho V_1^2}{2} \tag{4.4}$$

where $A = \pi r_{cut}\, z$ and $A_c = \pi r_c^2$. (4.5)

The friction coefficient (33)

$$C_f = \frac{0.074}{\left(\frac{V_1 z}{\nu}\right)^{0.2}}$$

for hydraulically smooth turbulent flows, and

$$C_f = (1.89 + 1.62 \log \frac{z}{Ks})^{-0.25}, \quad 10^2 < \frac{z}{Ks} < 10^6$$

for hydraulically rough turbulent flows,

The wall roughness is affected by many factors such as the depth of cut, cutting speed, material properties and the jet size and initial velocity. Typical cuts vary from smooth at the top portion where the jet velocity is highest to rough at the bottom where the jet velocity is lowest. C_f will therefore be a mean value between the smooth and rough regimes.

Substitution of Eqn. (4.5) into Eqn. (4.4) gives

$$F_{sh} = C_f \cdot \rho \cdot \sqrt{A_c} \cdot z \cdot V_1 \qquad (4.6)$$

4. The vertical momentum flux

$$\int_{c.s.} \rho V V_{rn} dA = \dot{m}_{ext} V_{ex.v} - \dot{m}_{in} V_{in.v} = \dot{m}_{ext} W - \rho A_1 V_1^2$$

under the assumption that velocities are normal to the respective control surfaces. Substituting from the continuity equation (4.2) gives

$$\int_{c.s.} \rho V V_{rn} dA = \rho A_1 V_1 W - \rho A_c W^2 - \rho A_1 V_1^2 \qquad (4.7)$$

5. The rate of change of vertical momentum in the control volume can be approximated by

$$\frac{\partial}{\partial t} \int_{c.v.} \rho V dv \simeq \frac{d}{dt} [\rho \cdot V_{mean} \cdot A_c \cdot z]$$

$$= \frac{1}{2} \rho A_c V_1 + \frac{1}{2} \rho A_c V_2 W + \frac{1}{2} \rho A_c z \frac{dV_2}{dt} \qquad (4.8)$$

where $V_{mean} \simeq \frac{V_1 + V_2}{2}$ is the mean vertical velocity inside the control volume.

The final control volume equation is obtained by substituting Eqns. (4.6), (4.7) and (4.8) into Eqn. (4.3).

$$-F_{mech} - C_f \cdot \rho \cdot \sqrt{A_c}\, z\, V_1 = \frac{1}{2} \rho A_c V_1 \dot{z} + \frac{1}{2} \rho A_c V_2 \dot{z}$$

$$+ \frac{1}{2} \rho A_c \dot{V}_2 z + \rho A_1 V_1 \dot{z} - \rho A_c \dot{z}^2 - \rho A_1 V_1^2 \qquad (4.9)$$

in which $\dot{z} = \frac{dz}{dt}$, $\dot{V}_2 = \frac{dV_2}{dt}$.

The mean velocity V_2 of the jet just before the step is approximated by

$$V_2 \simeq V_1 - \frac{F_{sh}}{\dot{m}_{in}} \qquad (4.10)$$

Eqns. (4.9) and (4.10) contain three unknowns, F_{mech}, V_2 and z. The third equation needed for the solution is derived in the next section. It relates F_{mech} to the material properties and the penetration rate $\dot{z}$.

4.2.3 Material Resistance

The time dependence of strain of different materials to applied stresses can be neglected in most of the engineering problems where materials are stressed quasi-statically. In this problem, the time dependence of strain in response to the applied stresses has to be considered. The fact that the material does not respond instantaneously to the applied stress is the reason for the dependence of penetration on time and consequently, the dependence of depth of cut on the feed rate. The time effect can be modelled phenomenologically (34), (35), (36), (37) by a combination of simple mechanical elements which simulate elastic response, plastic response and yield. The success of the rheological models in elucidating the stress-strain behaviour of any material depends on the proper choice and arrangement of the elements of the model. Fig. 4.2a,b shows examples of rheological models for wood (37) and polymer (36). The Bingham model,

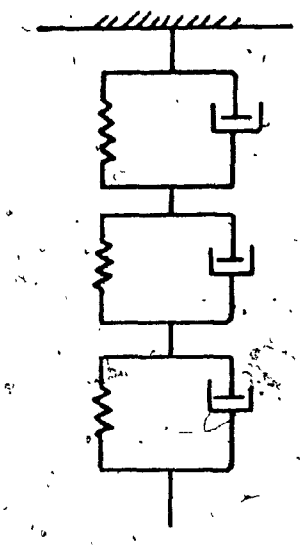

(a) Simplified Model of a Polymer

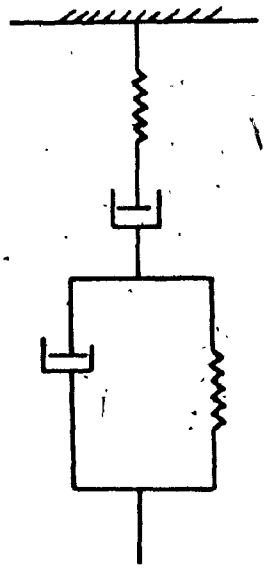

(b) Rheological Model for Wood

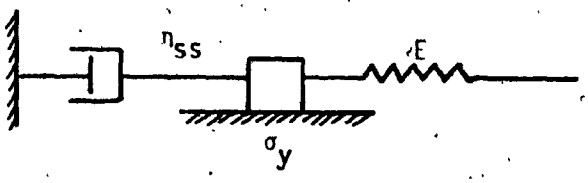

Bingham Substance

(c) Model of a Material with a Yield Point and Elastic-Plastic Characteristics

Fig. 4.2 Rheological Models for Typical Materials.

Fig. 4.2c, has a close relationship to the theory of plasticity (35). The present analysis uses the simplified Bingham model where the yield behaviour is analogous to the jet cutting process, which starts only when the velocity exceeds a certain minimum value. The stress-strain relationship for the Bingham model is

$$\begin{aligned} \sigma - \sigma_y &= \eta_{ss} \dot{\varepsilon} \ , \ \sigma > \sigma_y \\ \sigma &= E_\varepsilon \ , \ \sigma < \sigma_y \end{aligned} \tag{4.11}$$

where η_{ss} is the damping factor depending on stress and strain rate.

Multiplication by the area A_c results in the required force-displacement equation

$$\begin{aligned} F_{mech} - F_y &= A_c \eta \dot{z} \\ \sigma A_c - \sigma_y A_c &= \eta A_c \dot{z} \end{aligned} \tag{4.12}$$

where η is the damping factor depending on force and deflection rate. The conditions for jet cutting are

$$\sigma > \sigma_y \geq \sigma_c$$

where σ_c is the fracture stress value of the material. For these conditions, the required equation is

$$F_{mech} - \sigma_y A_c = \eta A_c \dot{z} \tag{4.13}$$

Eqns. (4.9), (4.10) and (4.13) can be solved for F_{mech}, $\dot{z}$, V_2.

4.2.4 Solution of the Simplified Equations

The penetration rate is much higher than the feed rate, but it is much less than the minimum jet velocity. A direct conclusion from this is that the hydrodynamic force can be calculated from Eqn.(4.9) which simplifies to

$$F_{mech} = \rho A_1 V_1^2 - C_f \cdot \rho \cdot \sqrt{A_c}\, z\, V_1^2 \qquad (4.14)$$

Assuming that the area of cut equals the nozzle exit area and solving Eqn. (4.14) with Eqn. (4.13) results in

$$z = \frac{\rho A_1 V_1^2 - \sigma_y A_1}{\frac{\sqrt{\pi}}{2} \cdot C_f \cdot \rho d_n V_1^2} \left[1 - e^{-\frac{2C_f \cdot \rho \cdot V_1^2}{\eta \sqrt{\pi}\, d_n} t}\right] \qquad (4.15)$$

The time t can be related to the feed rate and nozzle diameter by $t = \frac{d_n}{u}$, and the equation can be written in a nondimensional form

$$\left(\frac{z}{d_n}\right) = \frac{1 - \left(\frac{\sigma_y}{\rho V_1^2}\right)}{\left(\frac{2C_f}{\sqrt{\pi}}\right)} \left[1 - e^{-\left(\frac{2C_f}{\sqrt{\pi}}\right) \cdot \left(\frac{\rho V_1}{\eta}\right) \cdot \left(\frac{V_1}{u}\right)}\right] \qquad (4.16)$$

The nondimensional groups $\left(\frac{z}{d_n}\right)$, $\left(\frac{\sigma_y}{\rho V_1^2}\right)$, $\left(\frac{V_1}{u}\right)$ have been used in other published equations (1), (4), (7), and (10), for fixed stand off distance. However, the groups $\frac{\rho V_1}{\eta}$, $\frac{2C_f}{\sqrt{\pi}}$ have not appeared in other published work. An expression for the specific energy (SE) can be derived from Eqn. (4.16).

$$SE = \frac{\frac{1}{2}\dot{m} V_1^2 \cdot t}{(\frac{\pi}{4}) d_n^2 z} = \frac{\text{energy input}}{\text{volume removed}}, \quad \dot{m} = \text{jet flow rate}$$

or

$$\frac{u \cdot SE}{\rho V_1^3} = \frac{1}{[F_n - F_n \cdot S_n][1 - e^{-E_n \cdot V_n \cdot / F_n}]} \qquad (4.17)$$

where $F_n = \frac{\sqrt{\pi}/4}{C_f}$ Friction Number

$S_n = (\frac{\sigma_y}{\rho V_1^2})$ Yield Strength Number

$E_n = (\frac{\rho V_1}{\eta})$ Damping Number

$V_n = (\frac{V_1}{u})$ Velocity Ratio Number.

4.3 EXPERIMENTAL RESULTS

4.3.1 Coefficient of Friction

The friction coefficient C_f in Eqn. (4.14) can be determined experimentally from zero or very low feed rate data. The maximum depth of cut z_o achieved after a long time is

$$\frac{z_o}{d_n} = \frac{1 - (\frac{\sigma_c}{\rho V_1^2})}{(\frac{2C_f}{\sqrt{\pi}})} \qquad (4.18)$$

Data from different sources (1), (12), (18), (19), (22), (31) have been used to determine the friction factors for different materials. In Eqn. (4.18), σ_c is taken as the compressive fracture strength of the material. Fig. 4.3 is a plot of results obtained with different types of wood at zero feed rate. The tests were conducted with a range of nozzle diameters and driving pressures. Friction coefficients for other materials are listed in Table 4.2. When compared with flat, plate friction factors, these values of C_f are distributed in the hydraulically rough turbulent flow regime. This provides some justification for the use of Eqn. (4.18) to determine values of C_f for different materials.

4.3.2 Damping Coefficient

The damping coefficient η in Eqn. (4.16) is not a known material property but its value for a particular material can be calculated from Eqn. (4.16) using experimentally determined cutting depths z with the appropriate values of σ_y, C_f, d_n, V_1 and u.

Table 4.2 lists the calculated values of η for different materials. Each value of η is the mean for several test results and the maximum percentage deviation indicates the variation in the value for a particular material. The correlation coefficient listed in Table 4.2 reflects the variation in measured depth and the depth calculated from Eqn. (4.16) using the mean value of η for that material. The calculated values of η are highest for wood, 1.7×10^9 to 3.3×10^9 Kg/m^{2}sec. Values for sandstone, limestone, granite and

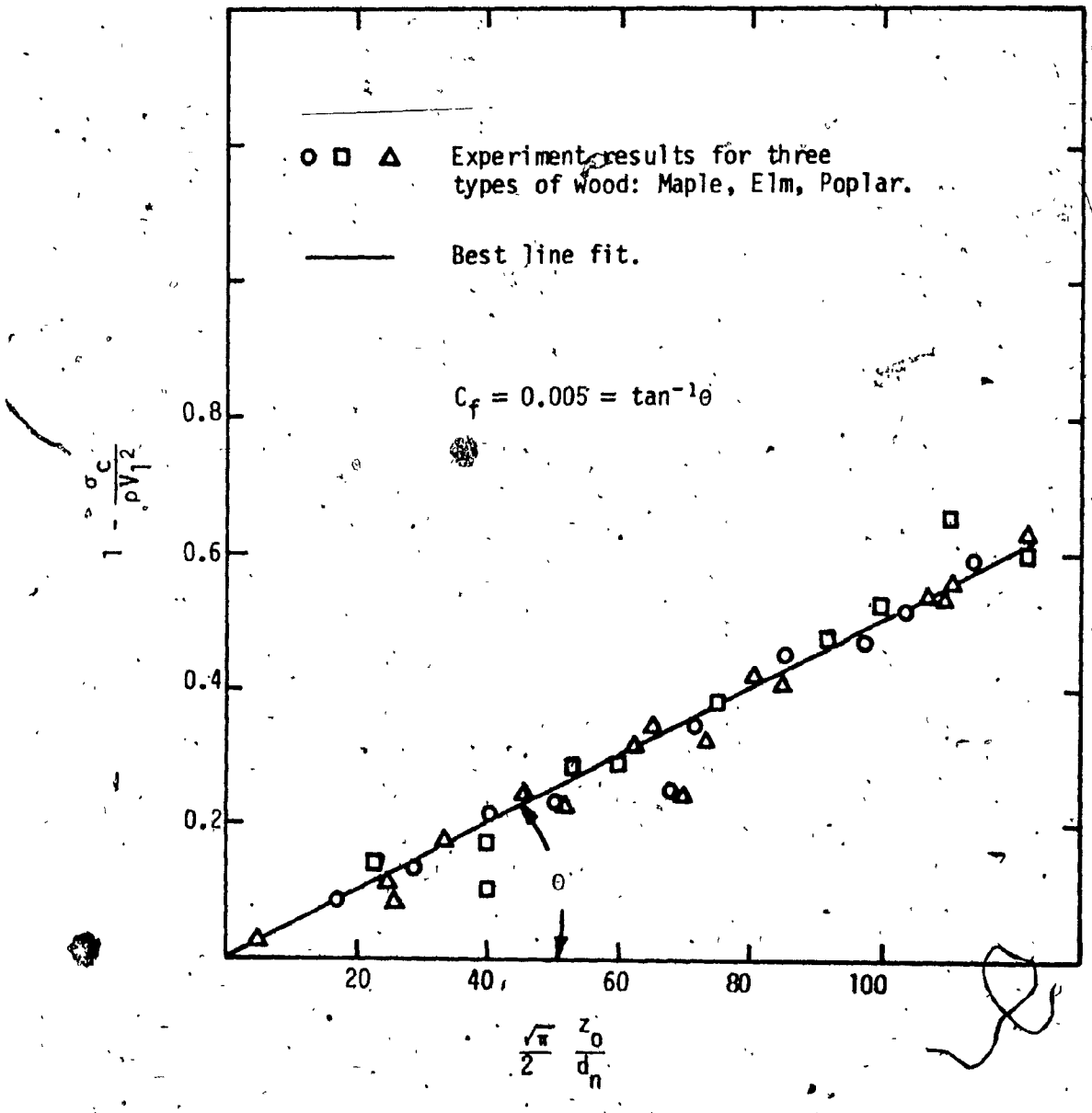

Fig. 4.3 Mean Value of the Coefficient of Friction (C_f) For Poplar, Maple and Elm

Ref. No.	Investigator	Material	Compressive Strength psi	Yield Strength psi	Friction Coef. C_f	Damping Coef. η Slug/ft^{2}s.	Max. % Dev. from/ η_{mean}	Correl. Coef.	No. of Tests
	Author	Maple	3800***	560	.005	1.5×10^7	1%	.9235	27
	Author	Elm	4080***	810	.005	2.1×10^7	1.2%	.9116	27
	Author	Poplar	2110***	290	.005	1.1×10^7	0.9%	.9317	27
1	Bryan	Sugar Maple	4560	850	.005	3.9×10^6	7%	.7511	7
18	Harris	Indiana Limestone	7600	700	.006	3.9×10^6	5.1%	.8470	9
21	Nikonov	Coal	1000***	200	.007	7513	.89%	.9623	5
20	Summers	Coal		500	.008	1.1×10^5	.95%	.9413	14
25	Moodie	Red Woolten	5217	800	.008	4.2×10^4	.86%	.9603	6
22	Northworthy	Concrete	3750	700	.01	1.4×10^6	2%	.8904	9
12	Mohaupt & Burns	Polycarbonate	12500*	5000	.008	2.99×10^6	2.3%	.8719	10
23	Hurlburt & Crow	White Granite	19500	1000	.015	8.7×10^5	.56%	.9838	10
23	Hurlburt & Crow	Wilkeson Sandstone	8300	600	.014	1.67×10^6	.5%	.9881	10
24	Calkins & Mellor	Ice		300	.0004	2.18×10^4	1.4%	.9010	8
19	Labus	Limestone	4785	600	.006	5.2×10^5	1.1%	.9113	10

* Given in other references.
** Calculated from reference data.
*** Crushing strength is used.

psi = 6.9×10^3 Pa
slug/ft^{2}sec. = 156.96 kg/m^2. sec.

Table 4.2: List of Material Properties Used in Equation (4.16)

concrete range from 7.8×10^7 to 6.3×10^8 Kg/m^2.sec. while values for hard and soft coal vary from 1.2×10^6 and 1.8×10^7 Kg/m^2.sec.

4.3.3 Comparison of Simplified and Exact Solutions

Eqns. (4.9),(4.10) and (4.13) have been solved simultaneously using a "MIMIC" Computer Program. The results obtained from these equations and from the simplified steady state equation (4.16) using the predetermined friction factor and damping factor are plotted in Fig. 4.4 for Elm. Comparison between the two solutions for other materials indicate a maximum difference of 2% in depth of cut data. This comparison shows that the simplified equation is adequate for typical cutting operations where the feed rate and penetration rate are small relative to the critical jet velocity.

4.3.4 Graphical Presentation of the Cutting Equation

The cutting equation (4.16) gives the relationship between five nondimensional groups. Graphical presentation is limited to showing the relationship between three groups for constant values of the remaining groups.

Figs. 4.5 and 4.6 are typical plots for constant values of the strength number and the friction coefficient. The cutting characteristics of a particular material at a fixed jet velocity is represented by the curve with the appropriate fixed value of the damping number. The characteristic curve gives the relationship between the cutting depth number and the cutting speed number for that material at the particular jet velocity. Experimental results for typical

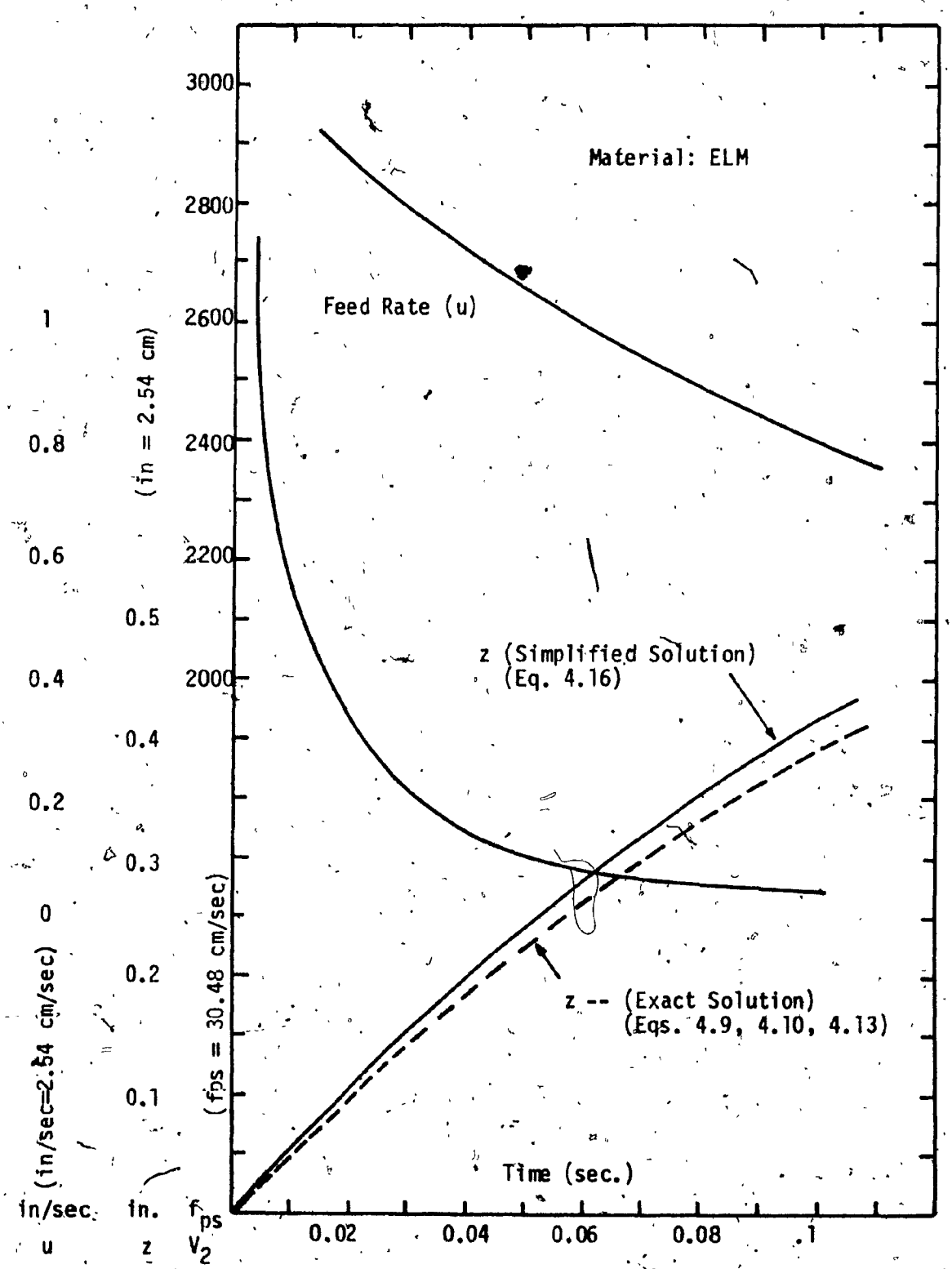

Fig. 4.4 Graphical Representation of the Solution of the Theoretical Cutting Equations (4.9), (4.10), (4.13) and (4.16).

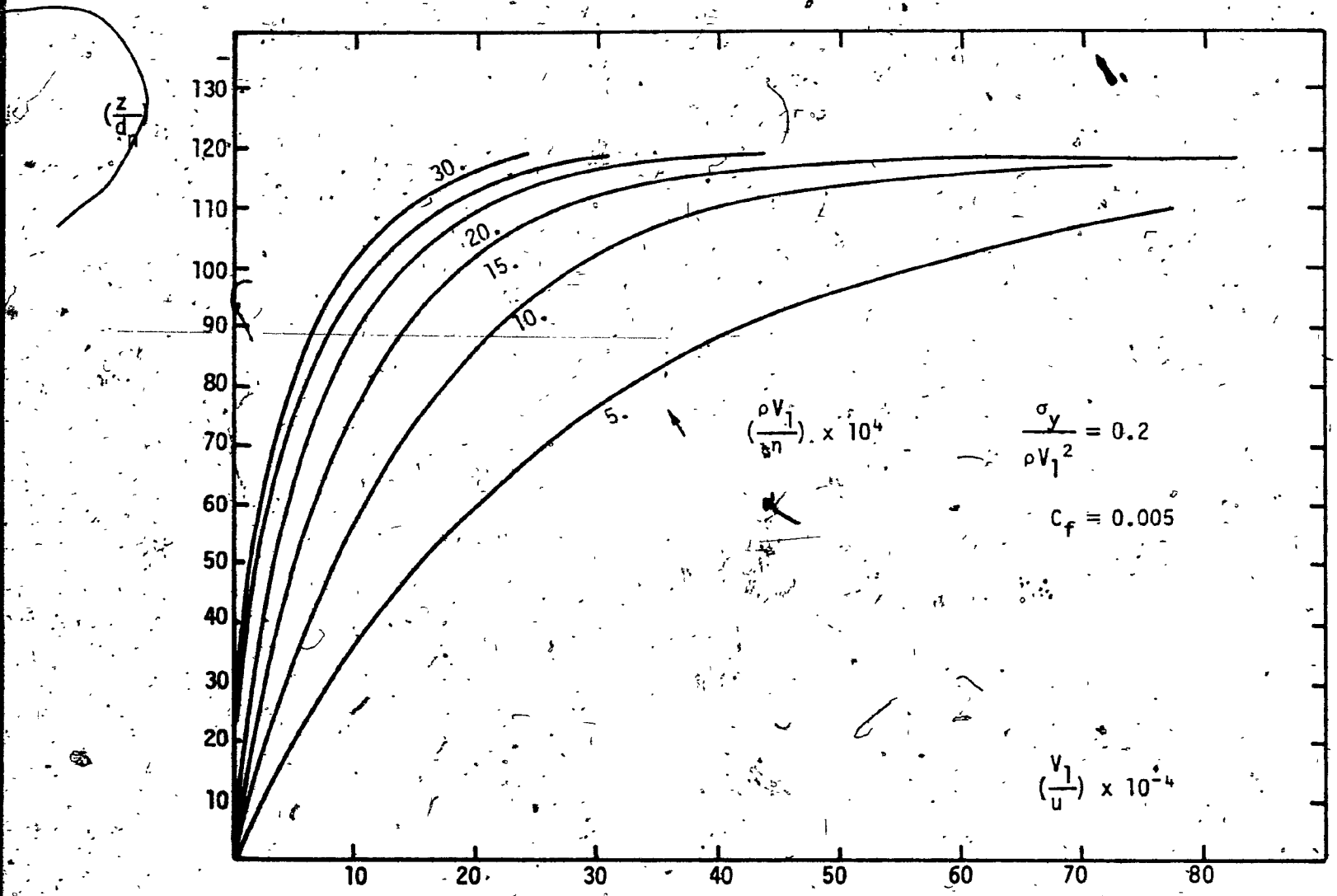

Fig. 4.5 Depth of Cut Number as a Function of Velocity and Damping Numbers for Constant Strength and Friction Numbers.

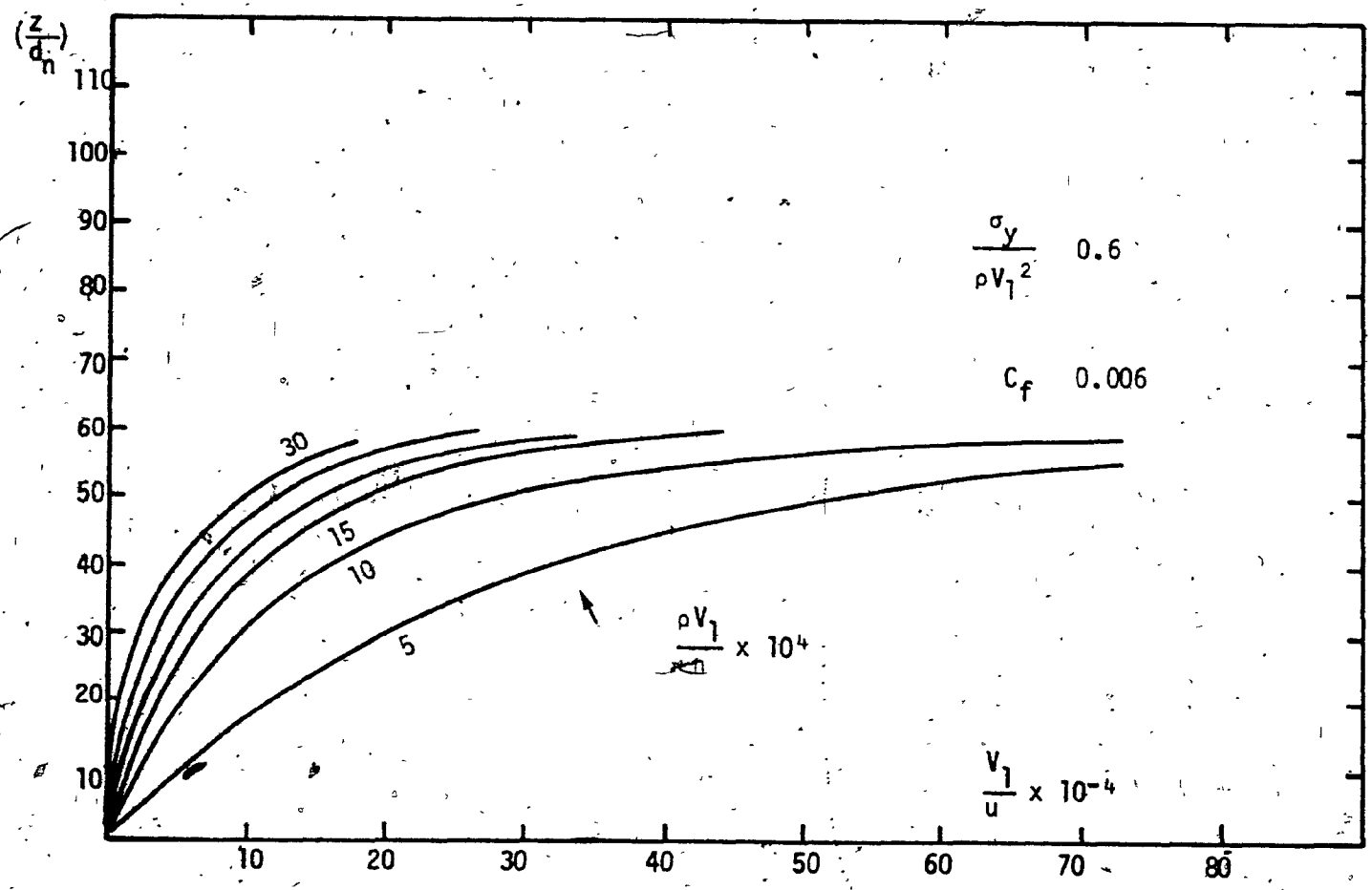

Fig. 4.6 Depth of Cut Number as a Function of Velocity and Damping Numbers for Constant Strength and Friction Numbers.

applications follow these curves almost exactly in cases where the damping coefficient of Table 4.2 has low standard deviations. The number of plots required for the graphical representation can be reduced to one if Eqn. (4.16) is rewritten in the form

$$\frac{z}{d_n} = N_1 = N_2 \left[1 - e^{-N_3}\right] \qquad (4.19)$$

N_2 and N_3 are new nondimensional numbers.

$$N_2 = \frac{1 - \frac{\sigma_c}{\rho V_1^2}}{2C_f / \sqrt{\pi}}$$

$$N_3 = \frac{2C_f}{\sqrt{\pi}} \cdot \frac{\rho V_1}{\eta} \cdot \frac{V_1}{u}$$

Fig. 4.7 is a logarithmic plot of Eqn. (4.19) which is rewritten as

$$\log_{10} \frac{N_2}{N_2 - N_1} = \frac{1}{2.3} N_3$$

The number N_3 may vary from 0.0 to ∞ depending on the values of the feed rate, n, V_1 and C_f.

Experimental data from the sources listed in Table 4.2 are also presented in Fig. 4.7. There is a high overall correlation between Eqn. (4.19) and the experimental data considering the wide variety of materials and allowing for differences in test conditions and the accuracy of experimental data.

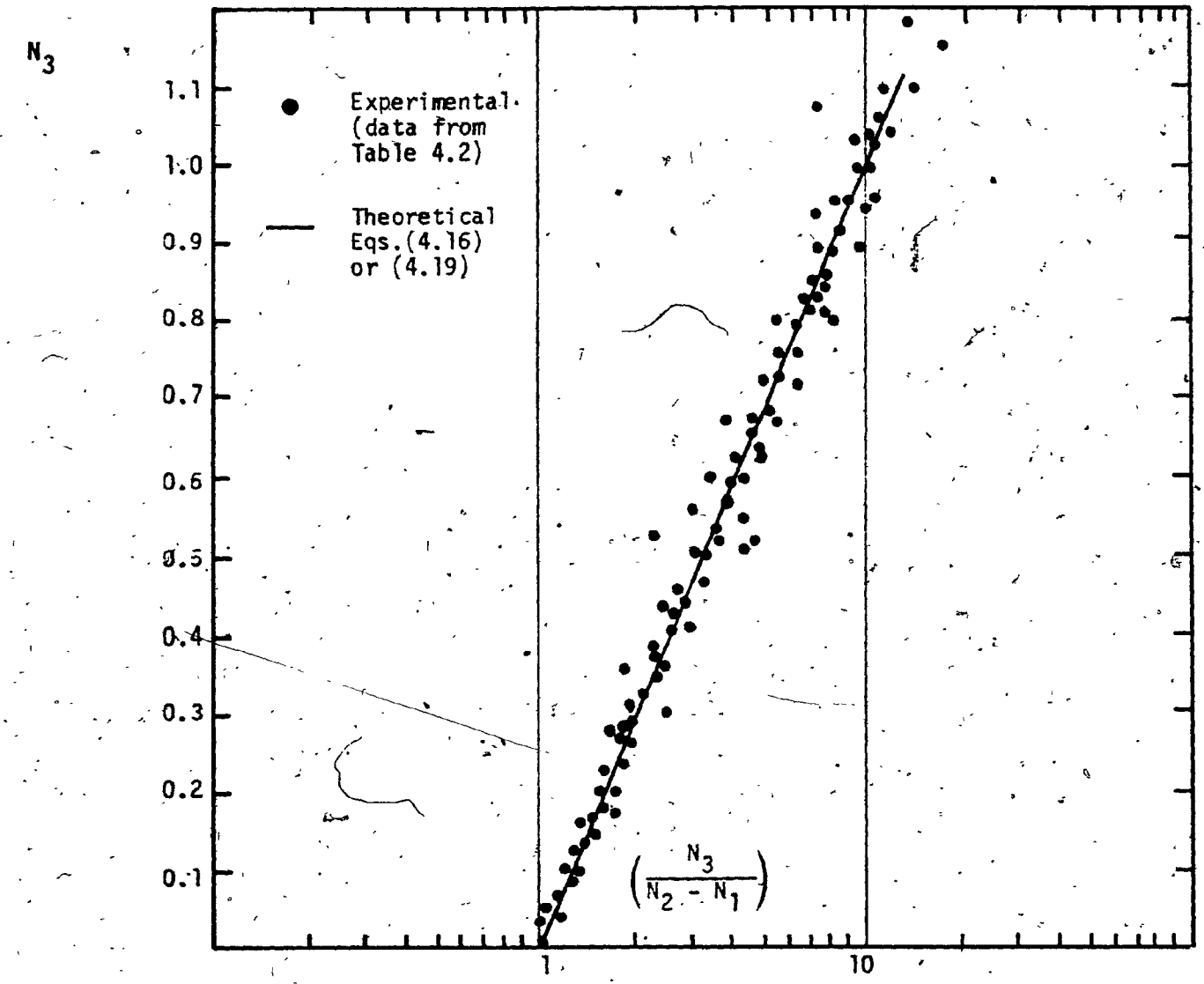

Fig. 4.7 Comparison Between Experimental Results and Theoretical Equation (4.16).

4.4 CONCLUSION

This study has attempted to develop a theory that describes the cutting behaviour of a wide variety of materials. The theory is based on a control volume analysis to determine the hydrodynamic forces acting on the solid boundaries in the cutting slot. The Bingham-plastic model is used to describe the time dependent stress-strain relationship of the solid material. This model is not necessarily the optimum for each one of the materials considered in the study. However, its simplicity leads to a closed form solution of the coupled fluid-solid mechanics equations. It also permits convenient characterization of different materials by means of a compressive yield stress, a damping coefficient and a hydrodynamic friction coefficient.

The equation describes the cutting behaviour of materials with structures ranging from fibrous, crystalline to granular. The method presented can be adapted to give greater accuracy for a particular material by choosing the optimum rheological model for that material.

CHAPTER 5

APPLICATION OF THE THEORY TO PREDICT THE EFFECT OF STAND OFF DISTANCE ON CUTTING RESULTS - PHASE III

5.1 INTRODUCTION

The analysis of Chapter 4 assumes that the jet velocity V_1 remains constant between the nozzle exit and the control volume entrance surface and it does not take into consideration the actual spreading characteristics discussed in Section 2.2.4. Fig. 5.1 is a simplified representation of the jet spreading behaviour in the air. Two regions are identified, the initial region and the main region. In the initial region, the jet velocity remains constant and the width increases proportional to the distance from the nozzle. In the main region, the centerline velocity of the jet decreases approximately proportional to the square root of distance (X) from the nozzle exit. Section 5.2 describes the jet behaviour in detail. The effect of jet spreading and velocity decay on the resulting cutting action at different stand off distances depends on the region of the jet in which cutting occurs and on the characteristics of the material. This chapter investigates the following possible effects of stand off distance for certain combinations of initial jet velocity and size, cutting conditions and material properties:

1. The existance of optimum stand off distances for maximum depth of cut and maximum volume of material removed.

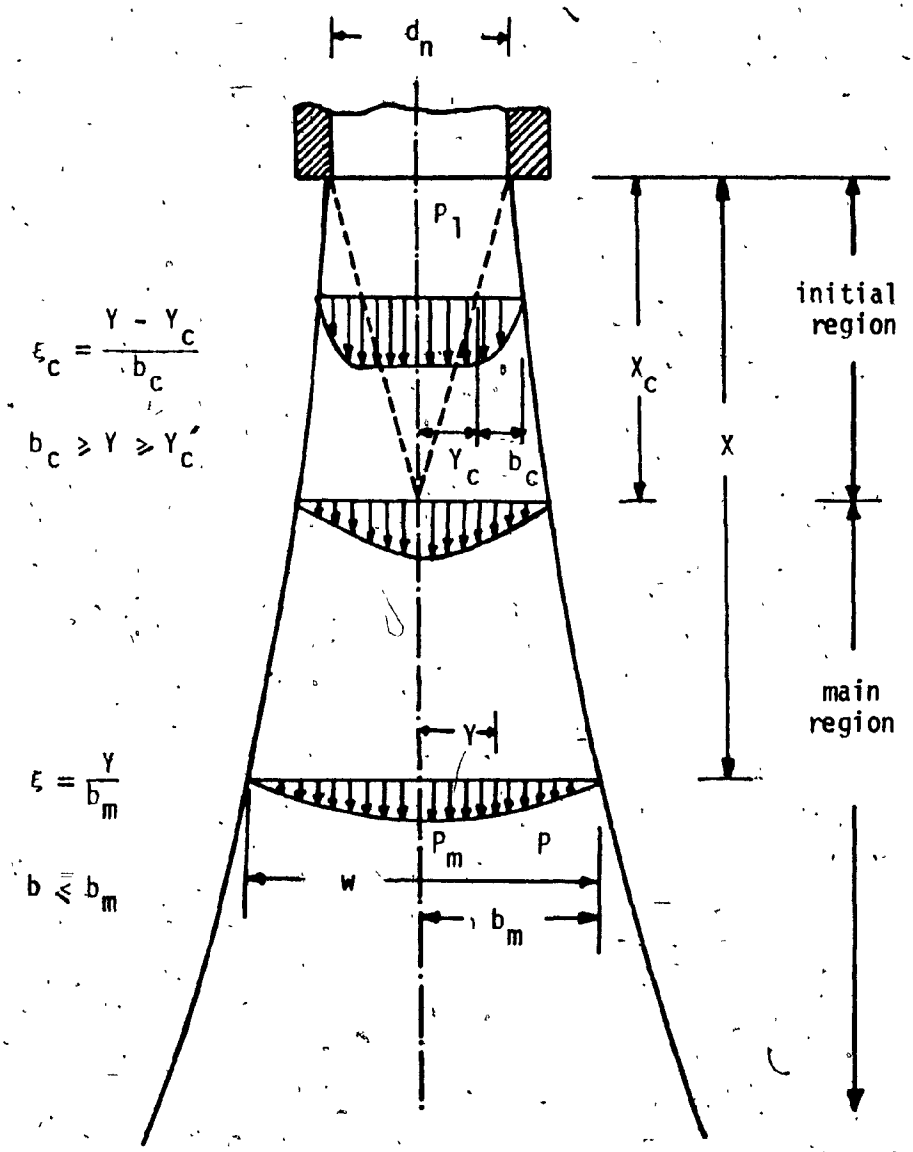

Fig. 5.1 Parameters For Jet Spreading in Air.

2. The existance of optimum feed rates and number of passes for maximum depth of cut and volume of material removed.
3. The existance of an optimum cutting efficiency (or specific energy). Analysis of the effect of stand off distance involves the jet spreading behaviour and the dynamics of penetration of the solid material.

5.2 THE EFFECT OF STAND OFF DISTANCE ON JET STRUCTURE

Eqn. (4.16) is used along with Yanaida's (15) results on the mechanics of jet spreading to develop nondimensional equations for the effect of stand off distance. Shavlovsky (38), Leach and Walker (16) and Abramovich (39) published some work on the mechanics of jet spreading, but Yanaida's results will be used here since it is the most recent work and correlates well with in-house experimental data as described in Section 2.2.4.

The axial and radial dynamic pressure decay characteristics are summarized in Table 5.1 and are presented graphically in Fig. 5.1.

Distribution	Region	Equation	Remarks	
Axial	Initial	$P_m = P_1$	$X < X_c$	(5.1)
	Main	$P_m/P_1 = X_c/X$	$X > X_c$	(5.2)
Radial	Initial	$P/P_m = (1 - \xi_c^{3/2})^2$	$\xi_c = Y-Y_c/b_c$	(5.3)
	Main	$P/P_m = (1 - \xi^{3/2})^2$	$\xi = Y/b_m$	(5.4)

Table 5.1 Axial and Radial Dynamic Pressure Distribution.

The average dynamic pressure across the jet that produces the equivalent jet hydrodynamic force on the material is calculated from Eqns. (5.1) to (5.4) (details are given in Appendix B) and the results are summarized in Table 5.2 following.

Region	Average Pressure
Initial	$P_{av.} = P_1 \dfrac{Y_c^2 + 0.257\, b_c^2}{(Y_c + b_c)^2}$ (5.5)
	$Y_c = \dfrac{dn}{2} \left(\dfrac{X}{X_c} - 1\right)$ (5.6)
	$b_c = \dfrac{0.335}{2} \sqrt{d_n X_c} \left(\dfrac{X}{X_c}\right)$ (5.7)
Main	$P_{av.} = 0.257\, P_1 \left(\dfrac{X_c}{X}\right)$ (5.8)

Table 5.2 Average Dynamic Pressure in the Two Jet Regions.

In this analysis, it is assumed that the jet spreads linearly in the initial region and proportional to the square root of distance from nozzle exit in the main region. The equation in the main region is

$$w = 0.335 \sqrt{d_n X}$$

or

$$\frac{w}{d_n \sqrt{R}} = 0.335 \sqrt{\frac{X}{X_c}} \qquad (5.9)$$

where $R = X_c/d_n$

The published data on the length of the initial region X_c vary according to parameters such as nozzle shape and pressure. Table 5.3 lists typical values of X_c.

Reference	$R = X_c/d_n$	Reference	$R = X_c/d_n$
Yanaida (15)	30 - 100	Chyapko *	100
Geyer *	140	Shavlovsky (38)	0.0 - 110

* Cited in Ref. (40).

Table 5.3 Reference Data for Length of Initial Jet Region.

In the main region of the jet, the effective diameter of the jet w_e, that is, the width within which the dynamic pressure satisfies the condition $\sigma_c \leq \rho V^2 = 2P$ can be determined from Eqns. (5.4) and (5.9) as shown in Appendix C. The resulting equation in a nondimensional form is

$$\frac{w_e}{d_n\sqrt{R}} = 0.335\sqrt{\frac{X}{X_c}}\left[1 - \sqrt{\frac{\sigma_c}{2P_1}\,\frac{X}{X_c}}\right]^{2/3} \qquad (5.10)$$

Fig. 5.2 is a plot of the jet profile in terms of the nondimensional numbers of Eqn. (5.10)

Width number	$\frac{w_e}{d_n\sqrt{R}}$
Strength number	$\frac{\sigma_c}{P_1}$
Stand off Distance Ratio	$\frac{X}{X_c}$

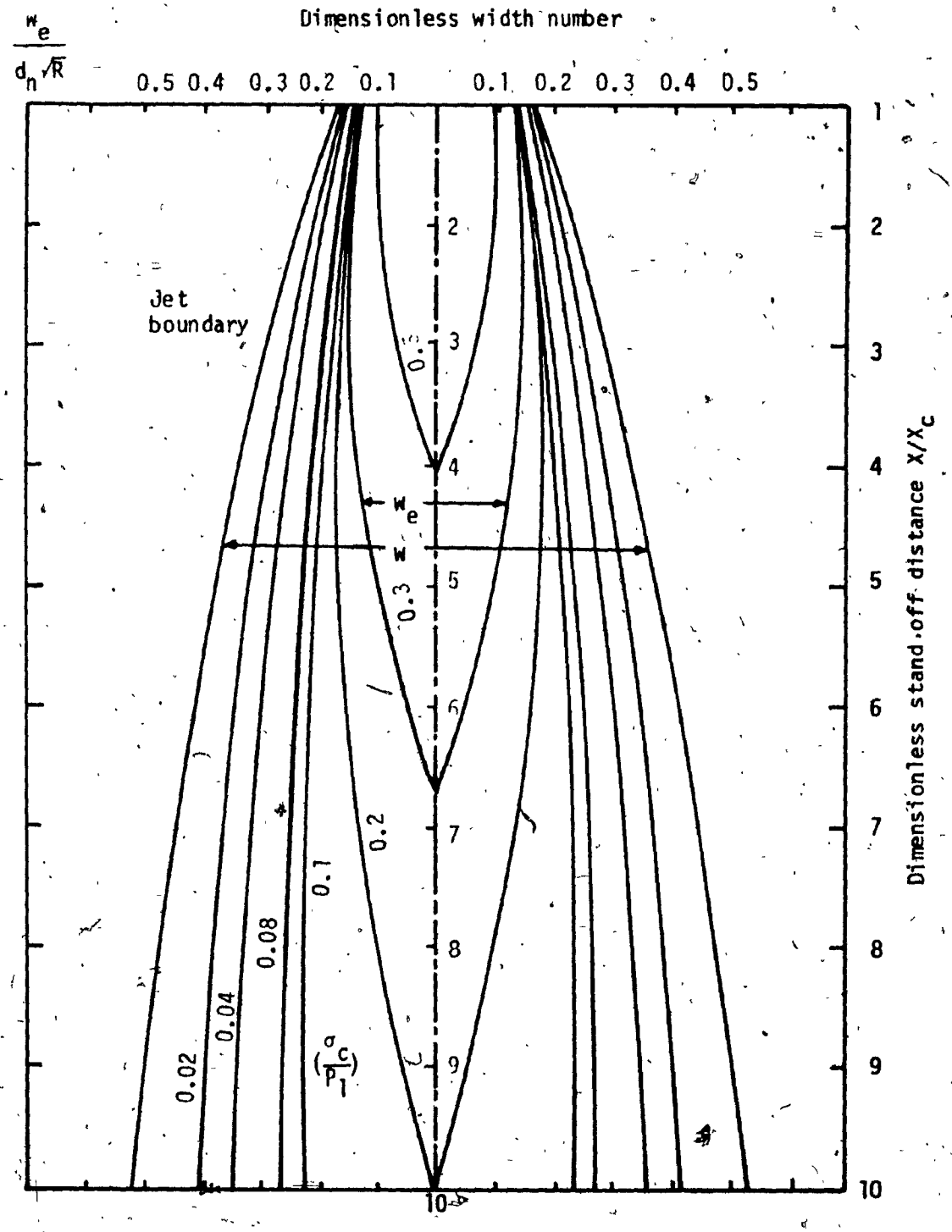

Fig. 5.2 Jet Spreading Profile and Effective Width for Different Strength Numbers (σ_c/P_1).

The equation can also be solved for different ranges of the cutting strength number. The range chosen here with an upper limit of $\sigma_c/P_1 = 0.5$ includes most of the published test results. Inspection of Eqn. (5.10) and Fig. 5.2 leads to the following observations.

1. Each cutting condition can be defined by a particular value of the strength number and the corresponding contour line of Fig. 5.2 defines the portion of the jet which is effective in cutting the material. The portion of the jet core is called the effective diameter (or width) w_e which either increases or decreases as the stand off distance ratio $\frac{X}{X_c}$ increases depending on whether $\frac{\sigma_c}{P_1}$ is either greater or less than about 0.1 to 0.5. The contour line for $\sigma_c/P_1 = 0.5$ shows a continuously decreasing value of w_e as X/X_c increases, and since P_1 also decreases with distance, no optimum value of stand off distance can be expected for $\sigma_c/P_1 \geq 0.5$.

2. For conditions where $\sigma_c/P_1 \leq 0.04$, that is, when the material is soft and the pressure is high (as in soft wood cutting), the effective diameter remains only slightly smaller than the actual jet diameter up to stand off numbers $(\frac{X}{X_c})$ of about 6.

3. From Eqn. (5.10) it follows that for constant pressure, w_e is proportional to d_n, the nozzle diameter; and from Eqn. (4.16), it was concluded that $d_n \propto z$, the depth of cut; therefore, $z \propto w_e$. Because w_e increases and the dynamic pressure decreases as $\frac{X}{X_c}$ increases, the depth of cut z will either increase or decrease depending on which effect is dominant. An optimum stand off

distance can therefore be expected under certain combinations of the nondimensional numbers.

4. The limiting stand off distance can be calculated from Eqn. (5.10) by substituting $w_e = 0.0$, to obtain

$$X_{lim.} = \frac{2P_l}{\sigma_c} X_c$$

i.e. $$\frac{X_{lim.}}{d_n} = 2 \cdot R \cdot \frac{P_l}{\sigma_c} \qquad (5.11)$$

At this distance, $\frac{\sigma_c}{2P_m} = 1$, that is, the compressive strength equals the hydrodynamic stress of the jet on the material and no cutting occurs. For distances where $X > X_{lim.}$, the jet may cause plastic deformation or fatigue in the material due to repeated impact of water drops which may form at this stand off distance.

The average pressure within the effective width of the jet is used in the next section. It is determined in Appendix D for the main region from Eqns. (5.4) and (5.10). The resulting equation is

$$P_a = 2P_l \frac{X_c}{X} (0.5 - 0.57 \psi + 0.2 \psi^2)$$

where $$\psi = (1 - \sqrt{\frac{\sigma_c}{2P_l} \frac{X_l}{X_c}}) \qquad (5.12)$$

The analysis presented in the following sections makes use of these derived equations of jet effective width and average dynamic pressure.

5.3 EFFECT OF STAND OFF DISTANCE ON DEPTH OF CUT

The existance of an optimum stand off distance for maximum depth of cut has been observed in cutting of aluminium (26) and concrete (41) with continuous water jets and in cutting granite with a cavitating jet (42).

To explain this phenomena quantitatively, the cutting equation

$$\frac{z}{d_n} = \frac{\sqrt{\pi}}{2C_f}\left(1 - \frac{f\sigma_y}{\rho V_1^2}\right)\left(1 - e^{-\frac{2C_f}{\sqrt{\pi}} \cdot \frac{\rho V_1}{n} \cdot \frac{V_1}{u}}\right) \qquad (4.16)$$

is used together with the following substitutions for d_n and V_1:

1. d_n is replaced by the effective width of the jet calculated from Eqn. (5.10).
2. V_1 is replaced by the average velocity which in turn is calculated from the average pressure given by Eqn. (5.12).

Substitutions 1 and 2 in Eqn. (4.16), and arrangement of terms as detailed in Appendix E, result in the following composite non-dimensional equation

$$\frac{zC_f}{d_n\sqrt{R}} = 0.297\sqrt{\frac{X}{X_c}} \cdot \psi^{2/3} \cdot \left[1 - \frac{\sigma_y}{2P_1\phi}\left(1 - e^{-2.256\frac{C_f P_1}{nu}\phi}\right)\right] \qquad (5.13)$$

where $$\psi = \left(1 - \sqrt{\frac{\sigma_c}{2P_1} \cdot \frac{X}{X_c}}\right)$$

$$\phi = 2\left(\frac{X_c}{X}\right)\left[0.5 - 0.57\,\psi + 0.2\,\psi^2\right], \text{ using } P_1$$

or $\phi = 2\left(\frac{X_c}{X}\right) \cdot C_{D_o}^2 \left[0.5 - 0.57\,\psi + 0.2\,\psi^2\right]$ if P_o

is used in Eqn. (5.13) instead of P_1.

The five nondimensional groups in Eqn. (5.13) are:

1. Dimensionless stand off distance $X_N = X/X_c$
2. Yield strength number $sY = \sigma_y/P_1$
3. Compressive strength number $SC = \sigma_c/P_1$
4. The number $C_f \cdot P_1/\eta u$ combines the friction factor, the damping number $\rho V_1/\eta$ and the velocity number V_1/u as described in Chapter 4.
5. The number $zC_f/d_n\sqrt{R}$ combines the depth of cut number z/d_n, C_f and the jet geometry number $\sqrt{R}$.

The five nondimensional groups can be reduced to four groups only in two cases:

1. If the material has a constant ratio $r_s = \sigma_y/\sigma_c$, so that the two strength numbers are related by a constant coefficient, r_s. Investigation of the cutting behaviour of one material involves only X_N, sY, $z/d_n\sqrt{R}$ and $P_1/\eta u$. The friction coefficient is dropped since it has a constant value for one material.
2. For soft materials where $SC \leq 0.04$ and $X_N \leq 6$, the following simplified substitutions apply to Eqn. (4.16): $w = w_e$ and can be calculated from Eqn. (5.9), and P_a can be calculated from Eqn. (5.8). The resulting equation is

$$\frac{z\,C_f}{d_n\sqrt{R}} = 0.297\sqrt{\frac{X}{X_c}}\left[1 - 1.945\frac{\sigma_y}{P_1}\frac{X}{X_c}\right]\left[1 - e^{-0.58\frac{C_f P_1}{nu}\cdot\frac{X_c}{X}}\right] \quad (5.14)$$

Eqn. (5.14) can also be obtained directly from Eqn. (5.13) by substituting $\psi = 1$. The four nondimensional groups in this case are X_N, sY, $C_f P_1/nu$ and $zC_f/d_n\sqrt{R}$. A graphical representation of Eqns. (5.13) and (5.14) in Fig. 5.2, shows that at $X_N = 5$, there is a difference of 4% at SC = 0.02 and 93% at SC = 0.1. When SC = 0.04 and $X_N = 6$, the maximum difference between results of Eqns. (5.13) and (5.14) is about 10%. The simplified equation (5.14) can therefore be used when SC $\leq$ 0.04 and $X_N \leq 6$ within these limits of accuracy.

The effect of stand off distance on the depth of cut is shown graphically in Figs. 5.4 to 5.6. The range of values for the nondimensional numbers apply to typical cutting data for wood, coal, concrete, plastics and rocks. The number $C_f P_1/nu$ can vary from very small to very large values, while the other numbers are found in a much smaller range, for example:

$\frac{X}{X_c}$ varies from 1 to 10

$\frac{\sigma_y}{P_1}$ varies from 0.01 to 0.1

r_s has typical values of 2, 5 and 8.

The following conclusions are drawn for these typical values of the parameters:

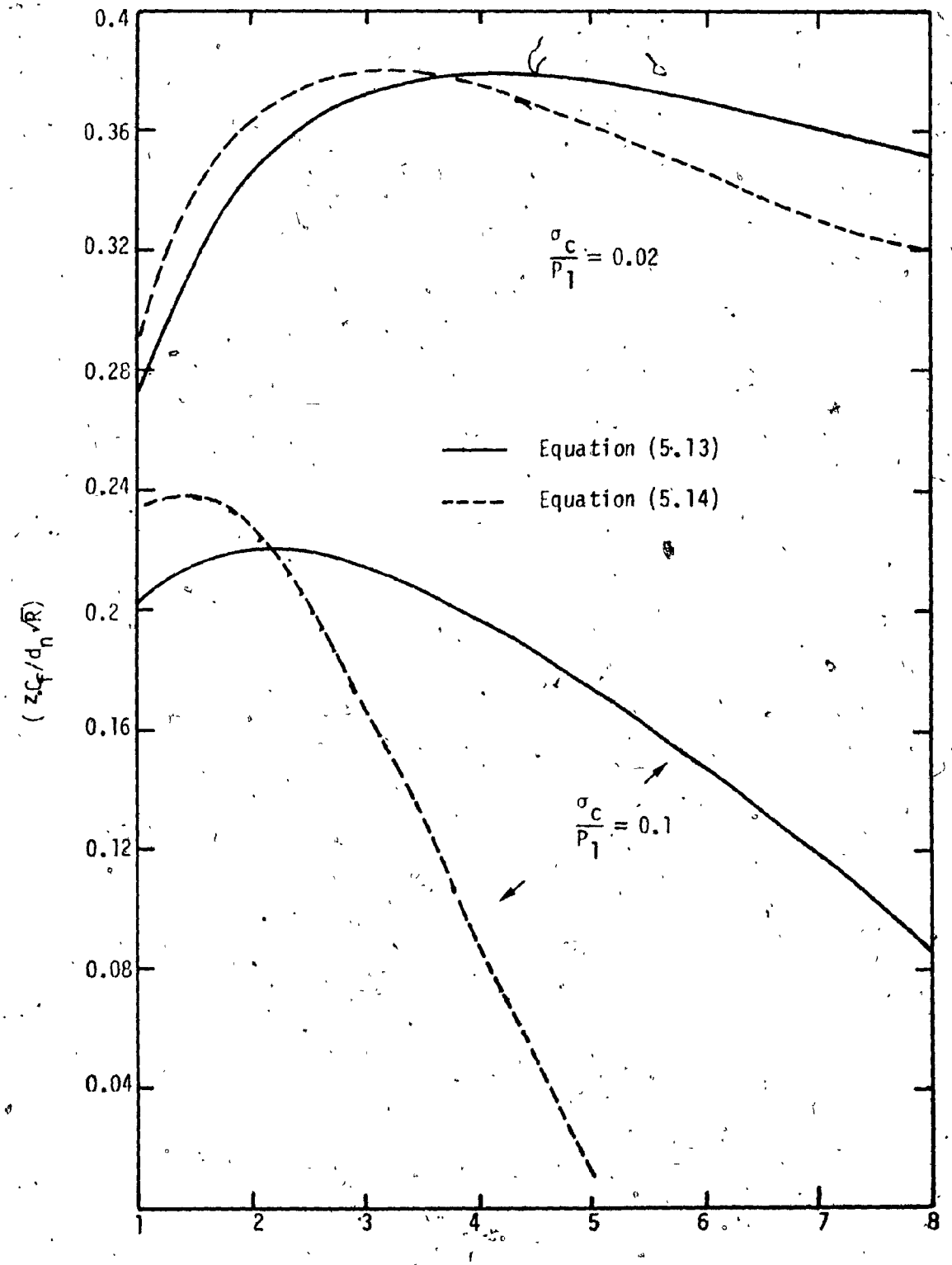

Fig. 5.3 Comparison of Results Obtained Using Equations (5.13), (5.14) in Predicting the Depth of Cut Under the Conditions $C_f P_1/nu = 0.8$, $r_s = 2$.

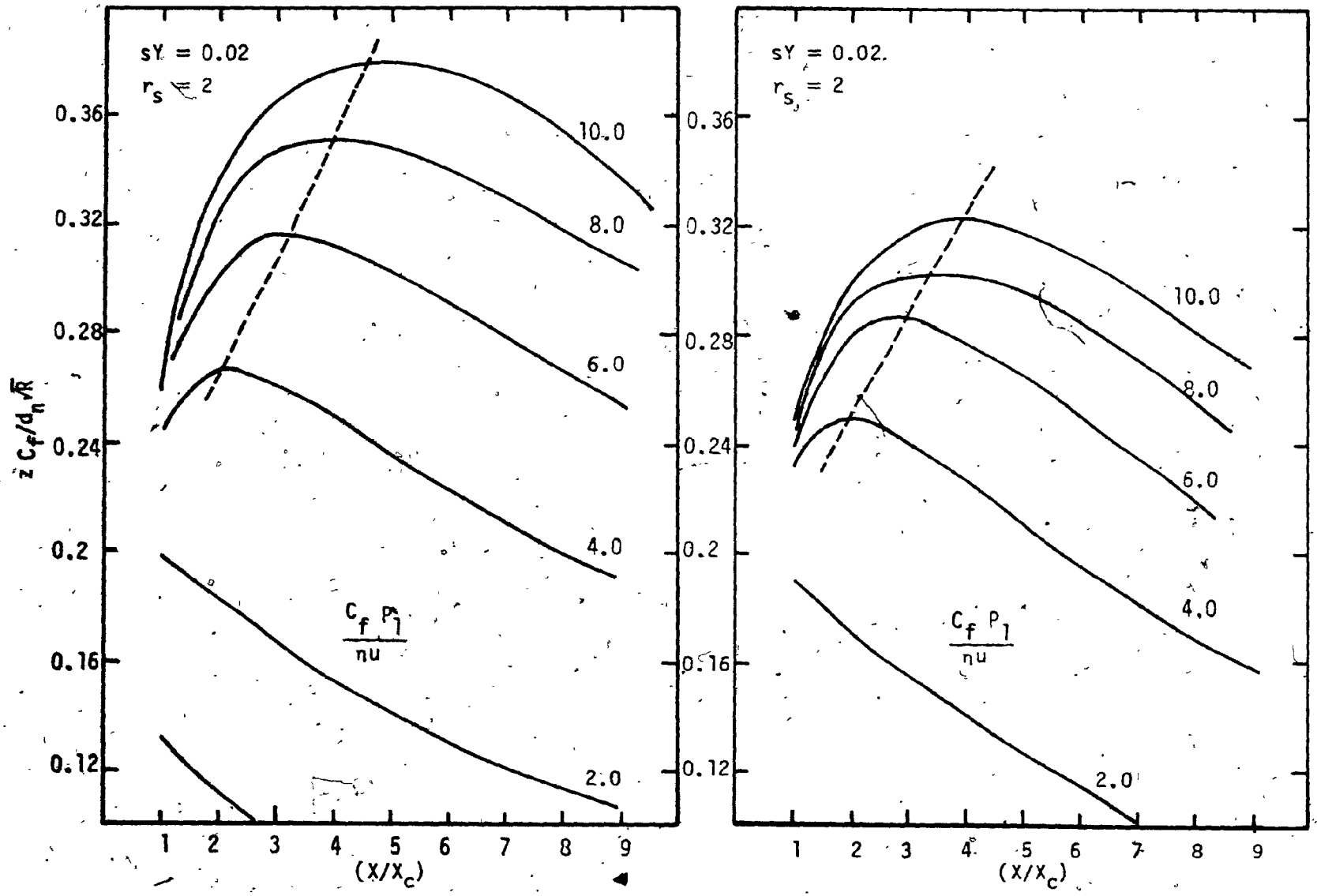

Fig. 5.4 Effect of Stand Off Distance Number (X/X_c) on the Nondimensional Depth of Cut Number ($z\,C_f/d_n\sqrt{R}$) at Different Values of ($C_f P_1/nu$), sY and r_s.

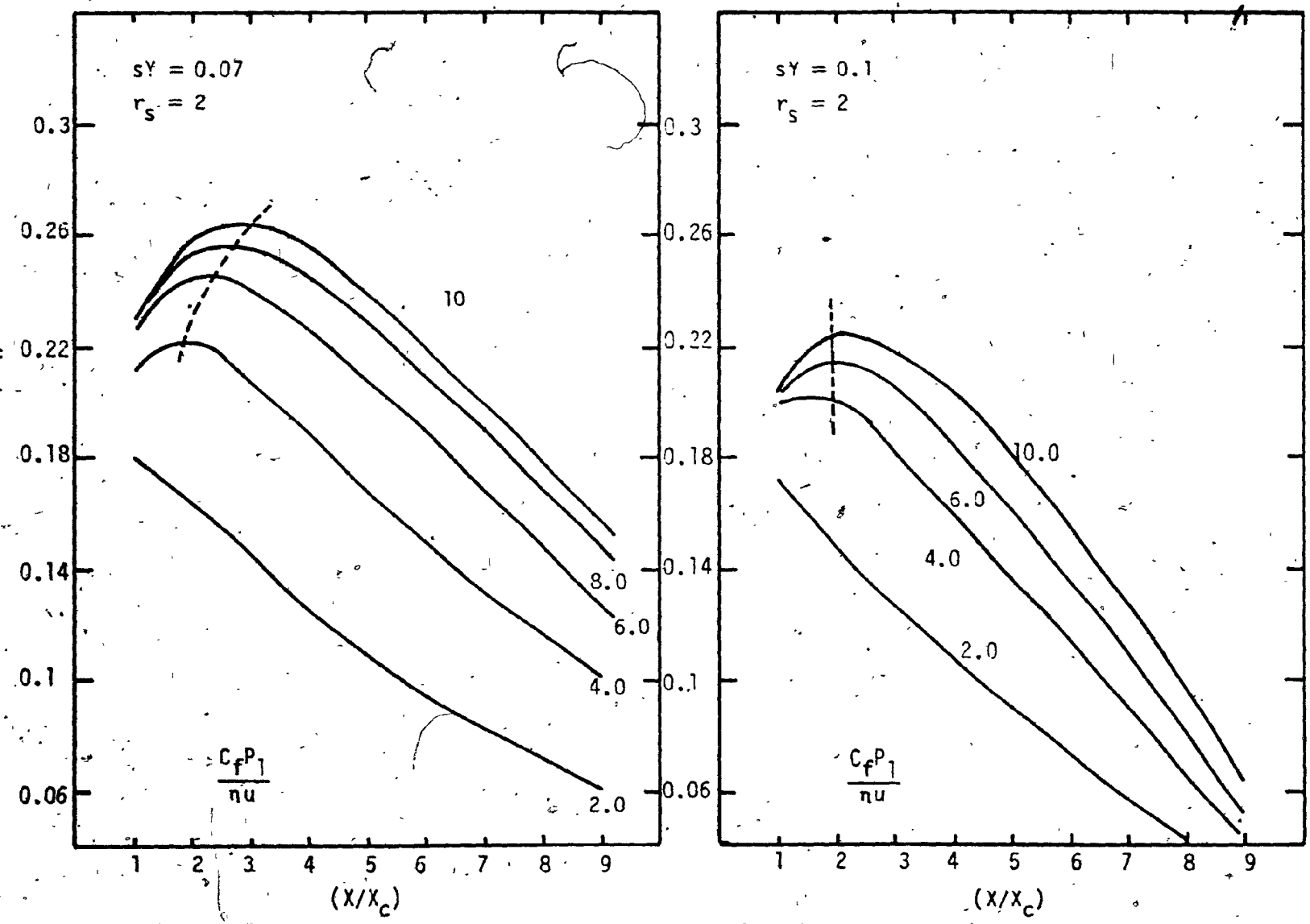

Fig. 5.5 Effect of Stand Off Distance Number (X/X_c) on the Nondimensional Depth of Cut Number $zC_f/d_n\sqrt{R}$ at Different Values of $(C_f P_1/nu)$, (sY) and (r_s).

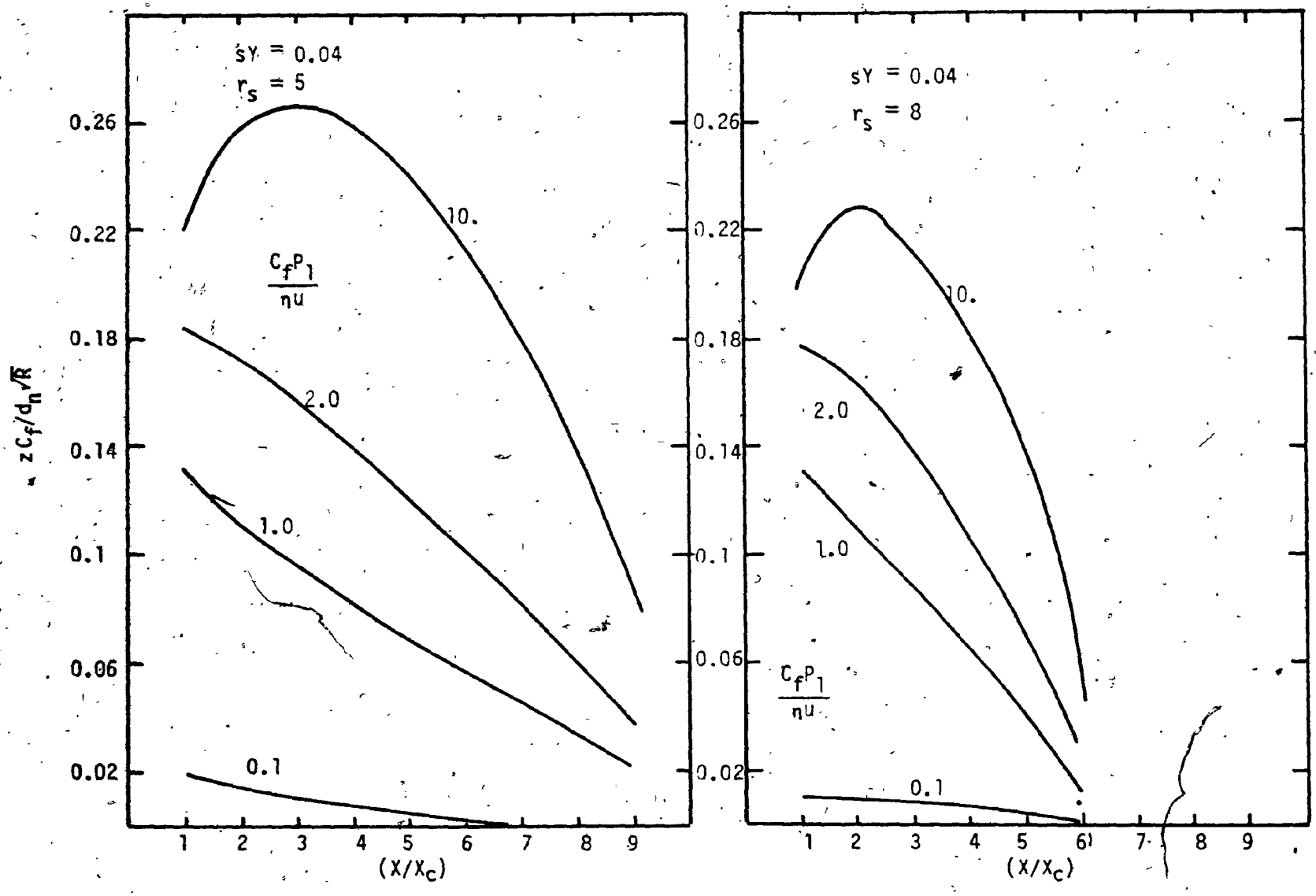

Fig. 5.6 Effect of Stand Off Distance Number (X/X_c) on the Nondimensional Depth of Cut Number $(z C_f/d_n\sqrt{R})$ at Different Values of $(C_f P_1/nu)$, (sY) and (r_s).

1. The optimum stand off distance generally occurs within the range $2 \leq X/X_c \leq 5$. Figs. 5.7 a, b show plots of the optimum stand off distance.

2. $C_f P_1/nu = 2$ is a lower critical value below which no optimum stand off distance exists and the depth of cut increases with decreasing distance from the nozzle. For values of $C_f P_1/nu > 2$ an optimum stand off distance exists and its exact location can be determined for specified values of $C_f P_1/nu$, sY and r_s.

3. $C_f P_1/nu = 10$ is a higher critical value. For $C_f P_1/nu > 10$, the depth of cut is a function of the strength numbers only, and it is independent of the value of $C_f P_1/nu$ as shown in Fig. 5.8. At this condition, reduction of the feed rate results in insignificant increases in the depth of cut. Fig. 5.9 is a schematic of the different regions of $C_f P_1/nu$.

Comparison with Experimental Results.

Eqn. (5.13) was used to predict the depth of cut at different stand off distances. The test conditions for wood listed in Table 2.16 and the wood properties of Table 4.2 were used. A typical value of R = 100 was used. The predictions are compared with the experimental results in Fig. 5.10. Values of $C_f P_1/nu$ for Poplar, Maple and Elm at the cutting conditions are 0.392, 0.288 and 0.205 respectively. These values are all below the lower critical value ($C_f P_1/nu = 2$) and consequently, an optimum stand off distance does not exist for $X/X_c > 1$ as discussed before. The data of Franz (26) suggests that aluminium

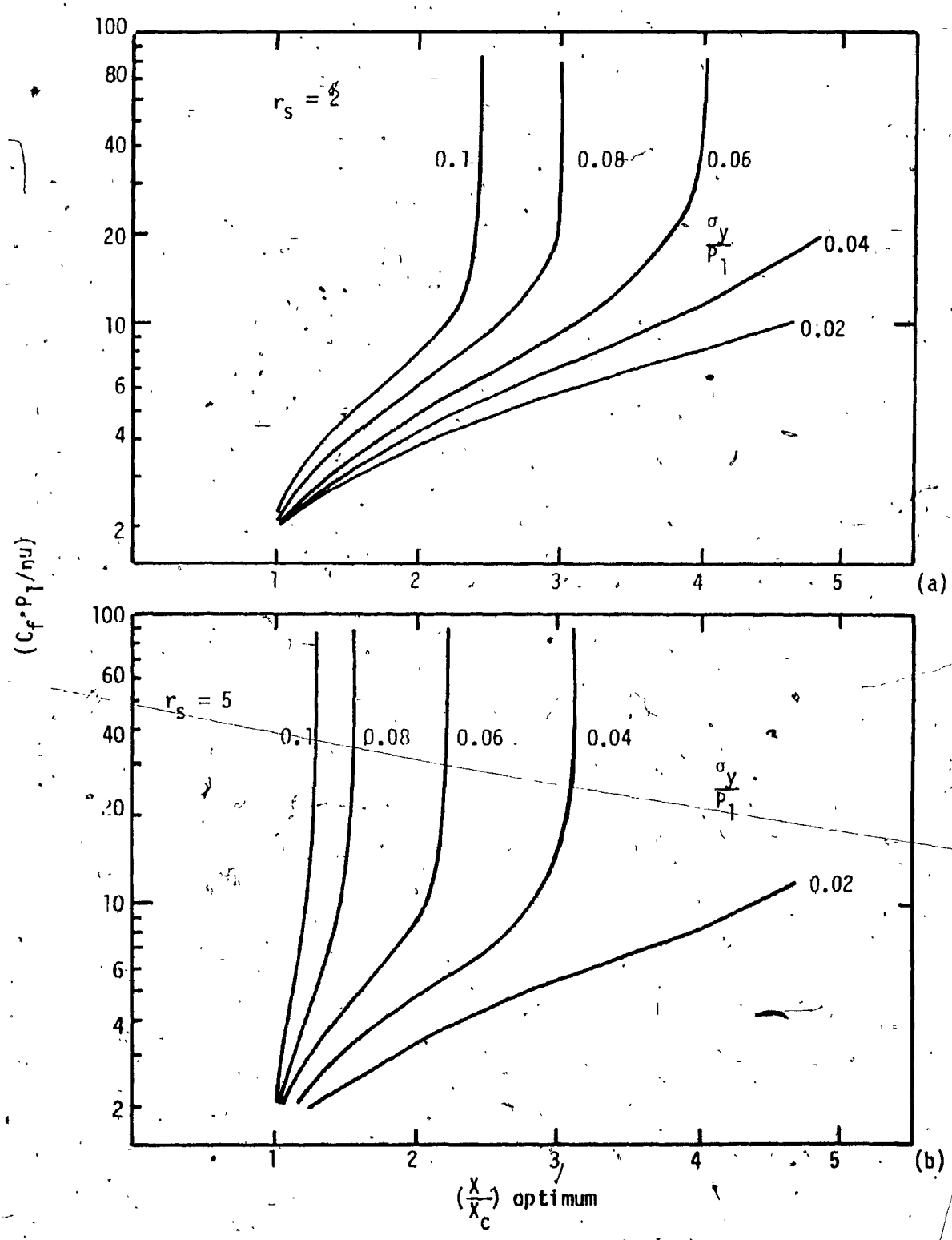

Fig. 5.7 Optimum Stand Off Distance Number for Maximum Depth of Cut at Different Values of $(C_f P_1/\eta u)$, (r_s) and (σ_y/P_1).

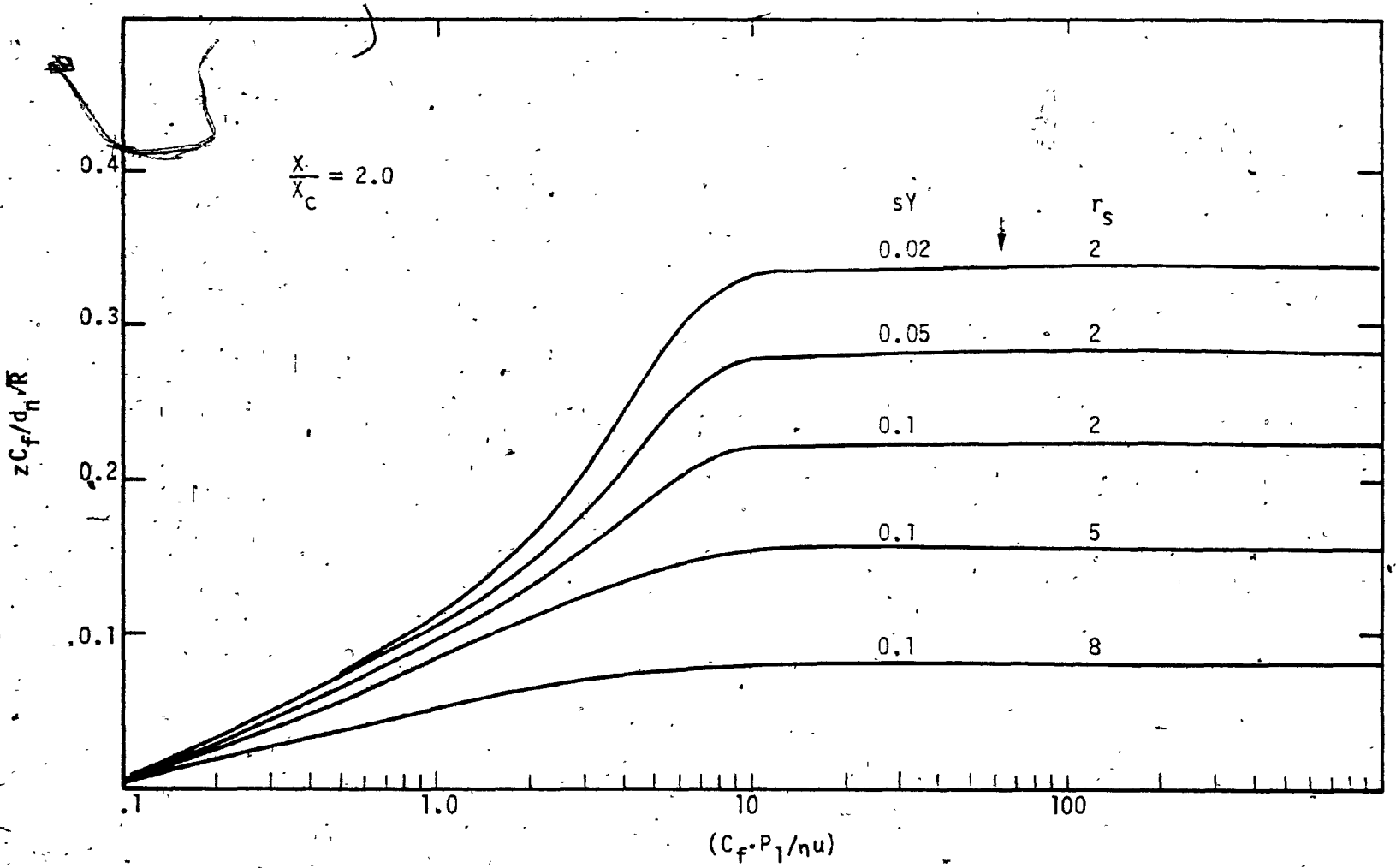

Fig. 5.8 Variation of Depth of Cut Number with Different Values of $(C_f P_1/nu)$, (r_s) and s_Y at Fixed Stand Off Distance Number.

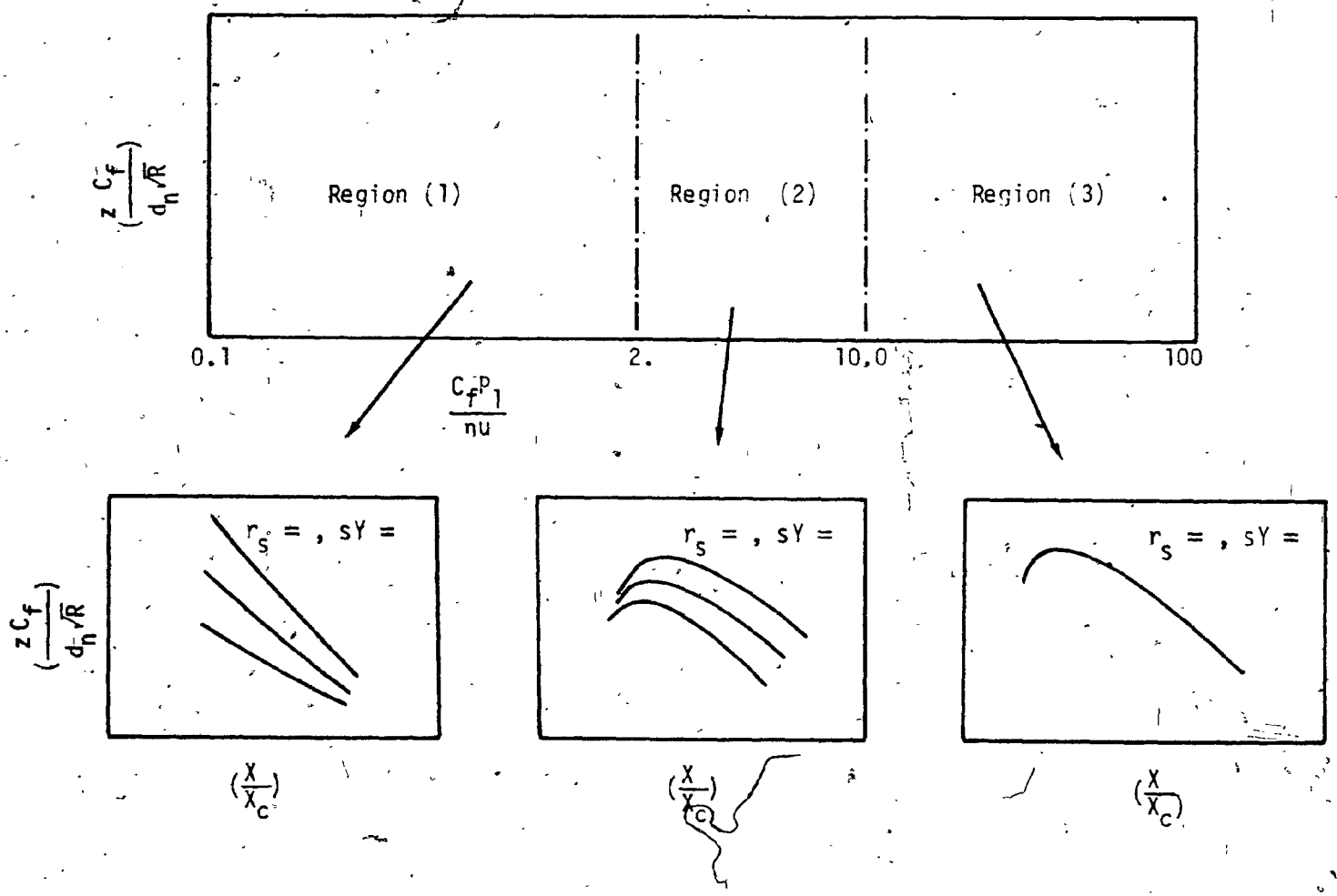

Fig. 5.9 Schematic Diagram of the Behaviour of the Nondimensional Depth of Cut with Stand Off Distance Number in the Different Regions of $(C_f P_1 / nu)$ Values.

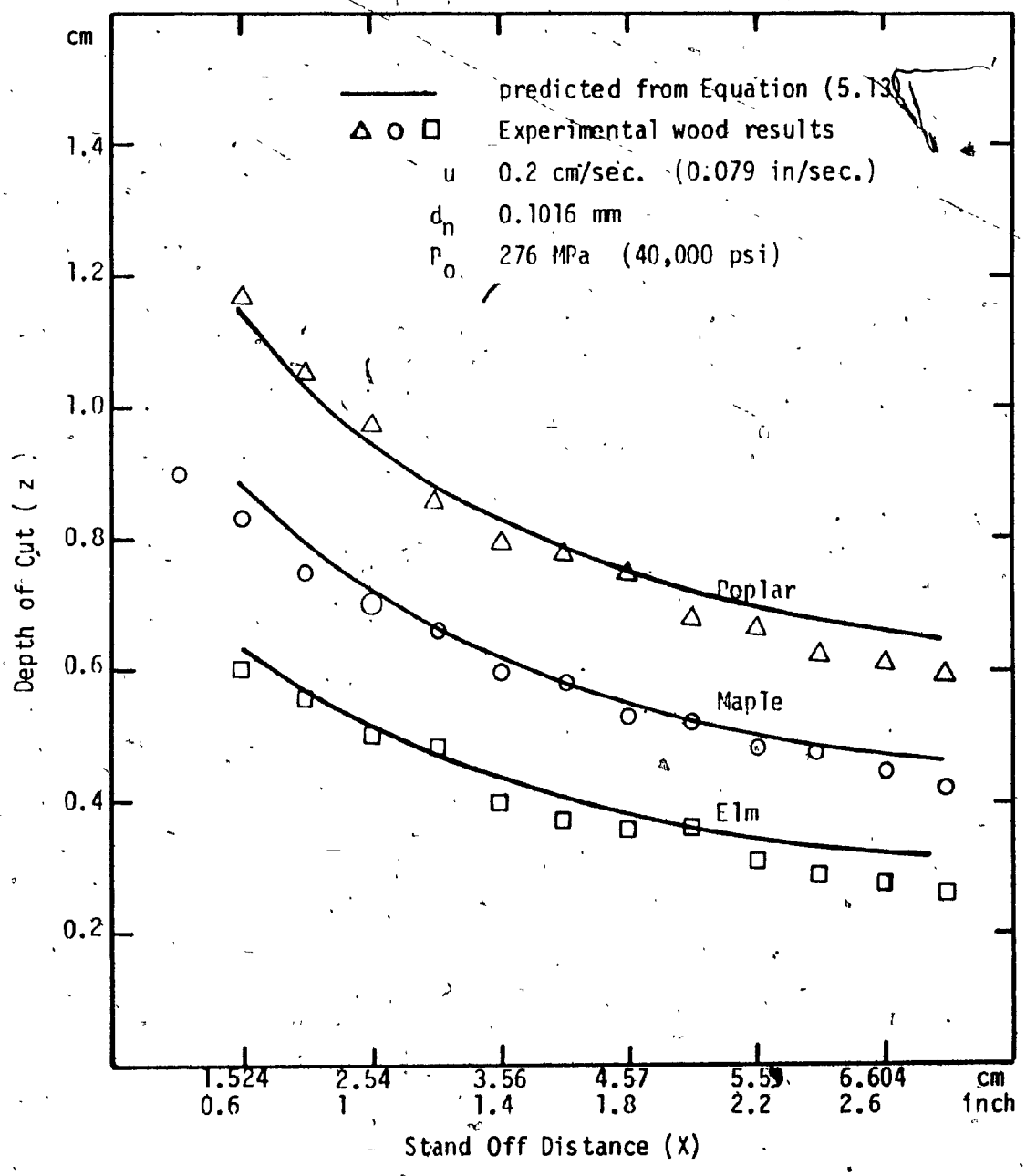

Fig. 5.10 Comparison of the Theoretical and Experimental Results of the Effect of Stand Off Distance on Depth of Cut of Wood.

cutting under the conditions given in Table 2.17 belongs to another mechanism of penetration. This aspect is discussed further in Section 6.2.1. Experimental confirmation of Eqn. (5.13) requires sufficient test data at different stand off distances for a wide variety of material to cover the practical range of values of the governing nondimensional groups. Such a detailed experimental program is beyond the scope of this study. However, indirect experimental confirmation of Eqn. (5.13) is obtained in the next section dealing with volume removal of material which incorporates the depth of cut equation.

5.4 THE EFFECT OF STAND OFF DISTANCE ON VOLUME REMOVAL

Achievement of maximum volume removal of material is important in mining and cleaning applications. The existance of an optimum stand off distance for maximum volume removal has been observed by many investigators (41), (43), (44), (45), (46) and (47) in cutting rocks and eroding metals with continuous and cavitating jets. In this section, a nondimensional equation for volume removal is derived. The equation should be useful in the design and choice of cutting parameters for an efficient volume removal system.

The volume per unit length along the cut is

$$\Delta V = z \cdot w_c \cdot 1 \qquad (5.15)$$

where w_c is the width of cut which is assumed to be uniform along the kerf and equal to the effective width of the jet at the start of

cutting. Substitution of the depth of cut from Eqn. (5.13) and the effective width w_e from Eqn. (5.10) in Eqn. (5.15), yields the non-dimensional equation:

$$\frac{\Delta V\, C_f}{R\, d_n^2} = 0.0994 \left(\frac{X}{X_c}\right) \cdot \psi^{4/3} \left(1 - \frac{\sigma y}{2P_1\phi}\right) \cdot \left(1 - e^{-2.256 \frac{C_f P_1}{nu} \phi}\right) \qquad (5.16)$$

where ϕ and ψ are defined in Eqn. (5.13). Eqn. (5.16) for volume removal contains the same four nondimensional groups X_N, sY, SC and $C_f P_1/nu$ that enter the depth of cut Equation (5.13). Reduction of these four groups to three can be done under the conditions mentioned in the previous section, namely $SC \leq 0.04$ and $X_N < 6$. The simplified equation is obtained by setting $\psi = 1$ which reduces Eqn. (5.16) to

$$\frac{\Delta V\, C_f}{R\, d_n^2} = 0.0994 \left(\frac{X}{X_c}\right) \left[1 - 1.945 \left(\frac{\sigma y}{P_1}\right)\left(\frac{X}{X_c}\right)\right] \left[1 - e^{-0.58 \frac{C_f P_1}{nu} \frac{X_c}{X}}\right] \qquad (5.17)$$

The same result is obtained if the local jet width rather than the effective jet width is used in Eqn. (5.15).

Graphical representation of Eqn. (5.16) in Figs. 5.11 and 5.12 for typical practical values of sY, strength ratio number r_s and $C_f P_1/nu$ confirm the existance of optimum stand off distances for maximum volume removal. Optimum stand off distance for a wide range of parameters are plotted separately in Fig. 5.13. This figure allows convenient selection of the optimum stand off distance for a particular application. Fig. 5.14 shows volume removal of material at a fixed stand off distance as a function of $C_f/P_1/nu$, SC and r_s. One curve

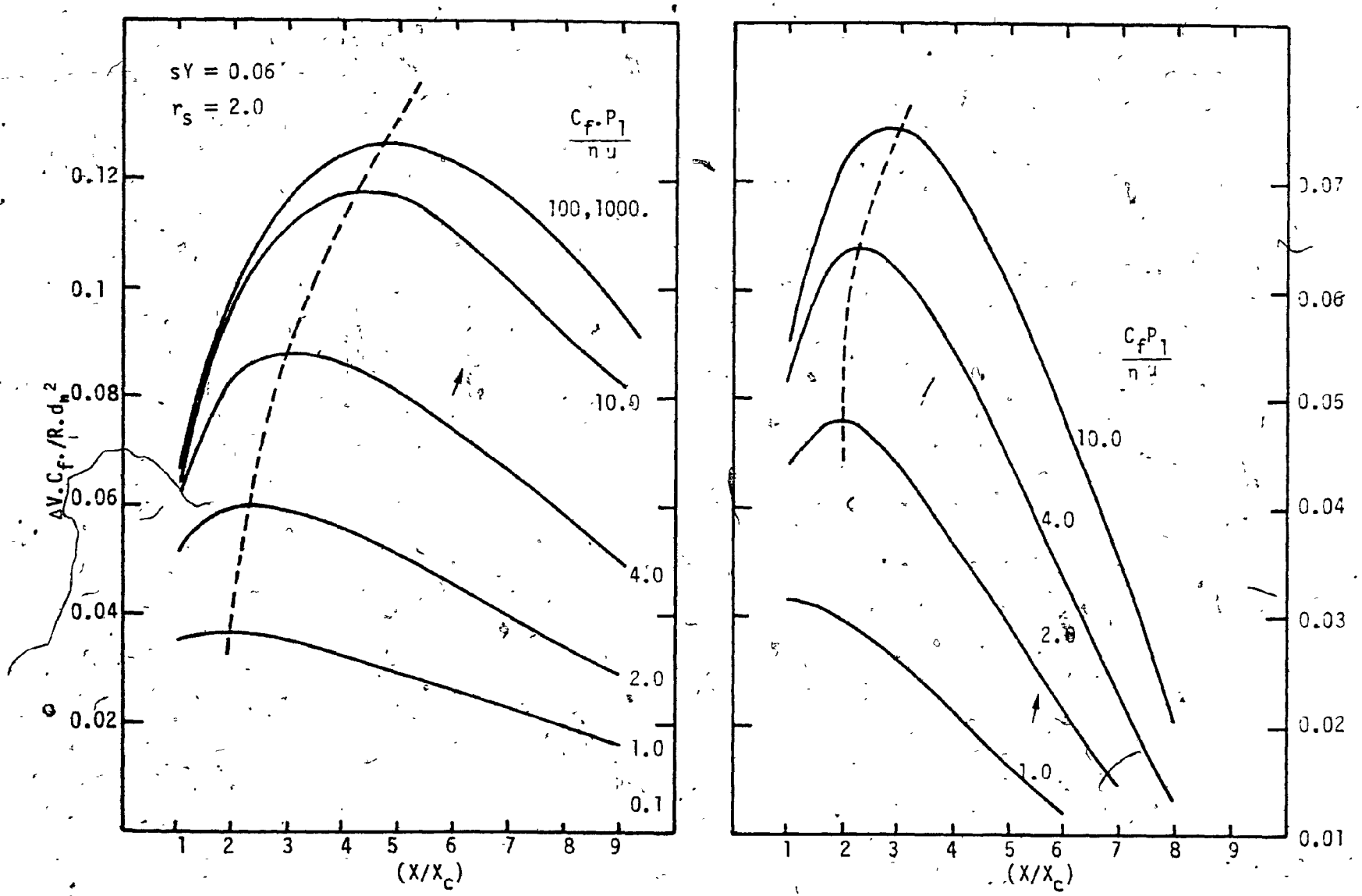

Fig. 5.11 Effect of the Stand Off Distance Number (X/X_C) on the Nondimensional Volume Removal Number at Different Values of $(C_f P_1/nu)$, r_s and sY.

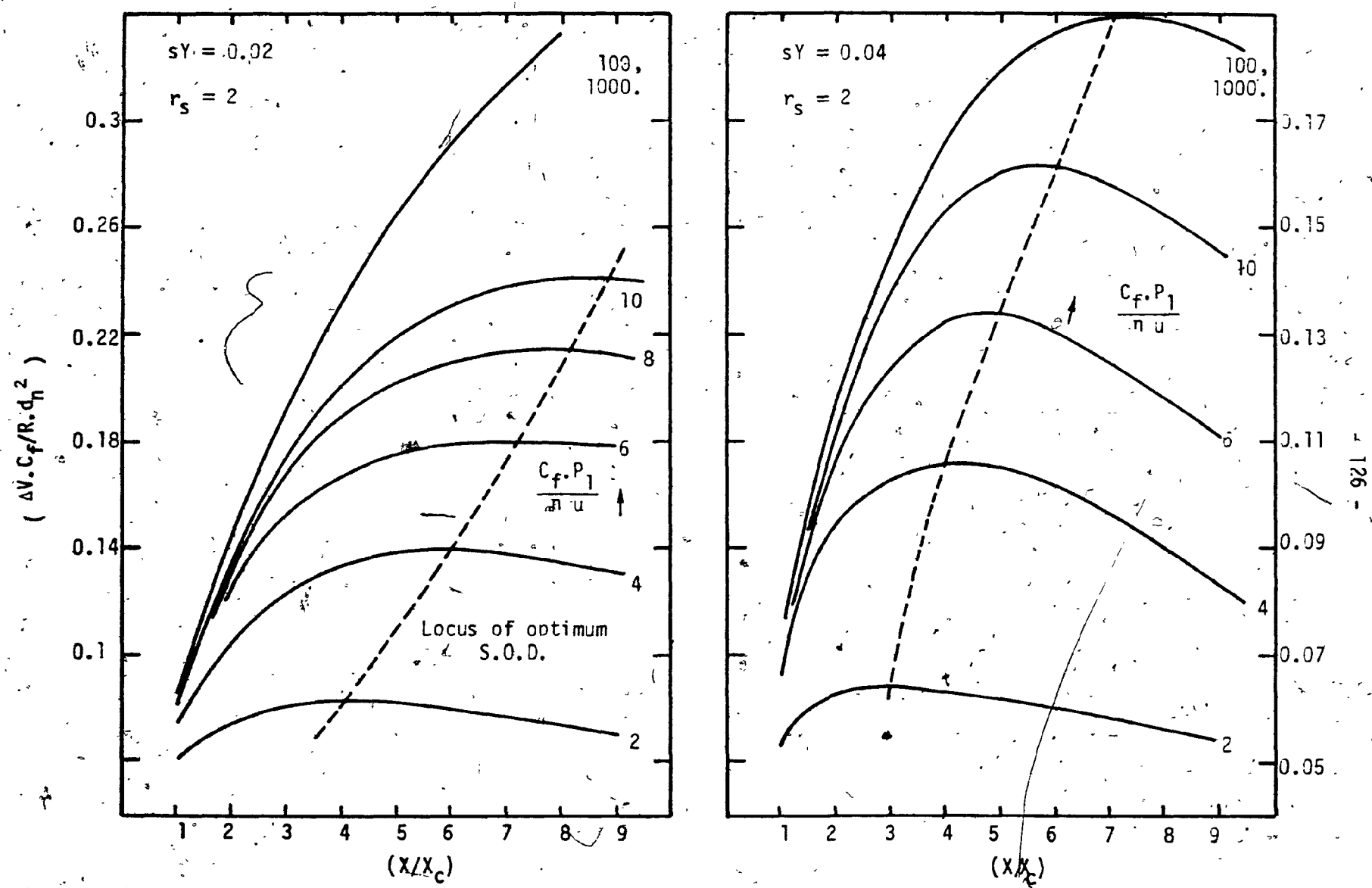

Fig. 5.12 Effect of Stand Off Distance Number (X/X_c) on the Nondimensional Volume Removal at Different Values of ($C_f P_1/\eta u$), sY and r_s.

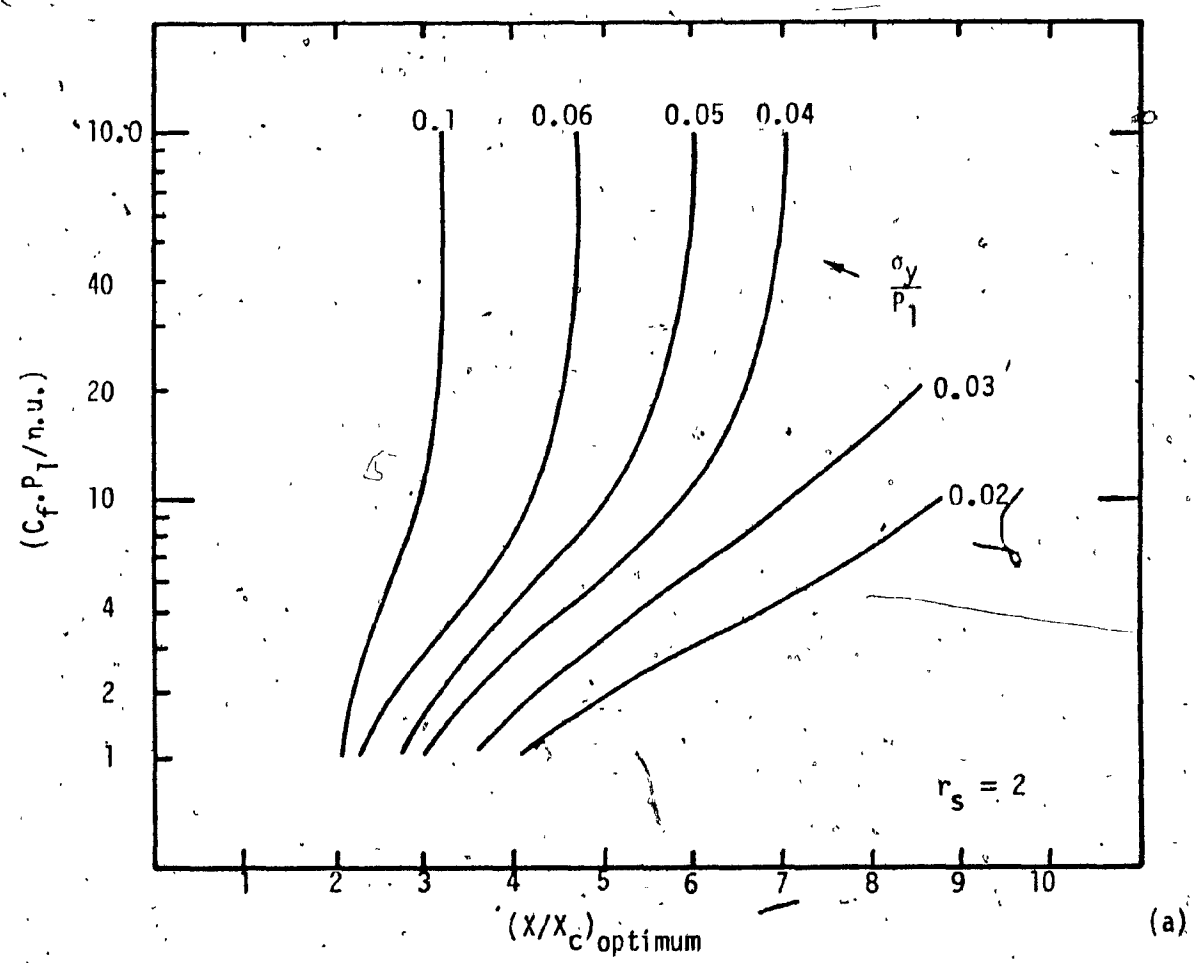

Fig. 5.13 Optimum Stand Off Distance Number (X/X_c) for Maximum Volume of Material Removal at Different Values of ($C_f P_1/nu$), sY and r_s.

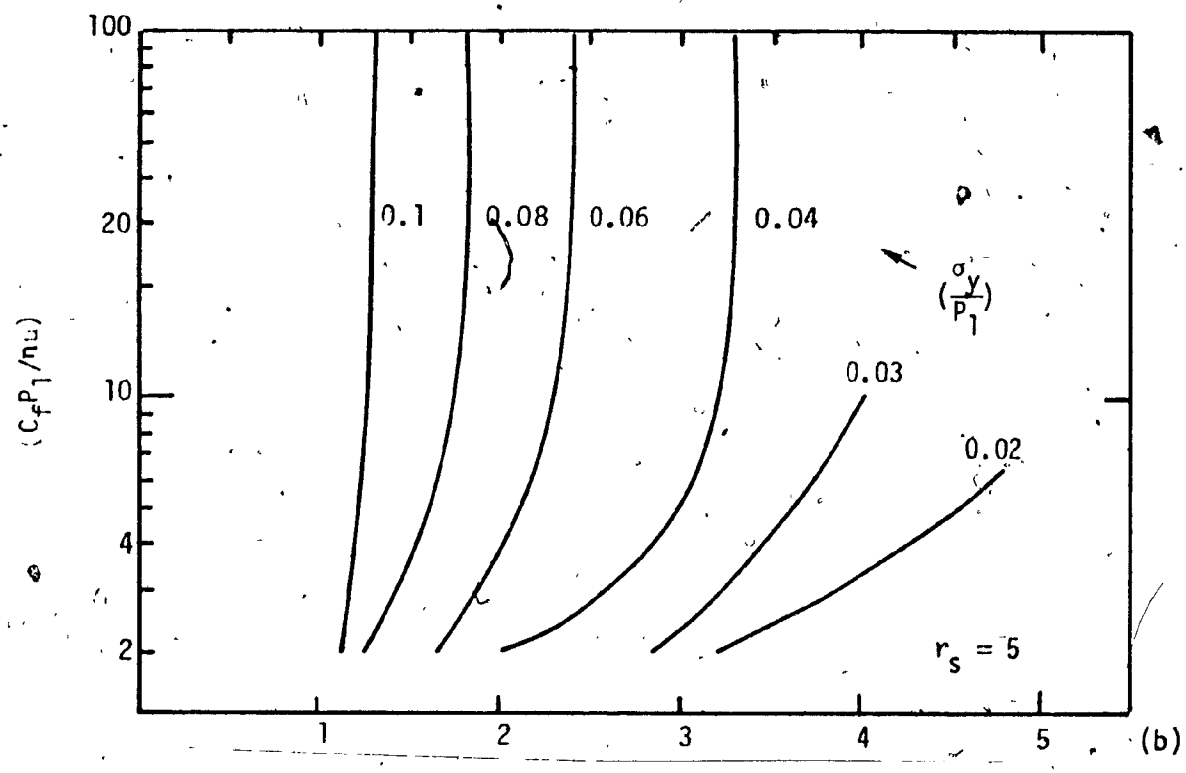

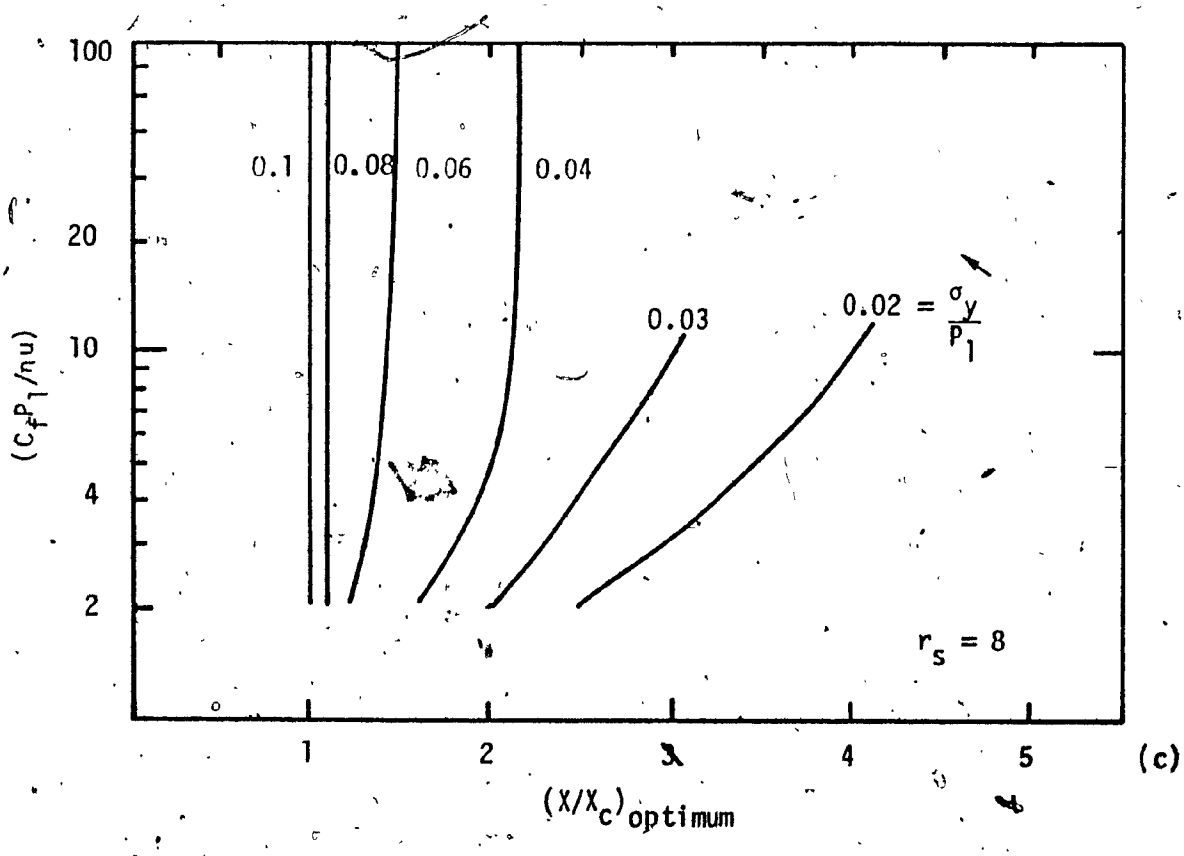

Fig. 5.13 Continued

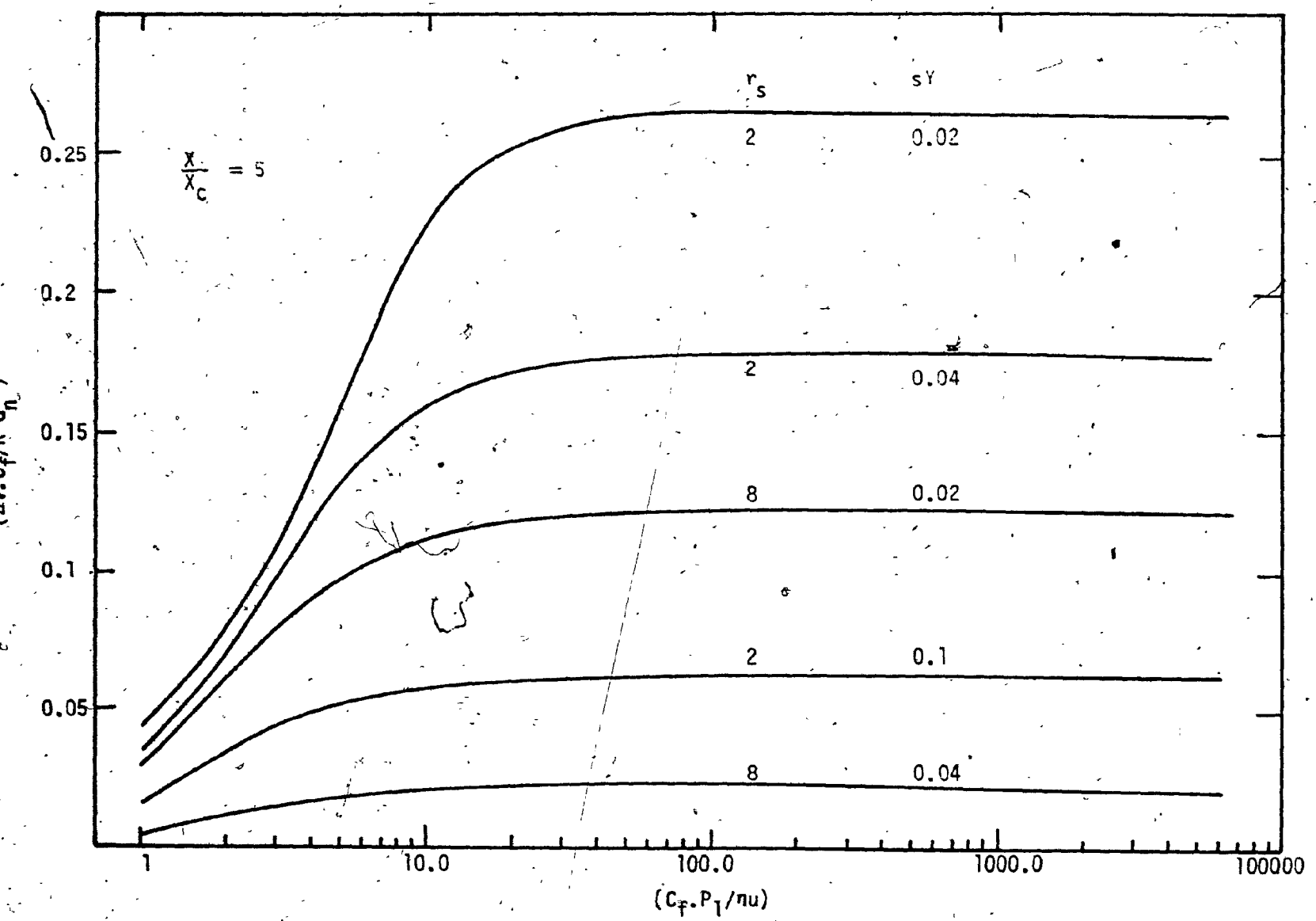

Fig. 5.14 Variation of the Volume Removal Number ($\Delta V.C_f/R\ d_n^2$) with Values of ($C_f P_1/nu$), sY and r_s at Constant Stand Off Distance Number.

represents the effect of feed rate on volume removal at fixed stand off distance. The value $C_f P_1/nu = 100$ represents a limiting value, after which, volume removal is a function of (sY) and (SC) only. The lower critical value of $C_f P_1/nu$ is 1.0. For values of $C_f P_1/nu \geq 1$, the existance of optimum stand off distance for maximum volume removal can be expected. Fig. 5.15 shows the different ranges of $C_f P_1/nu$ and the effect of stand off distance on volume removal.

Experimental Results

This section compares volume removal as predicted from Eqn. (5.16) with experimental results for wood (Table 2.20) and limestone (19). The widths of the top of the cut (w_1) and the bottom of the cut (w_2) were obtained with optical measuring scale. The volume calculated from the trapozoidal approximation is

$$\Delta V_{ex} = (w_1 + w_2)\, z / 2 \qquad (5.18)$$

Eqn. (5.16) was derived on the assumption that the width of cut equals the effective jet width (w_e). The theoretical model does not include secondary effects of jet spreading on initial impact and erosion by back flow. Both these effects result in widening the kerf in the top region. For materials such as wood there is a pronounced widening at the top of the kerf. The top width $w_1 \simeq 3w_e$ and the bottom width $w_2 \simeq w_e$. Hence the average width $(w_1 + w_2)/2 = 2w_e$, so that the predicted volume from Eqn. (5.16) must be multiplied by two or the experimental volume must be divided by two to obtain a comparison. That is

$$\Delta V_{ex} \simeq \frac{3w_e + w_e}{2}\, z \simeq 2w_e \cdot z \simeq 2\,\Delta V$$

or (5.19)

$$\Delta V_{mod.} \simeq \Delta V \text{ (Eqn. (5.17))} \quad (2)$$

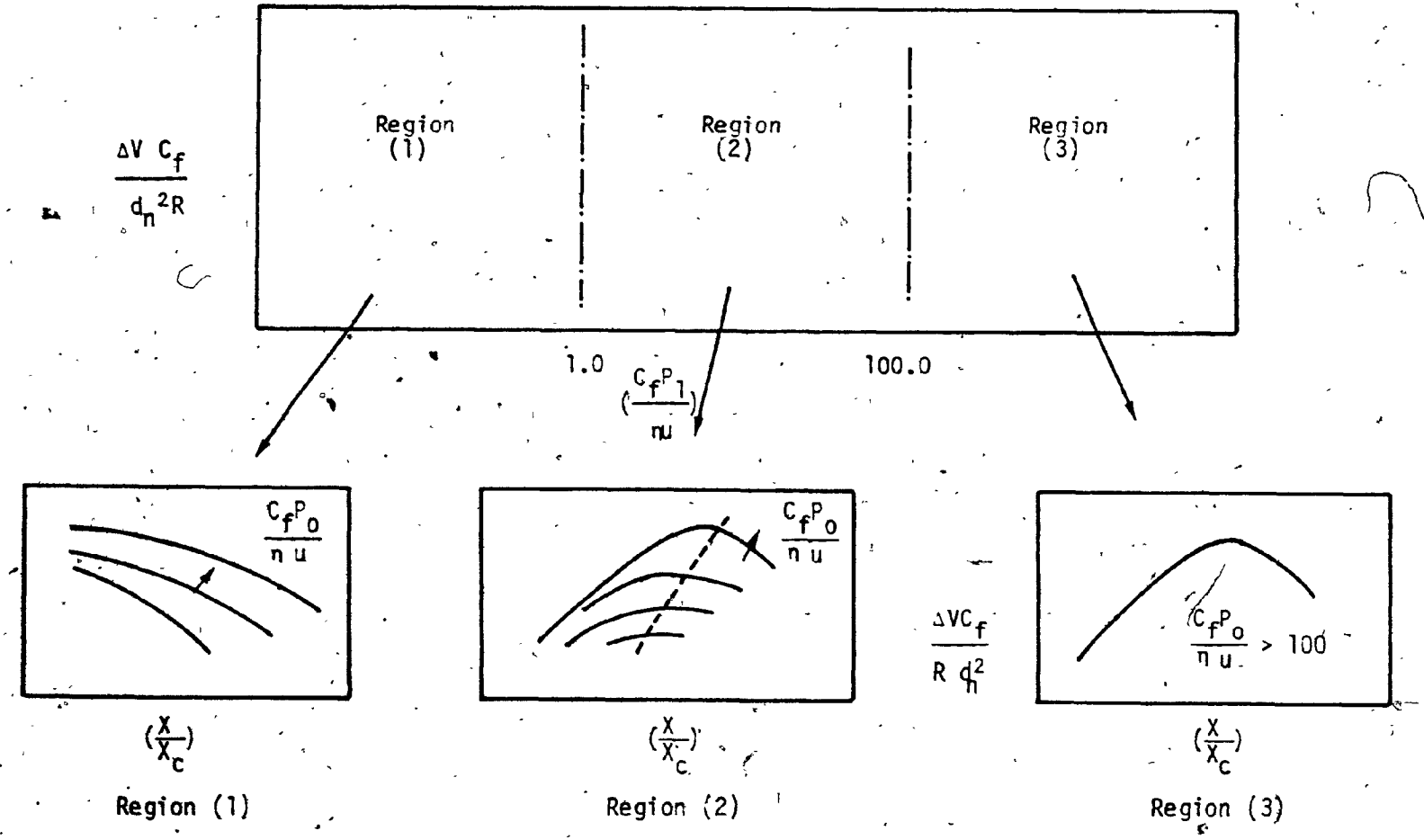

Fig. 5.15 Schematic Diagram of the Effect of Stand Off Distance Number on Volume Removal Number in the Different Regions of $(C_f P_1/\eta u)$ Values.

Comparison of experimental and modified theoretical results ($\Delta V_{mod.}$) in Fig. 5.16 shows that there is good agreement. Labus's (19) cutting results with limestone are compared with Eqn. (5.17) predictions. The following assumptions are made regarding stand off distance, jet structure and width of cut:

$$X/X_c = 1 , \qquad R = 100 , \qquad C_{D_o} = 0.8$$

$$w_c = \frac{w_1 + w_e}{2} , \qquad w_e = d_n = 0.05 \text{ cm}$$

The value w_c was used instead of w_e in Eqn. (5.15), so that

$$\Delta V_{mod.} = \Delta V \text{ (Eqn. (5.17))} \left[\frac{w_1 + w_e}{2w_e}\right] \qquad (5.20)$$

Comparison of experimental and theoretical values of $\Delta V_{mod.}$ in Table 5.4 show that there is good agreement.

sY	w_1 cm	Removed Volume ΔV cc	
		Experimental	Eqn. (5.20)
0.0043	0.317	0.104	0.109
0.0045	0.317	0.114	0.104
0.0053	0.396	0.123	0.11
0.0069	0.317	0.076	0.071
0.0067	0.317	0.066	0.074
0.004	0.396	0.132	0.141
0.0047	0.317	0.132	0.1

Table 5.4 Comparison of Experimental and Theoretical Results for Limestone (19), Volume Removal.

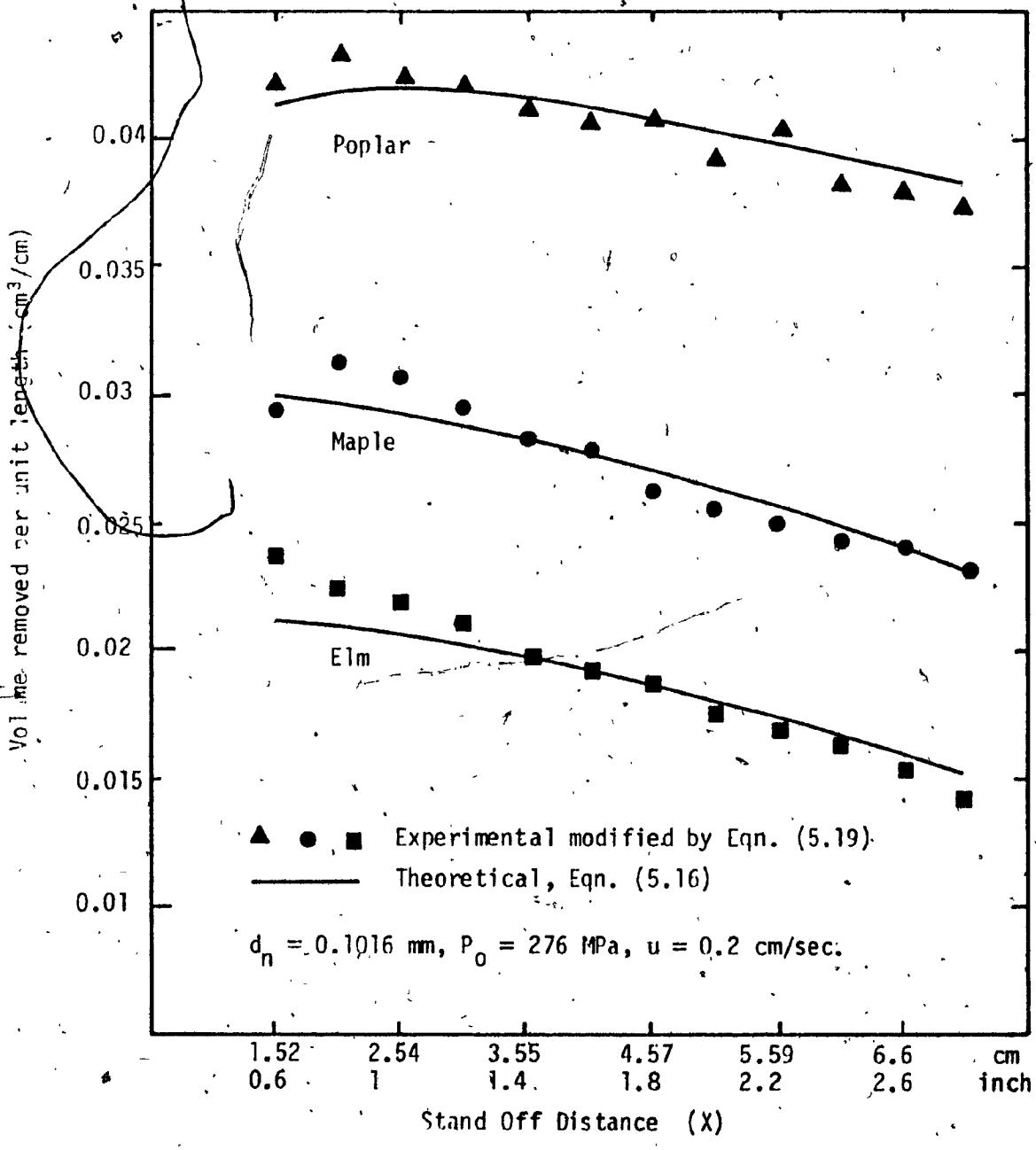

Fig. 5.16 Comparison of Experimental and Theoretical Results of the Effect of Stand Off Distance on Volume Removal of Wood.

Comparison with other published experimental results could not be made because of insufficient information on material properties and on the depth and width of cuts. The results of volume removal with wood and limestone are further used to calculate the specific energy values in the next section.

5.5 THE CUTTING EFFICIENCY AND OPTIMUM CONDITIONS

The cutting efficiency η_c is defined as the ratio of the volume removal to the input energy. The specific energy (SE)is the inverse of the cutting efficiency and it is an important parameter in mining applications where economic application requires minimization of specific energy values. The cutting efficiency in many applications (such as mining) is defined by

$$\eta_c = \frac{\Delta V}{\frac{1}{2} \dot{m} V_1^2 t} \tag{5.21}$$

where t is the time required to remove ΔV of the material. For unit length along the cut, the volume removed is given by Eqn. (5.16) and the corresponding time will be $t = 1/u$. Substitution from Eqn. (5.16) into Eqn. (5.21) and setting $t = 1/u$ results in the nondimensional equation

$$\frac{\eta_c \cdot V_1 \cdot n}{R} = 0.1256 \left(\frac{X}{X_c}\right) \frac{\psi^{4/3}}{\left(\frac{C_f P_1}{nu}\right)} \left[1 - \frac{\sigma_y}{2P_1\phi}\right] \left[1 - e^{-2.256 \frac{C_f P_1}{nu} \phi}\right] \tag{5.22}$$

where ϕ and ψ are defined in Eqn. (5.13). The specifc energy equation is obtained from Eqn. (5.22) by substituting $\eta_c = \frac{1}{SE}$.

$$\frac{SE \cdot R}{\eta \cdot V_1} = 7.96 \frac{(C_f P_1 / \eta u)}{(\frac{X}{X_c})\, \psi^{4/3}\, (1 - \frac{\sigma_y}{2P_1 \phi})(1 - e^{-2.256\,(C_f P_1 / \eta u)\phi})} \qquad (5.23)$$

For cutting of certain materials under fixed nozzle parameters (P_o, d_n), the highest cutting efficiency requires knowing the optimum stand off distance for maximum volume removal and the optimum feed rate. The optimum stand off distance can be found from conditions of maximum volume removal as discussed in Section 5.4. The effect of feed rate is shown in Fig. 5.17. For values of $\eta u / C_f P_1 > 10$ (Fig. 5.17), the efficiency reaches a maximum value. In practical terms, this means for instance, that high frequency oscillating jets ($\eta u / C_f P_1 > 10$) operate in a high efficiency region where lower energy input at high feed rates dominates reduced volume removal. For cleaning and descaling applications, oscillating jets will be efficient since small amounts of volume need to be removed at low specific energy values. The required conditions for efficient volume removal of material are to adjust the feed rate so that $\eta u / C_f P_1 > 10$ and to select the optimum stand off distance for maximum volume removal from Fig. 5.13.

Comparison of Specific Energy Predictions with Experimental Results.

Specific energy values for wood and limestone obtained from the experimental data listed in Tables 2.21 and 2.22 are compared with predicted values calculated from the modified equation

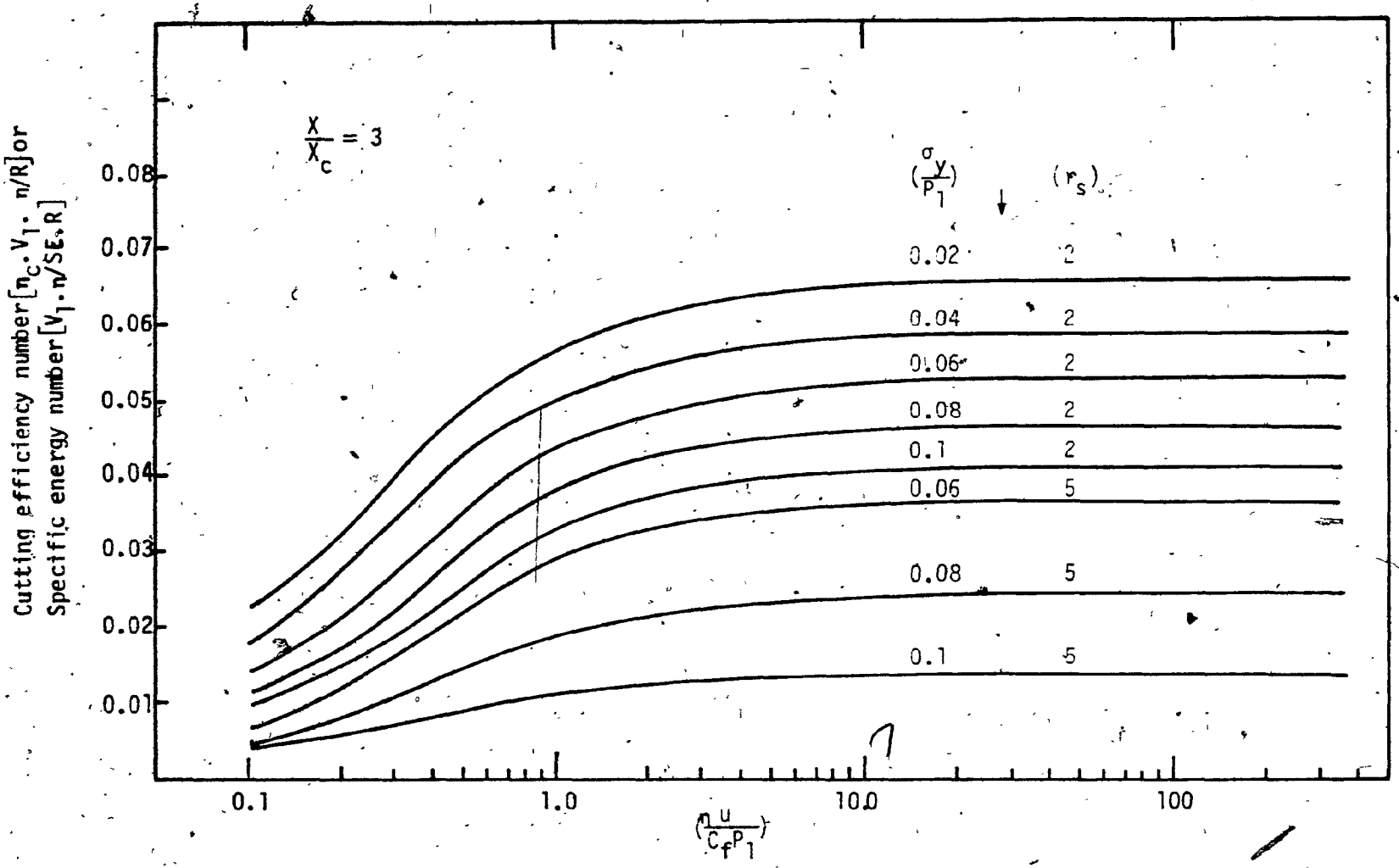

Fig. 5.17 The Specific Energy Number (or Cutting Efficiency Number) as a Function of $(\eta u/C_f P_1)$, r_s and σ_y at Fixed Stand Off Distance.

$$SE(\text{modified}) = SE(\text{Eqn. (5.23)}) \; / \; \left(\frac{w_1 + w_e}{2\, w_e}\right) \qquad (5.24)$$

which includes the appropriate widening factor $(w_1 + w_e/2w_e)$. Table 5.5 lists the experimental and theoretical specific energy values for wood. Inspite of the accumulated errors from widths of cut and depth of cut measurements, experimental and theoretical values deviate by less than 18%. Comparison of the nondimensional results with limestone in Table 5.6 also shows good agreement between theory and experiments. The widening factor as given by $(w_1 + d_n/2dn)$ was used.

u in/sec.	Poplar		Maple		Elm	
	Exp.	Eqn. (5.24)	Exp.	Eqn. (5.24)	Exp.	Eqn. (5.24)
0.08	93554	97263	127948	137204	171359	192547
0.16	93407	93553	123759	132859	161175	188096
0.32	92274	91734	123759	130721	159935	185497
0.64	94683	90833	118134	129661	173669	184803
1.28	83299	90384	119127	129133	151102	184258
2.56	83299	90161	111066	12889	148908	183986

Table 5.5 Experimental and Theoretical Specific Energy Values in J/cc for Wood.

$\frac{\sigma_y}{P_o}$	$n_c.V_1.n/R = V_1 n/SE.R$	
	Experimental	Eqn. (5.24)
0.0043	0.022	0.225
0.0045	0.251	0.226
0.0053	0.325	0.289
0.0009	0.256	0.238
0.0067	0.217	0.237
0.004	0.26	0.264
0.00476	0.285	0.228

Table 5.6 Experimental and Theoretical Values of the Cutting Efficiency Number for Limestone (19).

5.6 MULTIPASS CUTTING AND DEPTH OF CUT

Multipass cutting at high feed rates may result in deeper overall cuts than single pass cutting carried out over the same total elapsed time. Observation of tests with wood indicates the existance of optimum feed rates and number of passes.

If the initial stand off distance is X_1 and the depth of cut after the i^{th} pass is z_i, then the stand off distance after n passes is X_{n+1}

$$X_{n+1} = X_1 + \sum_{i=1}^{i=n} z_i \qquad (5.25)$$

This equation can be nondimensionalized by dividing by X_c

$$\left(\frac{X}{X_c}\right)_{n+1} = \left(\frac{X}{X_c}\right)_1 + \sum_{i=1}^{i=n} \left(\frac{z}{X_c}\right)_i \qquad (5.26)$$

The depth of cut equation (5.13) can be rewritten in the form

$$\frac{z}{X_c} = \frac{0.297}{C_f \sqrt{R}} \sqrt{\frac{X}{X_c}}\ \psi^{2/3}\left(1 - \frac{\sigma_y}{2P_1\phi}\right)\left(1 - e^{-2.256(C_f P_1/nu)\phi}\right) \qquad (5.27)$$

where ϕ, ψ are defined in Eqn. (5.13). Substituting Eqn. (5.27) in Eqn. (5.26) results in

$$\left(\frac{X}{X_c}\right)_{n+1} = \left(\frac{X_1}{X_c}\right)_1 + \sum_{i=1}^{i=n} \frac{0.297}{C_f \sqrt{R}} \sqrt{\left(\frac{X}{X_c}\right)_i}\ \psi_i^{2/3}\left(1 - \frac{\sigma_y}{2P_1\phi_i}\right)$$

$$\left(1 - e^{-2.256\ (C_f P_1/nu)\phi_i}\right) \qquad (5.28)$$

where

$$\psi_i = 1 - \sqrt{\frac{\sigma_c}{2P_1}\left(\frac{X}{X_c}\right)_i}$$

$$\phi_i = \frac{2}{(X/X_c)_i}\left(0.5 - 0.57\ \psi_i + 0.2\ \psi_i^2\right)$$

The cummulative depth of cut after n passes z_a is given by

$$\frac{z_a}{X_c} = \left(\frac{X}{X_c}\right)_{n+1} - \left(\frac{X}{X_c}\right)_1 \qquad (5.29)$$

If the initial standoff distance is less than X_c, then Eqn. (4.16) can be used instead of Eqn. (5.13) in calculating the depth of cut since the velocity can be assumed uniform across the jet in the initial region. However, the most convenient nondimensional form of Eqn. (4.16) is

$$\frac{z}{X_c} = \frac{0.886}{C_f R}\left[1 - 0.5\ \frac{\sigma_y}{P_1}\right]\left[1 - e^{-2.256\ (C_f P_1/nu)}\right] \qquad (5.30)$$

Experimental Results

A computer program was written for the recurrence relationship of Eqn. (5.29). Eqns. (5.27) and (5.30) are used to predict the cumulative depth of cut (z_a) when X is larger or less than X_c respectively. Experimental and theoretical results with wood are compared in Figs. 5.18 to 5.20. Good agreement is obtained for a low number of passes but accumulation of errors increase the deviation at a high number of passes. The major error results from the fact that no allowance is made for differences in successive cuts caused by narrowing of the cut, jet spreading and increased friction in narrower cuts. The feed rates shown in Figs. 5.18 to 5.20 have been choosen such that the ratio between two consecutive feed rates is 2. The dotted lines in these figures show the depth of cut that would have been obtained at the same total elapsed time as single pass cutting. This condition (same elapsed time) can be characterized by the ratio $\frac{u}{N}$ (cm/sec. pass) which is a constant value for each of these dotted lines. The positive slopes of the dotted lines clearly show the improved cutting which results from multipass cutting rather than single pass cutting. The slopes of these lines ($\frac{u}{N}$ = constant) increase when R increases and sY decreases as shown in Fig. 5.21 for the expected results with Poplar when R = 160. An increase of 73% in depth of cut with Poplar (when R = 160) is obtained with four passes and 3.96 cm/sec. feed rate over that obtained at one pass and 0.99 cm/sec. feed rate. Both conditions have the same elapsed cutting time ($\frac{u}{N}$ = 0.99 cm/sec. pass).

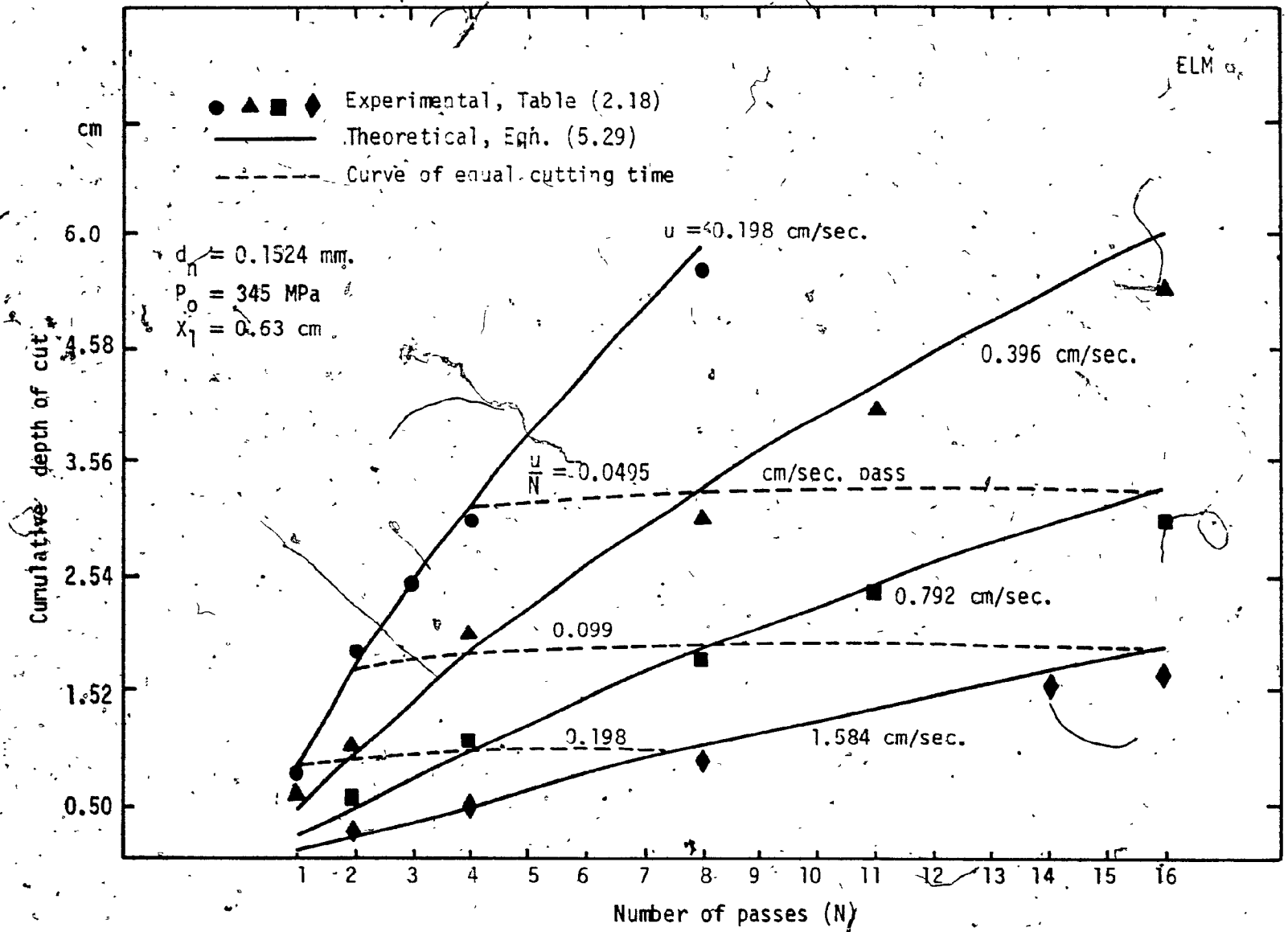

Fig. 5.18 Theoretical and Experimental Results of Multipass Cutting of Elm.

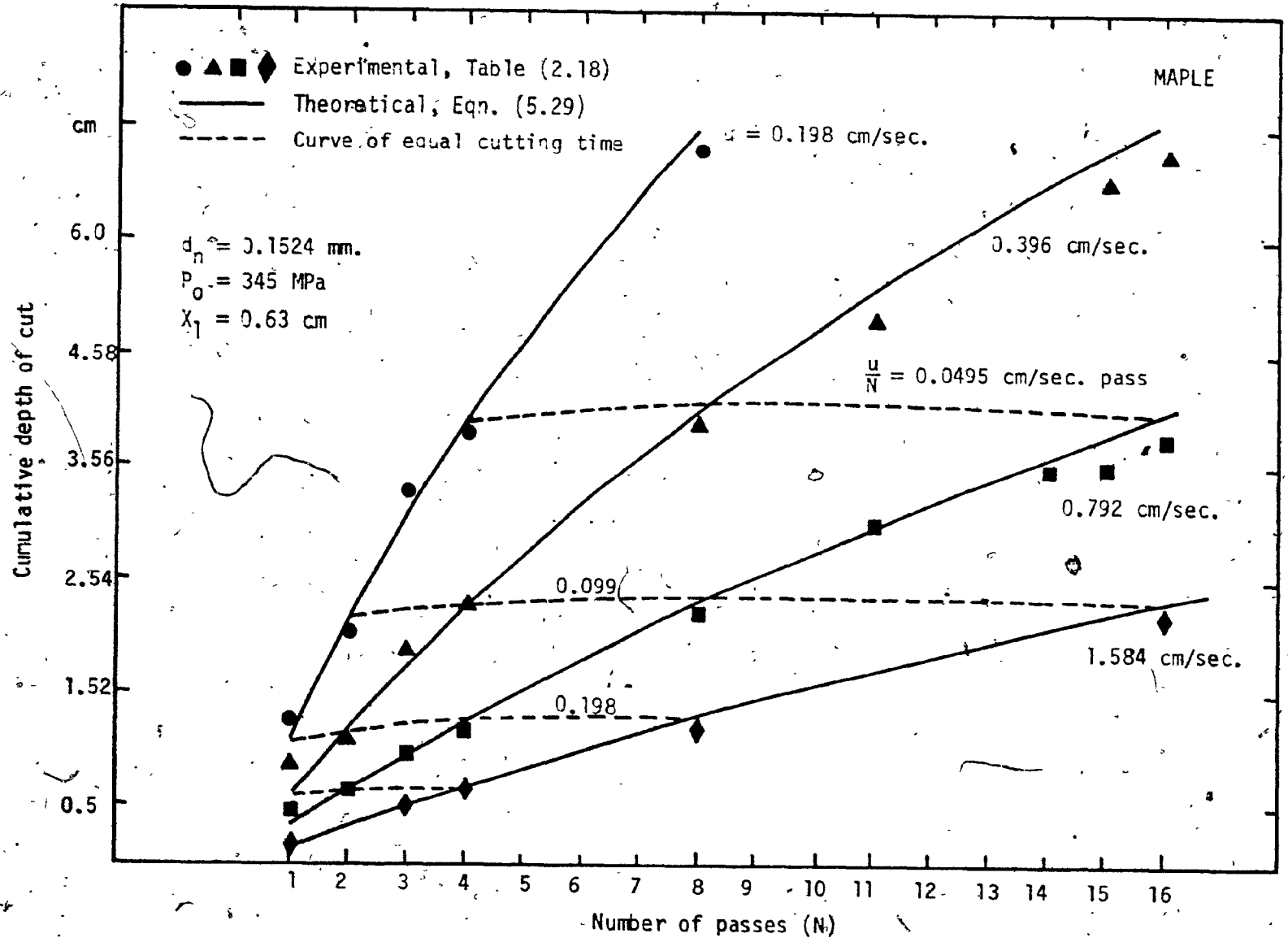

Fig. 5.19 Theoretical and Experimental Results of Multipass Cutting of Maple.

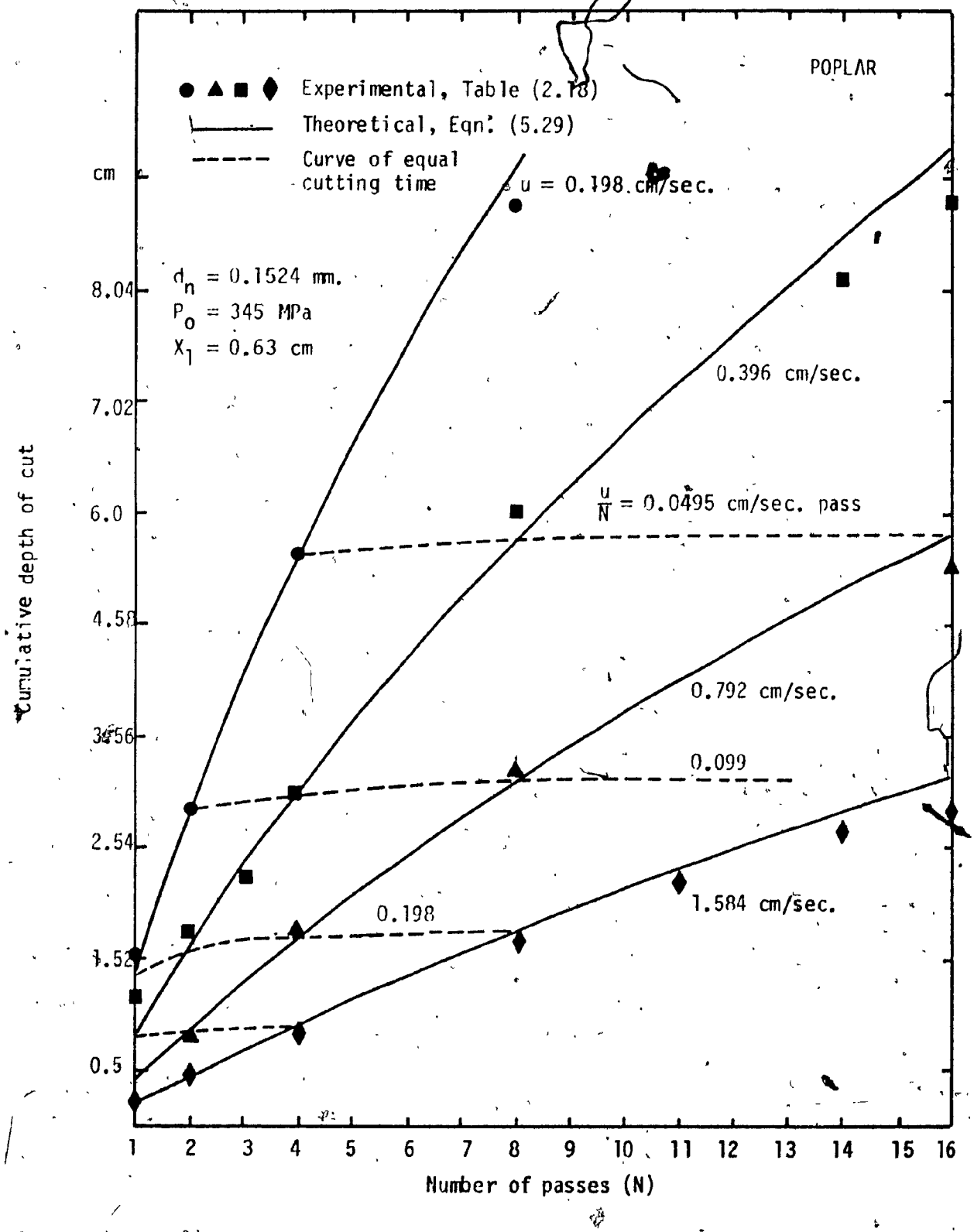

Fig. 5.20 Theoretical and Experimental Results of Multipass Cutting of Poplar.

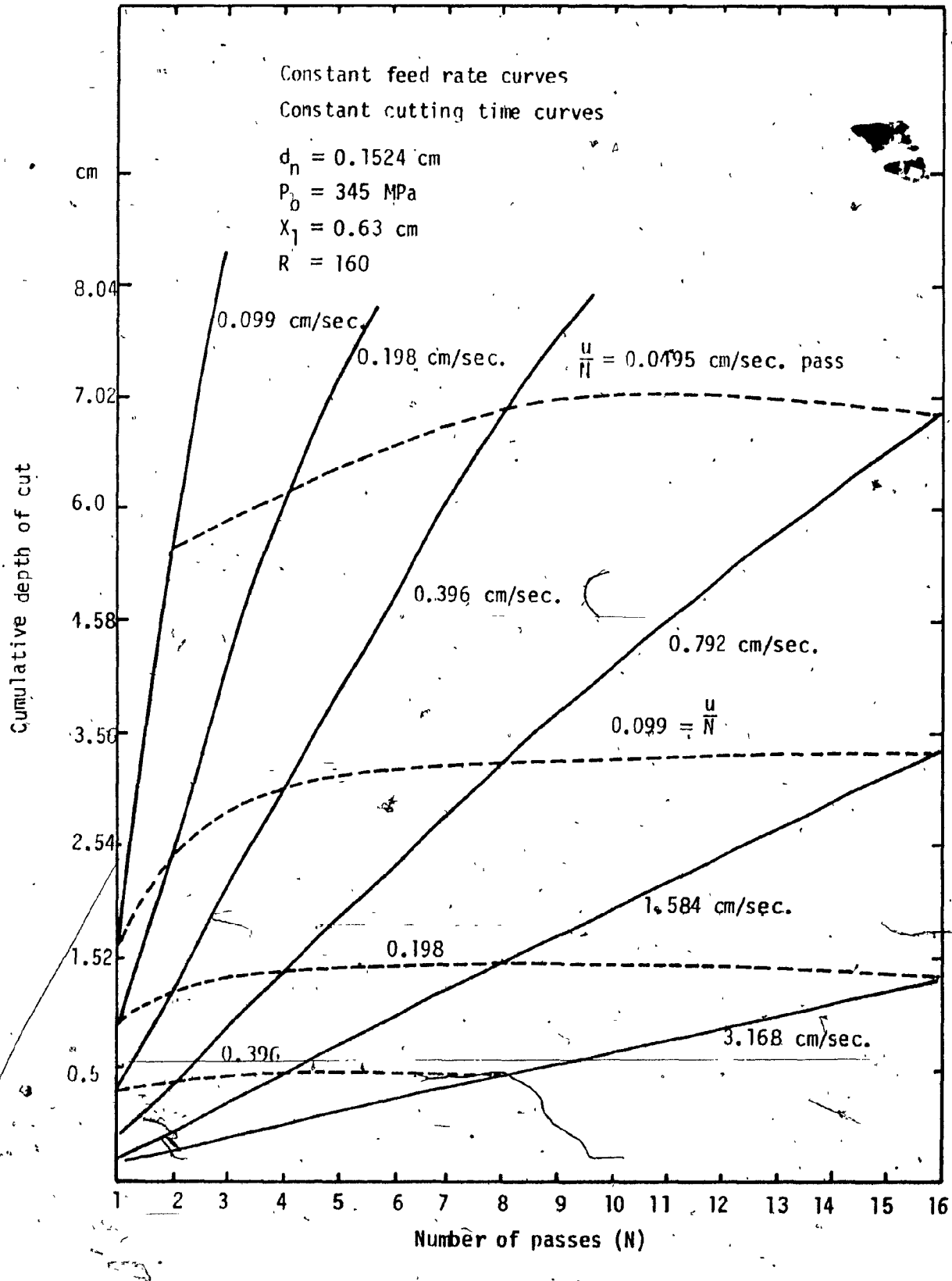

Fig. 5.21 Expected Multipass Cutting Results of Poplar.

Fig. 5.22 compares theoretical and experimental results for coal (27). Agreement is good for low feed rates where experimental data are observed to be consistent. Higher feed rate data are not consistent as shown in Table 2.19, so that no valid comparison can be made for these data.

5.7 CONCLUSIONS

In summary, the findings of Chapter 5 are;

1. Nondimensional equations have been developed to explain quantitatively the effect of stand off distance on cutting results. Critical numbers were defined to explain qualitatively the effect of these numbers over ranges of values found in typical cutting applications.
2. For materials and conditions where the compressive strength number $sC \geq 0.5$, there is no optimum stand off distance for depth of cut or volume removal.
3. The number $C_f P_1/nu$ has two critical limiting values of 2 and 10 that are related to the qualitative behaviour of stand off distance on depth of cut. For $C_f P_1/nu < 2$, there is no optimum stand off distance. For $C_f P_1/nu \geq 10$, the rate of change of depth of cut is independent of the values of $C_f P_1/nu$.
4. The number $C_f P_1/nu$ has two critical limiting values of 1 and 100 that are related to the qualitative effect of stand off distance

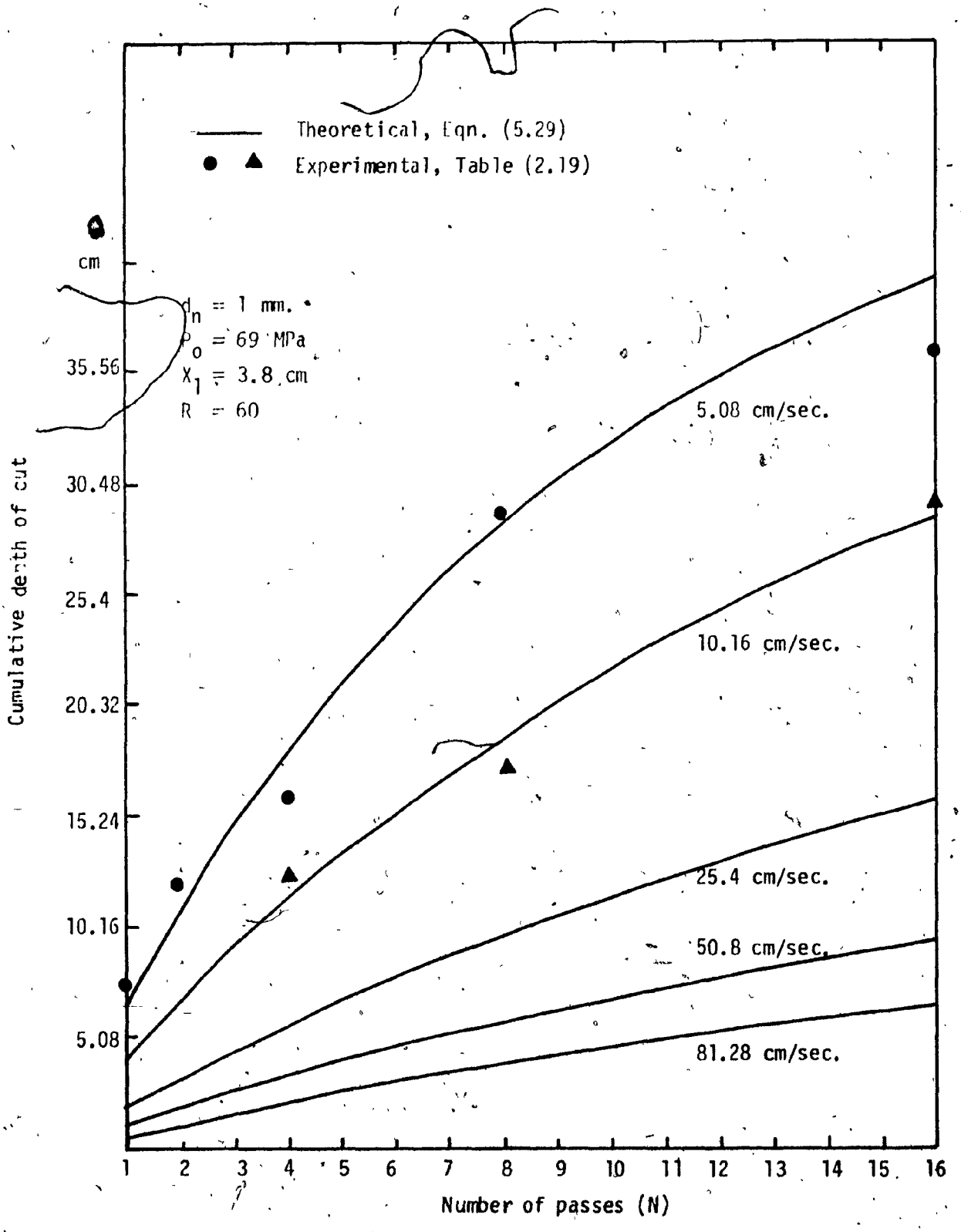

Fig. 5.22 Comparison of Experimental Results Of Multipass Cutting of Coal, Ref. (27) and Theoretical Results from Equation (5.29).

on volume removal in a similar way to that mentioned in item 3.

5. For cleaning and mining applications which require minimum specific energy values, the most efficient volume removal occurs at the optimum stand off distance and values of $nu/C_f P_1 \geq 10$.

6. It is possible to optimize the feed rate and number of passes for maximum depth of cut for materials with $sY \leq 0.06$ and jets with core lengths $X_c \geq 120\ d_n$. In practical terms, this applies to soft materials such as wood and coherent jets with long core lengths. Within these limiting values, a typical application shows that for the optimum feed rate and number of passes, the depth of cut is 70% greater than a single pass depth of cut made in the same total elapsed time.

CHAPTER 6

THEORETICAL ANALYSIS OF THE EFFECT OF FEED RATE AND PULSATING JETS ON THE CUTTING EQUATIONS PHASE IV

6.1 INTRODUCTION

At large distances from the nozzle exit, air friction causes the jet to break into drops as can be seen from Fig. 2.19. The fracture mechanism of materials subjected to the jet in this region will be due to multiple drop impact associated with erosion and fatigue mechanisms. The mechanics of material erosion by single and multiple drop impact has been widely investigated experimentally and semitheoretically. In this chapter the theoretical equations of the previous chapters are extended to very high feed rates to simulate erosion by impact of liquid drops. The conclusions are presented without experimental verification which is beyond the scope of this study.

6.2 THE EFFECT OF FEED RATE ON MODES OF FRACTURE

It was shown in Chapter 4 that the mechanical response of many materials can be represented by an idealized model of springs and dashpots. The Bingham model was used to represent flow of material under the high hydrodynamic forces imposed on it by the water jet. The stress-strain relationship for the Bingham model (Fig. 4.2.c) is,

$$\varepsilon = \frac{\sigma}{E} \qquad \sigma < \sigma_y$$

$$\varepsilon = \frac{\sigma-\sigma_y}{\eta_{ss}} + \frac{\sigma}{E} \qquad \sigma > \sigma_y \qquad (6.1)$$

Equation (6.1) can be rewritten as

$$\frac{E\,\Delta\varepsilon}{\Delta t} = \frac{\Delta(\sigma-\sigma_y)}{(\eta_{ss}/E)} + \frac{\Delta\sigma}{\Delta t} \qquad (6.2)$$

in which Δt, $\Delta\sigma$ and $\Delta\varepsilon$ are finite elements of time, stress and strain respectively. Two cases must be considered depending on the loading time Δt (36):

1- If the loading time $\Delta t \ll \frac{\eta_{ss}}{E}$, then the first term on the right hand side of Eqn. (6.2), can be neglected and brittle fracture can be expected if stresses reach ultimate strength values. The loading time in the case of jet cutting is $\Delta t = d_n/u$, and the feed rate (u) that will result in fracture should be

$$u \gg d_n \frac{E}{\eta_{ss}} \qquad (6.3)$$

2- If the loading time $\Delta t \gg (\eta_{ss}/E)$, the second term on the right hand side of Eqn. (6.2) can be neglected and the case of material flow as discussed in Chapter 4 is obtained. The feed rate condition for this case is

$$u \ll d_n \frac{E}{\eta_{ss}} \qquad (6.4)$$

The quantity (η_{ss}/E) is known as the time constant and it is a very small fraction of a second. Unfortunately, there are no published data for η_{ss} for different materials based on certain characterizing rheological models.

An alternative way of determining the limiting values of feed rate for different modes of fracture is to find the initial penetration rate $\dot{z}_i$ from Eqn. (4.15) by differentiation and

substituting $t = 0.0$. The result is

$$\dot{z}_i = \left(1 - \frac{\sigma_y}{\rho V^2}\right) \left(\frac{\rho V}{\eta}\right) V \qquad (6.5)$$

In Eqn. (6.5), V is used instead of V_1 because the equation is valid at any location along the jet.

For high feed rates, the depth of cut can be found from the linear relationship

$$z = \dot{z}_i t = \left(1 - \frac{\sigma_y}{\rho V^2}\right) \left(\frac{\rho V}{\eta}\right) V.t$$

where

$$t = d_n/u$$

This equation can be rewritten in the nondimensional form

$$\frac{z}{d_n} = \left(1 - \frac{\sigma_y}{\rho V^2}\right) \left(\frac{\rho V}{\eta}\right) \left(\frac{V}{u}\right) \qquad (6.6)$$

when the feed rate u is much higher than $\dot{z}_i$, brittle fracture can be expected. The initial penetration rate for different materials has been calculated in Table 6.1 from properties listed in Table 4.2 at a jet velocity of 457 m/sec (1500 fps).

Material	Ref. No.	$\dot{z}_i$		Material	Ref. No.	$\dot{z}_i$	
		fps.	m/sec.			fps.	m/sec.
Maple	author	0.29	0.088	Red Woolten	(25)	103.9	31.6
Elm	author	0.207	0.063	Concrete	(22)	3.11	0.948
Poplar	author	0.396	0.12	Polycarbonate	(12)	1.459	0.447
Sugar Maple	(1)	1.119	0.341	White Granite	(23)	3.02	0.92
Indiana Limestone	(18)	11.90	0.341	Wilkeson S.S.	(23)	2.613	0.796
Coal	(2)	590	180	Ice	(24)	200.2	61.0
Coal	(20)	39.6	12	Limestone	(19)	8.39	2.55

Table 6.1 Initial penetration rate for different materials at V = 457 m/sec (1500 fps)

In the following section, the dominant fracture mechanism at very high feed rates ($u >> \dot{z}_i$) is presented.

6.2.1 Fracture at Very High Feed Rates

The damage of material by liquid jets when the feed rate is very high is similar in principle to the damage of material by the erosion mechanism of liquid drop impact. The compressible stage of loading at the very beginning of impact has been neglected in the previous analysis of Chapter 4 because its duration time is much shorter than the duration of the subsequent hydrodynamic loading stage. In this section, the compressible loading stage is considered. The model of fracture by liquid drop impact which was suggested by Olive (48) is shown in Fig. 6.1a in which only an elastic wave was assumed to propagate in the solid material upon impact. Continuity of the solid material was assumed inspite of the fact that damage occurs. In Olive's (48) analysis, the pit depth (δ) caused by the impact of the liquid drop with velocity V is

$$\delta = \frac{V}{1 + S \frac{C_e}{C_\ell}} \frac{2.d_d}{C_\ell} \qquad (6.7)$$

Eqn. (6.7) was modified (48) by nondimensional analysis and empirical constants to agree with experimental results. This indicates that the original model on which Eqn. (6.7) was based is not satisfactory. Improved models of the liquid impact as presented in Figs. 6.1b,c are used in the following analysis which is based on the following assumptions:

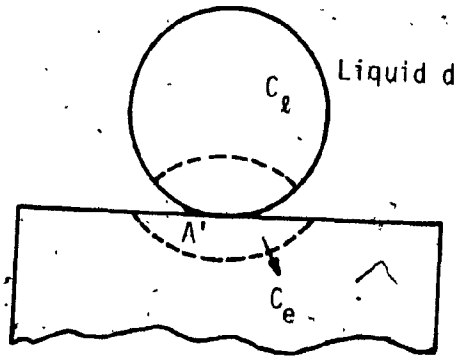

(a)

Impact of liquid drop on a solid surface from Ref. (48)

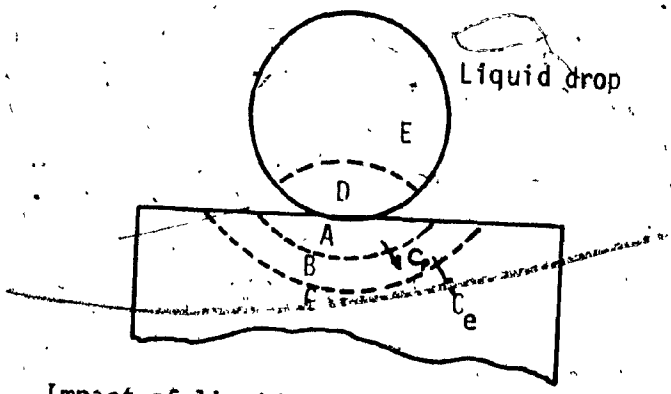

(b)

Impact of liquid drop on a solid surface resulting in plastic deformation

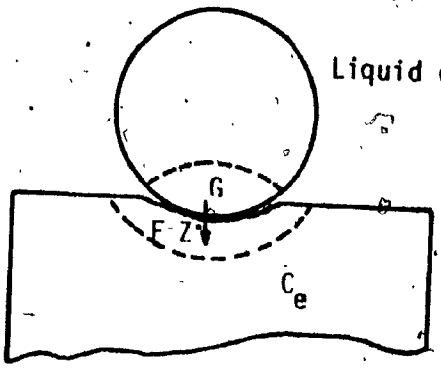

(c)

Impact of a liquid drop on a solid surface resulting in fracture

Fig. 6.1 Models of Erosion Damage by Drop Impact.

1- The effect of the lateral flow of the jet is neglected

2- The pressure is uniform over the liquid-solid interface

3- The wave propagation is one dimensional (plane waves)

4- The effect of reflected waves from solid boundaries is neglected.

Analysis:

When a liquid drop or cylindrical column moving at a velocity V hits a stress free semi-infinite solid, the solid particles in the vicinity of impact (zone A, Fig. 6.1b) attain a certain velocity v_A. A shock wave propagates in the liquid with velocity C_ℓ and brings the pressure in zone D behind the wave front to a value σ which is also the stress in zone A. Hence,

$$\sigma = \rho\, C_\ell\, (V - v_A) \qquad (6.8)$$

where $V - v_A$ is the change in liquid particles velocity in region D. At the same time, the following situations may arise in the solid material depending on the magnitude of the particle velocity v_A:

a - Elastic deformation can occur as long as the stress σ in zone A (Fig. 6.1a) is below the dynamic yield strength of the material, σ_{yd}. The particle velocity v_A in this case cannot exceed the value,

$$v_A = \frac{\sigma_{yd}}{\rho_m\, C_e} \qquad (6.9)$$

The drop velocity, V, that will result in this situation can be found by solving Eqns (6.8) with $\sigma = \sigma_{yd}$ and (6.9).

$$V = \frac{\sigma_{yd} (Z_e + Z_\ell)}{Z_e Z_\ell} \qquad (6.10)$$

where $Z_e = \rho_m C_e$ solid acoustic impedance

$Z_\ell = \rho_\ell C_\ell$ liquid acoustic impedance

For drop velocities higher than that given by Eqn. (6.10), one of the following situations may occur.

b - Elastic-plastic deformation. In this case, two waves propagate simultaneously in the solid material Fig. 6.1b. The first is the elastic wave with velocity C_e followed by the second, which is the plastic wave with velocity C_p. C_p is less than C_e and is a function of the stress level at the point of impact. Between zones A and B Fig. 6.1b, an incremental change in particles velocity dv occurs because of the change in stress level, $d\sigma$. The value of dv is found from the relationship

$$dv = \frac{d\sigma}{\rho_m C} \qquad (6.11)$$

The velocity of propagation, C, of the stress wave, σ, is

$$C = \sqrt{\frac{d\sigma/d\varepsilon}{\rho_m}} \qquad (6.12)$$

Fig. 6.2a is a stress-strain diagram for an actual material; the value $d\sigma/d\varepsilon$ is a function of the stress σ after the yield point. Fig. 6.2b is a bilinear approximation (49) for the stress-strain relation in which the value $d\sigma/d\varepsilon$ is constant in both elastic and plastic regions. Consequently, the velocity of plastic wave propagation has a unique value C_p that can be used in Eqn. (6.11) which is rewritten,

$$\sigma_A - \sigma_B = \rho_m C_p (v_A - v_B) \qquad (6.13)$$

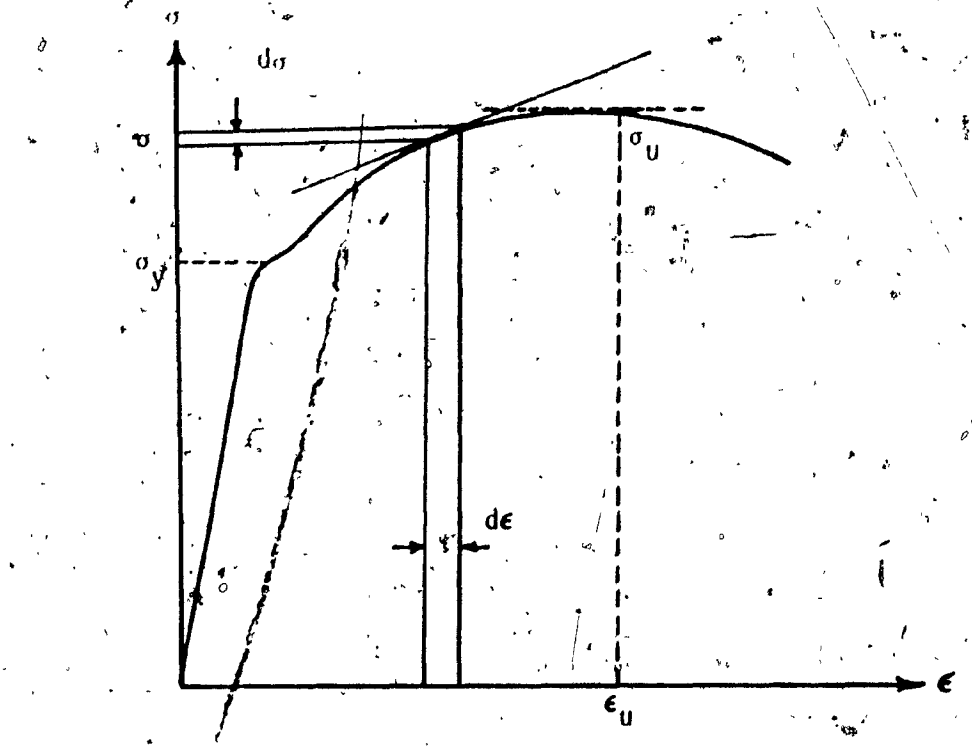

a - actual material

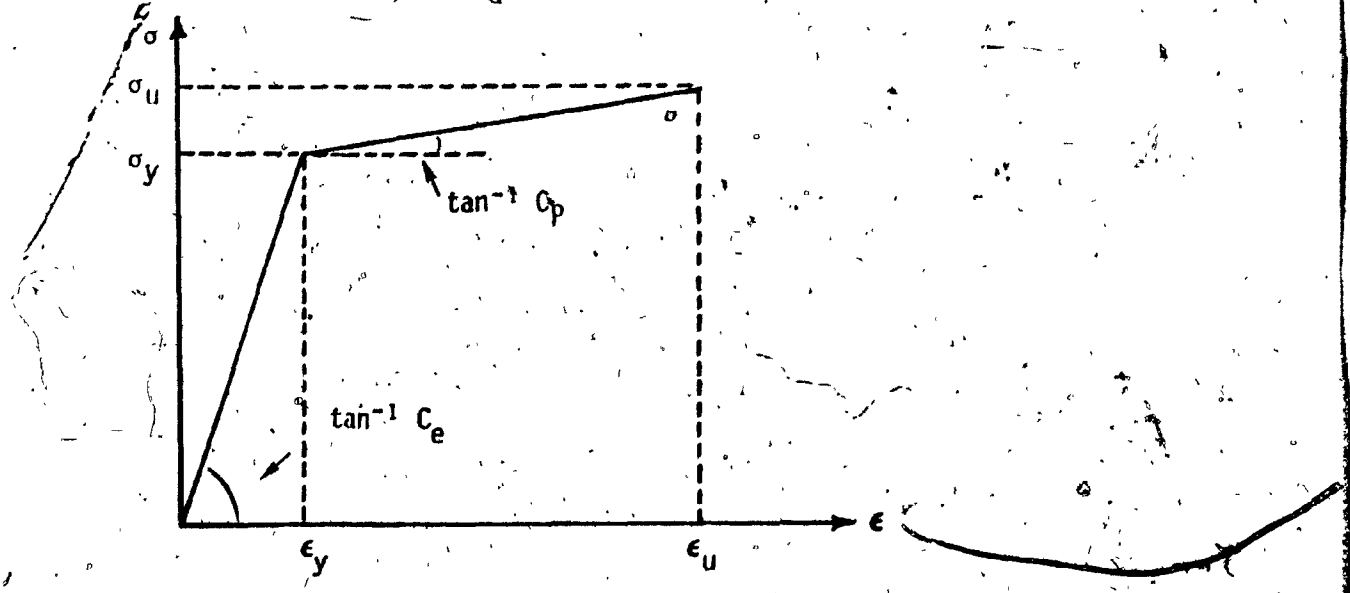

b - bilinear material

Fig. 6.2 Stress Strain Diagrams.

The velocity v_B of the particles in region B is given by

$$v_B = \frac{\sigma_{yd}}{\rho_m C_e} \tag{6.14}$$

where the stress σ_B in region B equals σ_{yd}. The stress σ_A in Eqn. (6.13) equals the stress σ (or pressure) in region D of the liquid drop. The drop velocity, V, and the particle velocity, v_A, are obtained by solving Eqns. (6.8), (6.13) and (6.14).

$$V = \sigma \left(\frac{1}{Z_p} + \frac{1}{Z_\ell}\right) + \sigma_{yd} \left(\frac{1}{Z_e} - \frac{1}{Z_p}\right) \tag{6.15}$$

$$v_A = \frac{\sigma}{Z_p} + \sigma_{yd} \left(\frac{1}{Z_e} - \frac{1}{Z_p}\right) \tag{6.16}$$

where $$Z_p = \rho_m C_p$$

Eqn. (6.16) can also be derived from Eqn. (6.11) and the bilinear stress-strain diagram Fig. 6.2b

$$v_A = \int_0^{v_A} dv = \int_0^{\sigma_{yd}} \frac{d\sigma}{\rho_m C_e} + \int_{\sigma_{yd}}^{\sigma} \frac{d\sigma}{\rho_m C_p}$$

Impact of liquid drops with velocity V causes plastic deformation as long as σ is less than the ultimate dynamic strength σ_u. The critical impact velocity V_c can then be found by substituting σ_u for σ in Eqn. (6.15).

$$V_c = \sigma_u \left(\frac{1}{Z_p} + \frac{1}{Z_\ell}\right) + \sigma_{yd} \left(\frac{1}{Z_e} - \frac{1}{Z_p}\right) \tag{6.17}$$

The critical particle velocity v_{AC} which is the required particle velocity for material damage (erosion) is found from Eqn. (6.16) and $\sigma = \sigma_u$,

$$v_{AC} = \frac{\sigma_u}{Z_p} + \sigma_{yd} \left(\frac{1}{Z_e} - \frac{1}{Z_p}\right) \tag{6.18}$$

Impact velocities higher than V_c will result in material erosion as treated in the following section

c - Material damage (erosion). The model of material damage by liquid drop impact is shown in Fig. 6.1c in which the material is penetrated by the liquid drop at a velocity $\dot{z}$. The particle velocity v_A cannot exceed the maximum critical value v_{AC} without damaging the material. The material particles attain the maximum critical particle velocity $v_c = v_{AC}$ at a rate $\dot{z}$ and the stress increment, σ, in region F (Fig. 6.1c) is

$$\sigma = \rho_m \dot{z} v_c \tag{6.19}$$

The stress (or pressure) in region G of the liquid drop (Fig. 6.1c) is

$$\sigma = \rho C_\ell (V - \dot{z}) \tag{6.20}$$

The velocity $\dot{z}$ rather than the particles velocity v_c is used in Eqn. (6.20) because $V-\dot{z}$ is the actual change in the velocity of liquid particles in region G. The value of $\dot{z}$ is obtained by solving Eqns (6.19) and (6.20)

$$\dot{z} = \frac{V}{1+s\frac{v_c}{C_\ell}}, \quad V > V_c \tag{6.21}$$

The liquid drop remains at the "water hammer" pressure, σ, for a certain time Δt given by

$\Delta t = \frac{2d_d}{C_\ell}$ for a liquid drop of diameter d_d

$\Delta t = \frac{d_j}{C_\ell}$ for a liquid jet of diameter d_j

This is the time required by the shock wave to travel forward and backward from the point of impact to the free surface of the liquid. The pit depth, δ, can be then calculated from

$$\delta = 2 \Delta t$$

i.e.

$$\delta = \frac{V}{1+s\frac{v_c}{C_\ell}} \cdot \Delta t \ , \quad V > V_c \qquad (6.22)$$

This equation differs from equation 6.7 because it uses v_c instead of the velocity of elastic wave propagation, C_e, and it holds only for $V > V_c$.

Table 6.2 compares predictions from Eqn. (6.22) with Olive's (48) experimental results for erosion of aluminum and copper by mercury drops. The predicted pit depths deviates from the experimental results by about 18%. The dynamic strength properties which are needed to calculate the particle critical velocity v_c (Eqn. (6.18)) are not available (49), (50), (51), (52). However, a value of v_c=60 m/sec. was assumed for both aluminum and copper (49). The liquid shock wave velocity, C_ℓ, calculated for mercury drops is 1390 m/sec. Other properties are shown in Table 6.2.

Material	V m/sec.	d_d cm	δ exp. (48)	δ equation 6.22	mean % deviation
Copper	300	0.15	0.04	0.044	
	400	0.15	0.064	0.06	+ 13%
s = 8.92	600	0.15	0.11	0.089	- 16%
	700	0.15	0.14	0.104	
	300	0.1	0.025	0.029	
Aluminium 1100	400	0.1	0.071	0.05	
	500	0.1	0.1	0.064	
s = 2.713	600	0.1	0.125	0.077	- 27%
	250	0.285	0.1	0.09	
	500	0.15	0.14	0.096	

Table 6.2 Comparison of experimental (48) & theoretical results (Eqn. 6.22)

Predicted values from Eqn. (6.22) are in good agreement with test data for copper but are lower than the experimental results for the "softer" material (aluminum). A probable reason is that equation 6.22 does not include the additional penetration during the incompressible stage of impact which follows the compressible stage of impact.

For materials moving with a feed rate $u \gg \dot{z}_i$ under a high velocity water jet of diameter d_n, there are two actions, compressible and incompressible impact. The duration of the compressible stage is $\frac{d_n}{C_\ell}$ and the duration of the incompressible stage is $d_n/u - d_n/C_\ell$ which can be approximated by d_n/u since $C_\ell \gg u$. The total depth of cut z_t is the summation of Eqns (6.6) and (6.22). In nondimensional form, the combined equation is

$$\frac{z_t}{d_n} = \left(1 - \frac{\sigma_y}{\rho V^2}\right)\left(\frac{\rho V}{\eta}\right)\left(\frac{V}{u}\right) + \frac{M}{1+s\frac{v_c}{C_\ell}} \qquad (6.23)$$

where M is the Mach number, V/C_ℓ.

The higher critical feed rate can be determined from Eqn. (6.23) by assuming a maximum allowable error in calculating z_t if the compressible impact is neglected. If this maximum allowable error is 10%, then, the first term on the right hand side of Eqn. (6.23) should be nine times the second term on the right hand side (which accounts for the compressible stage of impact). Consequently, the feed rate u_H that satisfies this condition is

$$u_H = \left(1 - \frac{\sigma_y}{\rho V^2}\right)\left(\frac{\rho V}{\eta}\right)\left(\frac{C_\ell + sv_c}{9.0}\right) \qquad (6.24)$$

For feed rates lower than u_H, the compressible stage of impact can be neglected with less than 10% error in depth of cut prediction from

Eqn. (6.6). Approximate values of u_H are shown for some materials in Table 6.3. The values are based on results of Table 4.2 at a jet velocity of 609 m/sec. (2000 fps). Also, values of (sv_c) are negligible in relation to C_ℓ for the light and soft materials considered.

Material	Ref.	u_H equation 6.24	
		in/sec.	cm/sec.
Poplar	author	2.3	5.8
Maple	author	1.66	4.2
Elm	author	1.19	3.02
Coal	20	188	477
Concrete	22	14.7	37
Wilkenson sand stone	23	12.39	31.4
Lime stone	19	39.79	101

Table 6.3 Approximate values of the higher critical feed rate for some materials at V = 609 m/sec. (2000 fps)

Materials with higher specific gravities and dynamic strength properties such as metals will have lower values of u_H (less than 1.0 inch/sec. at V = 2000 fps). This offers a probable explanation, why Franz's (7) data on aluminum cutting (Table 2.17) does not agree with the theoretical prediction of Eqn. (5.13). Eqn. (6.23) is the appropriate equation with which to compare Franz's data.

6.2.2 The Lower Critical Feed Rate

The flow of material under the jet hydrodynamic stresses is terminated when the stress equals the compressible strength of the material. For very low feed rates, this situation may occur and

further lowering of feed rate will not improve the depth of cut which has a maximum value given by Eqn. (4.18), namely

$$z_o = \frac{1 - \frac{\sigma_c}{\rho V^2}}{\frac{2C_f}{(\frac{}{\sqrt{\pi}})}}$$

The feed rate that will produce z_o is the lower critical feed rate u_L which can be found by solving Eqns. (4.18) and (4.15)

$$u_L = \frac{(\frac{2\ C_f}{\sqrt{\pi}}) \cdot (\frac{\rho V^2}{\eta})}{\log_e (\frac{\rho V^2 - \sigma_y}{\sigma_c - \sigma_y})} \qquad (6.25)$$

Feed rates below u_L will probably result in chip formation type of mechanism of cut similar to the conventional cutting mechanism where material slips on maximum shear planes. The maximum depth of cut achieved by this mechanism is $dn/2$ at the leading edge of the workpiece since the maximum shear plane will be at 45^o from the jet flow direction.

6.3 PULSED JETS

Pulsed water jets have been the subject of many theoretical and experimental investigations (53), (54), (55), (56), (57), (58). They have been applied to rock and coal cutting (59), (60), (61). The short duration release of high pressure energy results in high jet velocities which can do more damage to the material than a jet of longer duration with the same energy. However, an efficient pulsed system must operate at high frequencies which is beyond the capability of present equipment design technology.

The mechanism of penetration of solids by pulsed jets can be divided into two stages:

1- Erosive damage during the compressible impact stage of the jet

2- Material flow under the high hydrodynamic stress (similar to that of Chapter 4) during the incompressible stage of impact that follows the first stage.

The interaction betwcen the pulsed jet and the solid material may occur in one of the two following ways:

1- Penetration of a semi-infinite medium as in drilling applications

2- Penetration of the material on the edge of the kerf. In this case, synchronisation of feed rate and the pulse frequency is required. Fig. 6.3 illustrates the two cases.

6.3.1 Penetration of a Semi-infinite solid by a jet pulse.

When a cylindrical column of liquid (jet pulse) with diameter d_n and length ℓ_t and moving with velocity V, hits a solid material, a total penetration depth z_t results due to different mechanisms of impact. If δ is the pit depth resulting from the first stage of impact and z_s is the depth of cut resulting from the second stage of impact, then, the total depth of cut z_t is

$$z_t = \delta + z_s \qquad (6.26)$$

The pit depth δ requires a jet length ℓ_s and the depth of cut z_s requires a jet length ℓ_s. The total jet length ℓ_t is

$$\ell_t = \ell_\delta + \ell_s$$

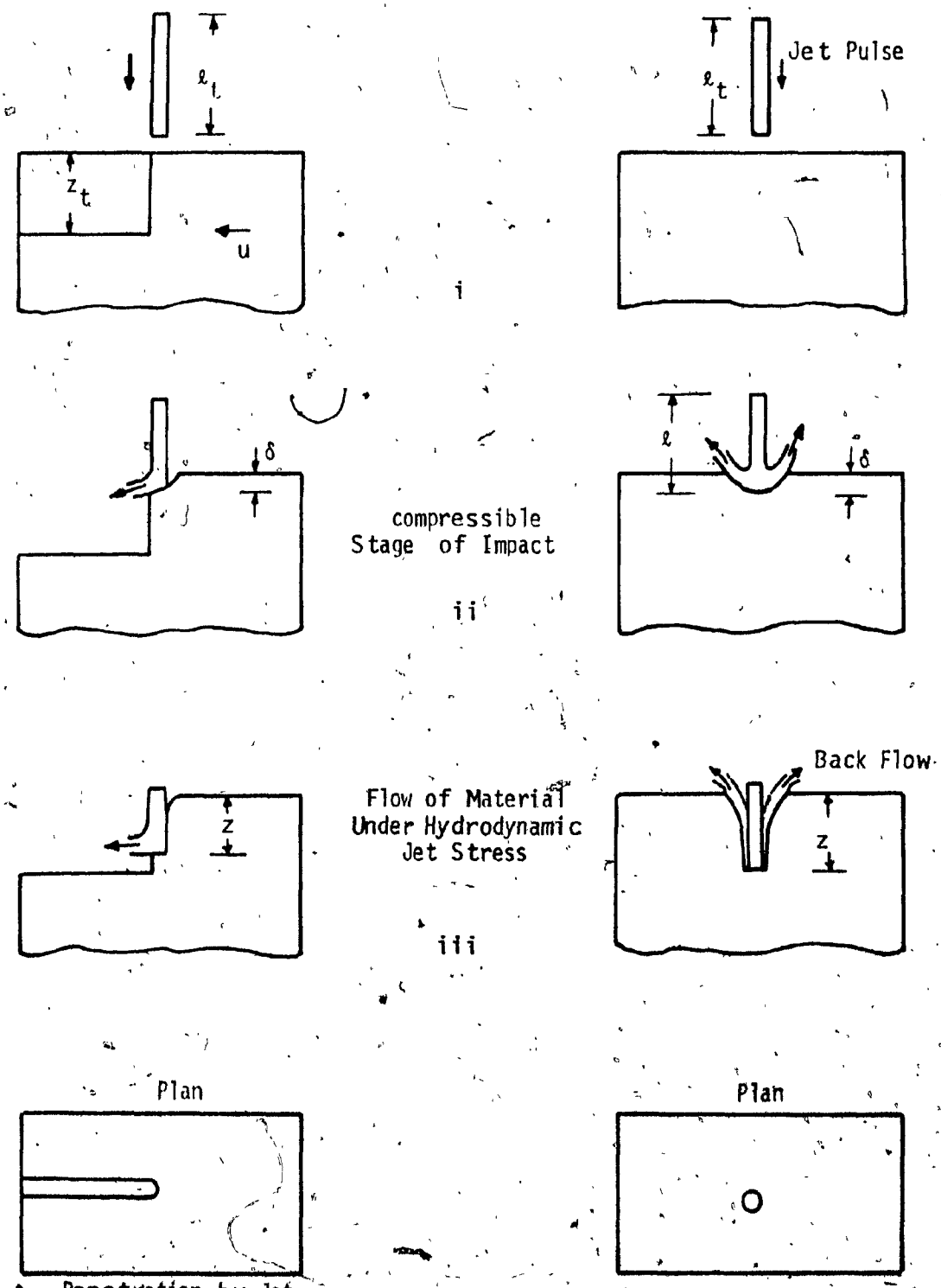

a - Penetration by Jet Subjected to Wall Friction.

b - Penetration of Semi-infinite Solid.

Fig. 6.3 Stages of Fracture and types of Liquid-Solid Interaction.

The penetration rate $\dot{\delta}$ during the first stage of impact is related to the time duration of this stage $t_\delta = d_n/C_\ell$ and the jet length ℓ_δ by the relationship

$$t_\delta = \frac{\ell_\delta}{V - \dot{\delta}} \tag{6.28}$$

The penetration rate $\dot{\delta}$ equals $\dot{z}$ in Eqn. (6.21). The jet length can then be found by solving Eqns. (6.21) and (6.28).

The result is written in the nondimensional form:

$$\frac{\ell_\delta}{d_n} = M \left(1 - \frac{1}{1+s\,\frac{v_c}{C_\ell}}\right) \tag{6.29}$$

where M is the Mach number, V/C_ℓ.

To determine the depth z_s and the corresponding jet length ℓ_s, the jet velocity is assumed to decay similarly to a free submerged jet (Fig. 6.4). The velocity decay in the main region of a free submerged jet is given by the following relationship: (33), (39), (61)

$$V_z = K_j \frac{d_n V}{z} \tag{6.30}$$

where V_z is the jet velocity at distance $z > X_c$ from the solid surface (Fig. 6.4). K_j is constant and equals 6.4 for free submerged jet (33), (39), (61). The additional friction due to the contraction of the flow passage and the effect of back flow shown in Fig. 6.4 will lower the value of K_j in this case. The resistance F_1 of the assumed Bingham substance equals the jet force F_2, as discussed in Chapter 4, where,

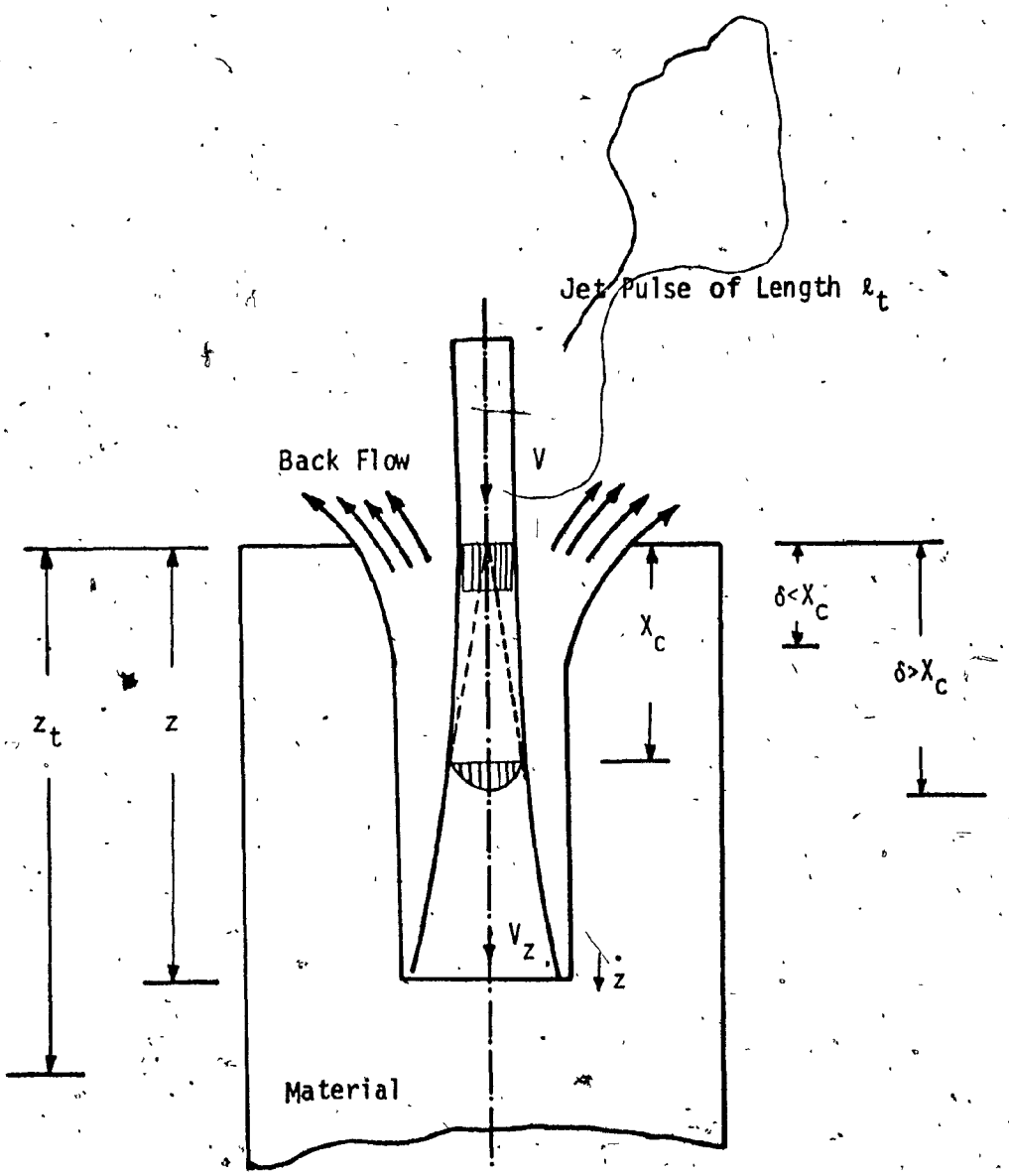

Fig. 6.4 Parameters of Penetration of Semi-infinite Solid.

$$F_1 = \eta A_c \dot{z} + \sigma_y A_c \qquad (6.31)$$

$$F_2 = \rho A_c (V_z - \dot{z})^2 \qquad (6.32)$$

$\dot{z}$ is the penetration rate in the second stage of penetration. The penetration rate $\dot{z}$ is obtained by simultaneous solution of Eqns. (6.30), (6.31), and (6.32), $\dot{z} << V_z$, in Eqn. (6.32),

$$\dot{z} = \frac{K_j^2 \rho V^2 d_n^2 - \sigma_y z^2}{\eta z^2} \qquad (6.33)$$

A small element of the jet $d\ell$ produces a depth dz in time dt at a rate $\dot{z}$, where

$$dt = \frac{d\ell}{V - \dot{z}} \qquad (6.34)$$

To relate the depth of cut to the jet length ℓ, Eqns. (6.33) and (6.34) are solved together. The result is

$$\int \frac{\eta z^2 V - K_j^2 \rho V^2 d_n - \sigma_y z^2}{K_j^2 \rho V^2 d_n - \sigma_y z^2} dz = \int d\ell \qquad (6.35)$$

The limits of integration in Eqn. (6.35) depend on whether δ, the pit depth, is greater or less than X_c, the core length.

a - $\delta > X_c$. In this case, the penetration during the incompressible stage of impact corresponds to the main region of the submerged jet. Eqn. (6.35) can, then, be rewritten with the integration limits:

$$\int_{\delta}^{z_t} \frac{\eta z^2 V - K_s^2 \rho V^2 d_n - \sigma_y z^2}{K_j^2 \rho V^2 d_n - \sigma_y z^2} dz = \int_{\ell_\delta}^{\ell_t} d\ell = \ell_s \qquad (6.36)$$

2. The spreading behaviour of high pressure jets with polymer are adequately described by existing equations for low pressure incompressible jets.

3. The wood cutting studies of Chapter 3 resulted in formulation of a cutting equation in which the dominant properties are a mean strength value and the dry and wet specific gravities of the wood.

4. The theoretical analysis of Chapter 4 shows that the dominant material properties that affect cutting results are the compressive yield and fracture strengths, the hydrodynamic solid-liquid coefficient of friction and the damping factor which has been determined experimentally for some materials.

5. The functional relationship between depth of cut, feed rate and dominant material properties that has been derived is in good agreement with different cutting results and satisfies the limiting conditions of jet cutting processes. The comparison is based on assumed values of jet spreading behaviour where published data do not contain the necessary information.

6. The optimum stand off distances for maximum depth of cut and maximum volume removal (minimum specific energy) have been determined as functions of nondimensional jet and material characteristics as described in Sections 5.2 and 5.3.

7. For a material to be cut in a specified time, the maximum depth of cut can be achieved by adjusting the feed rate and number of passes. Quantitative relationships are presented in Section 5.5.

8. The specific energy has been found to have its lowest values above certain critical feed rates when all other parameters are kept constant. This suggests that oscillating jets with certain minimum frequencies should be used for descaling and mining applications where maximum volume removal is required at low costs. Numerical values of nondimensional numbers for the choice of optimum conditions are presented in Chapter 5.

9. The theory of steady jets as extended to pulsating jets and impact of liquid drops in Chapter 6 is useful in the following ways:

i - It allows estimation of higher critical feed rate to distinguish between different mechanisms of failure during the compressible and incompressible stages of impact.

ii - It defines the parameters that are related to penetration of solids by a liquid jet pulse for different ways of liquid-solid interaction.

iii - It allows calculation of pit depth obtained by the compressible stage of impact of a jet pulse or the pit depth by a continuous jet at very high feed rates.

REFERENCES

1. Bryan, E.: "High Energy Liquid Jets as a New Concept for Wood Machining". A Dissertation submitted in partial fulfillment of the requirements for the Degree of Doctor of Philosophy in the University of Michigan, 1963.

2. Kinoshita, T., Koshino, K. and Takagi, K.: "Rock Breaking with Continuous High Speed Water Jet System". Proceedings of the Symposium on Jet Cutting Technology, BHRA Fluid Engineering, 1972, pp. B2-13-B2-28.

3. Cooley, W.C.: "Correlation of Data on Jet Cutting by Water Jets using Dimensionless Parameters". Proceedings of the Symposium on Jet Cutting Technology, BHRA Fluid Engineering, 1974, pp. H4-39-H4-48.

4. Cooley, W.C.: "Hydraulic Mining and Excavation". Proceedings of the Symposium on Jet Cutting Technology, BHRA Fluid Engineering, Introductory Course, Lecture No. E, 1976.

5. Matsumoto, K., Hamada, H., Fukuda, T. and Shizyo, A.: "High Pressure Jet Cutting". Proceedings of the Symposium on Jet Cutting Technology, BHRA Fluid Engineering, Paper B4, 1972.

6. Farmer, I.W. and Attewell, P.B.: "Rock Penetration by High Velocity Water Jet". International Journal of Mech. Mining Science, Vol. 2, 1964, pp. 135-153.

7. Frank, N. and Lohn, P.D.: "Fragmentation of Native Copper Ores with Hydraulic Jets". Proceedings of the Symposium on Jet Cutting Technology, BHRA Fluid Engineering, 1974, pp. H3-29-H3-38.

8. Mellor, M.: "Some General Relationships for Idealized Jet Cutting". Proceedings of the Symposium on Jet Cutting Technology, BHRA Fluid Engineering, Paper A2, 1972.

9. Mellor, M.: "Cutting Ice with Continuous Jets". Proceedings of the Symposium on Jet Cutting Technology, BHRA Fluid Engineering, 1974, pp. G5-65-G5-76.

10. Zelenin, A.N., Vesselov, G.M. and Konishin, Y.C.: "Rock Breaking with Jet Stream under Pressure up to 2000 Atm". Problems of Mining, Turpigorev Volume, 1958, pp. 112-122. Translated by Prokopov, C.A., Spokane Office of Mineral Resources and Spokane Office of Mining Research, U.S. Bureau of Mines, Spokane, Washington.

11. Crow, S.C.: "A Theory of Hydraulic Rock Cutting". International Journal Rock Mech. Sci. & Geomech. Abstr., Vol. 10, 1973, pp. 567-584.

12. Mohaupt, U.H. and Burns, D.J.: "Machining Unreinforced Polymers with High Velocity Water Jets". Experimental Mechanics, Vol. 14, No. 3, April 1974, pp. 152-157.

13. Garrett, B. et al.: "Explosives with Lined Cavities". Journal of Applied Physics, Vol. 19, June 1948, pp. 563-582.

14. Bridgman, P.W.: "The Volume of Eighteen Liquids as a Function of Pressure and Temperature". Proceedings of American Academy Arts and Sciences, Vol. 66, 1931, pp. 185-233.

15. Yanaida, K.: "Flow Characteristics of Water Jets". Proceedings of the Symposium on Jet Cutting, BHRA Fluid Engineering, Paper A2, 1974.

16. Leach, S.J. and Walker, G.L.: "The Application of High Speed Liquid Jets to Cutting". Royal Soc. Phil. Trans., London, Vol. 260A, 1966, pp. 295-314.

17. Harris, H.D. and Brierley, W.H.: "Application of Water Jet Cutting". Proceedings of the Symposium on Jet Cutting Technology, BHRA Fluid Engineering, Paper G1, 1972.

18. Harris, H.D. and Mellor, M.: "Penetration of Rocks by Continuous Water Jets". Proceedings 2nd International Symposium on Jet Cutting Technology, BHRA, Cambridge, England, Paper H1, April 1974.

19. Labus, T.J.: "Energy Requirements for Rock Penetration by Water Jets". Proceedings 3rd International Jet Cutting Technology Symposium, BHRA, Chicago, Paper E3, May 1976.

20. Summers, D.A. and Peters, J.F.: "Preliminary Experimentation on Coal Cutting in the Pressure Range 35 to 200 MN/m^2". Proceedings 2nd International Jet Cutting Technology Symposium, BHRA, Cambridge, England, Paper H2, April 1974.

21. Nikonov, P.G. and Goldin, A.Y.: "Coal and Rock Penetration by Fine, Continuous High Pressure Water Jets". Proceedings 1st International Jet Cutting Technology Symposium, BHRA, Conventry, England, Paper E2, April 1972.

22. Northworthy, A.G., Mohaupt, U.H. and Burns, D.J.: "Concrete Slotting with Continuous Water Jets at Pressures up to 483 MPa (70 Ksi)". Proceedings 2nd International Jet Cutting Technology Symposium, Cambridge, England, Paper G3, April 1974.

23. Hurlburt, G.H., Crow, S.C. and Lade, P.V.: "Experiments in Hydraulic Rock Cutting". International Journal Rock Mech. Min. Sci. & Geomech. Abstr., Vol. 12, 1975, pp. 203-212.

24. Calkins, D. and Mellor, M.: "Investigations of Water Jet for Lock Wall Deicing". Proceedings 3rd International Jet Cutting Technology Symposium, BHRA, Chicago, Paper G2, May 1976.

25. Moodie, K. and Arlingstall, G.: "Some Experiments on the Application of High Pressure Water Jets for Mineral Excavation". Proceedings 1st International Jet Cutting Technology Symposium, BHRA, Conventry, England, Paper E3, April 1972.

26. Franz, N.C.: "The Influence of Stand Off Distance on Cutting with High Velocity Fluid Jets". Proceedings 2nd International Jet Cutting Technology Symposium, BHRA, Cambridge, England, Paper B3, 1974.

27. Summers, D.A. and Mazurkiewicz, M.: "The Effect of Jet Traverse Velocity on the Cutting of Coal and Jet Structure". Proceedings 3rd International Jet Cutting Technology Symposium, BHRA, Chicago, Paper D5, May 1976.

28. Kennedy, E.I.: "Strength and Related Properties of Wood Grown in Canada". Department of Forestry Publications, Ottawa, No. 1104, 1965.

29. Koch, P.: "Wood Machining Processes". Ronald, New York, pp. 24-29.

30. Downey, D.B. and Tottle, C.R.: "A Scanning Electron Microscope Study of Water Jet Cut Paper". Proceedings of the Symposium on Jet Cutting Technology, BHRA Fluid Engineering, 1974, pp. C2-19-C2-29.

31. DuPlessis, M.P. and Hashish, M.: "High Energy Water Jet Cutting Equations for Wood". ASME Transactions.

32. Hansen, A.G.: "Fluid Mechanics". Chapters 3 and 4, John Wiley and Sons, New York, 1967.

33. Schlichting, H.: "Boundary Layer Theory". Chapter 21, McGraw-Hill, 1968.

34. Jaeger, J.C. and Cook, N.G.W.: "Fundamentals of Rock Mechanics". Chapter 11, Methuen & Co. Ltd., London, 1969.

35. Jaeger, J.C.: "Elasticity, Fracture and Flow". Chapter 2, Methuen & Co. Ltd., London, John Wiley and Sons, Inc., New York, 1964.

36. McClintock, F.A. and Argon, A.S.: "Mechanical Behaviour of Materials". Addison-Wesley, Reading, Mass., USA, 1966.

37. Kollmann, F.F.P. and Wilfred, A.: "Principals of Wood Science and Technology". Chapter 7, Springer-Verlag New York Inc., 1968.

38. Shavlovsky, D.S.: "Hydrodynamics of High Pressure Fine Continuous Jets". Proceedings 1st International Jet Cutting Symposium, BHRA, Conventry, England, Paper A6, 1972.

39. Abramovich, G.N.: "The Theory of Turbulent Jets". MIT Press, Cambridge, Mass., 1963.

40. Shtuckaturov, K.T. and Kuklin, I.S.: "Basic Factors and Fracturing Ability of Water Jet". Akad. Nauk SSSR, Uralyskiy Filial.3, 1962.

41. Hamada, H., Fukuda, T. and Sijoh, A.: "Basic Study of Concrete Cutting by High Pressure Continuous Water Jets". Proceedings 2nd International Jet Cutting Technology Symposium, BHRA, Paper G2, 1974.

42. Virgil, E. et al.: "Tunnelling, Fracturing, Drilling and Mining with High Speed Water Jets Utilizing Cavitation Damage". Proceedings 1st International Jet Cutting Technology Symposium, BHRA, Paper A3, 1972.

43. Lichtarowicz, A.: "Experiments with Cavitating Jets". Proceedings 2nd International Jet Cutting Technology Symposium, BHRA, Paper D1, 1974.

44. Beutin, E.F., Erdmann, F. and Louis, F.: "Material Behaviour in the Case of High Speed Liquid Attacks". Proceedings 2nd International Jet Cutting Technology Symposium, BHRA, Paper C1, 1974.

45. Beutin, E.F., Erdmann, F. and Louis, F.: "Influence of Cavitation Bubbles in Cutting Jets". Proceedings 2nd International Jet Cutting Technology Symposium, BHRA, Paper D3, 1974.

46. Chermensky, G.P.: "Breaking Coal and Rock With Pulsed Water Jets". Proceedings 3rd International Jet Cutting Technology Symposium, BHRA, Paper D4, 1976.

47. Erdmann-J, F., Hassan, A.M. and Louis, H.: "A Study of the Oscillations Effects on the Cleaning and Cutting Efficiency of High Speed Water Jet". Proceedings 3rd International Jet Cutting Technology Symposium, BHRA, Paper C3, 1976.

48. Olive, G.E.: "P.S. in Metals Caused by Collision with Liquid Drops and Soft Metal Spheres". Journal of Research of National Bureau of Standards, Vol. 62, No. 6, June 1959, pp. 229-246.

49. Johnson, W.: "Impact Strength of Materials". Edward Arnold, London and Crane, Russak New York, 1972.

50. Rinchart, S.J. and Pearson, J.: "Behaviour of Metals under Impulsive Loads". Dover Publications, Inc. New York, 1954.

51. Thiruvengadam, A.: "The Concept of Erosion Strength". Erosion by Cavitation or Impingement, ASTM STP 408, Am. Soc. Testing Mats., 1967, p. 22.

52. Springer, G.: "Erosion by Liquid Impact". Scripta Publishing Co., Washington, D.C., 1976.

53. Edney, B.E.: "Experimental Studies of Pulsed Water Jets". Proceedings 3rd International Jet Cutting Technology Symposium, BHRA, 1976.

54. Mellors, W.; Mohaupt, U.H. and Burns, D.J.: "Dynamic Response and Optimization of a Pulsed Water Jet Machine of the Pressure Extrusion Type". Proceedings 3rd International Jet Cutting Technology Symposium, BHRA, Paper B4, 1976.

55. Chermensky, G.P.: "Experimental Investigation of the Reliability of Impulsive Water Cannons". Proceedings 3rd International Jet Cutting Technology Symposium, BHRA, Paper H1, 1976.

56. Lucke, W.N. and Cooley, W.C.: "Development and Testing of a Water Cannon for Tunnelling". Proceedings 2nd International Jet Cutting Technology Symposium, BHRA, Paper J3, 1974.

57. Wylie, E.B.: "Pipeline Dynamics and Pulsed Jet". Proceedings 1st International Jet Cutting Technology Symposium, BHRA, Paper A5, 1972.

58. Contractor, D.N.: "Application of Fluid Transients to Hydraulic Mining". Journal of Basic Engineering, Trans. ASME, June 1972, pp. 447-454.

59. Moodie, K. and Taylor, G.: "The Fracture of Rocks by Pulsed Water Jets". Proceedings 2nd International Jet Cutting Technology Symposium, BHRA, Paper H7, 1974.

60. Cooley, W.C. and Clipp, L.L.: "High Pressure Water Jets for Undersea Rock Excavation". Trans. ASME, Journal of Engineering for Industry, May 1970, pp. 281-287.

61. Daily, J.W. and Harleman: "Fluid Dynamics". Addison-Wesley Publishing Co. Inc., Reading, Mass., U.S.A., 1966.

62. Nikonov, G.P.: "Research into the Cutting of Coal by Small Diameter High Pressure Water Jets". Dynamics of Rock Mechanics, Soc. of Mining Engineers, New York, 1971.

APPENDIX A

$$\frac{\partial}{\partial t}\int_{c.v.} \rho dV = -\int_{c.s.} \rho V_{r.n}\, dA$$

can be written as

$$\frac{d}{dt}\left[\rho_m V_{c.v}\right] = -\int_{c.s} \rho V_{r.n}\, dA = -\left[\rho_2 A_2 V_2 - \rho_1 A_1 V_1\right]$$

Neglecting density changes due to frictional heating and substituting $V_{c.v} = A_c z$

$$\frac{d}{dt}\left[\rho A_c z\right] = -\rho A_2 V_2 + \rho A_1 V_1$$

$$\rho A_c \dot{z} = -\rho A_2 V_2 + \rho A_1 V_1$$

after assuming A_c = constant, $\dot{z} = W$

$$\rho A_2 V_2 = \rho A_1 V_1 - \rho A_c W$$

$$\dot{m}_{ext} = \rho\left[A_1 V_1 - A_c W\right]$$

Where $\dot{m}_{ext}$ is the exit mass flow rate from the control volume

APPENDIX B

AVERAGE STAGNATION PRESSURE ACROSS JET WIDTH

a - The Main Region of the Jet

The average pressure $P_{av.}$ is obtained from

$$P_{av.}\ \pi\ b_m^2 = \int_0^{b_m} P.2\pi Y\ dY \qquad (B.1)$$

where $$P = P_m\ (1 - \xi^{3/2})^2 \qquad (B.2)$$

substituting $Y = b_m \xi$, $dY = b_m\ d\xi$ in Eqn. (B.1) and using Eqn. (B.2) for P. The result is

$$P_{av.}\ \pi b_m^2 = \int_0^1 2\pi P_m (1 - \xi^{3/2})^2\ b_m^2\ \xi\ d\xi$$

$$P_{av.} = 2\ P_m \left[\frac{1}{2}\xi^2 + \frac{2}{3.5}\xi^{7/2} + \frac{1}{5}\xi^5\right]_0^1$$

$$= 0.257\ P_m \qquad (B.3)$$

Substituting in Eqn. (B.3) by the value of P_m from Eqn. (5.2):

$$P_{av.} = 0.257\ P_1\ \left(\frac{X_c}{X}\right) \qquad (B.4)$$

b - The Initial Region of the Jet

In this case, the average pressure is calculated from:

(see Fig. 5.1)

$$P_{av}\,\pi(Y_c + b_c)^2 = P_1\,\pi\,Y_c^2 + \int_{Y_c}^{b_c} P.\,2\pi Y\,dY \qquad (B.5)$$

The integral term in Eqn. (B.5) can be found as in the previous case, and equals $0.257\,P_1\,\pi\,b_c^2$, then

$$P_{av}\,\pi(Y_c + b_c)^2 = P_1\,\pi\,Y_c^2 + 0.257\,P_1\,\pi\,b_c^2 \qquad (B.6)$$

i.e. $$P_{av.} = P_1\left(\frac{Y_c^2 + 0.257\,b_c^2}{(Y_c + b_c)^2}\right) \qquad (B.7)$$

The values of Y_c and b_c as functions of X can be determined by using Eqn. (2.19) when $X = X_c$

$$W_{X_c} = 0.335\,\sqrt{d_n\,X_c} \qquad (B.8)$$

Geometric similarity in jet initial region Fig. 5.1 results in

$$\frac{2\,Y_c}{d_n} = \frac{X - X_c}{X_c} \quad \text{i.e.} \quad Y_c = \frac{d_n}{2}\left(\frac{X}{X_c} - 1\right) \qquad (B.9)$$

and $\frac{2b_c}{W_{X_c}} = \frac{X}{X_c}$ using Eqn. (B.8) for W_{X_c}, then

$$b_c = \frac{0.335}{2}\sqrt{d_n\,X_c}\left(\frac{X}{X_c}\right) \qquad (B.10)$$

APPENDIX C

EFFECTIVE JET WIDTH IN THE MAIN REGION

Eqn. (5.4) is rewritten as

$$\xi = (1 - \sqrt{\frac{P}{P_m}})^{2/3} = \frac{Y}{b_m} \qquad (C.1)$$

The effective width is determined by using the relationship

$$P = 0.5\ \sigma_c \qquad (C.2)$$

substituting in Eqn. (C.1) by values of P from Eqn. (C.2) and P_m from Eqn. (5.2). The result is

$$\frac{Y_{eff}}{b_m} = (1 - \sqrt{\frac{\sigma_c}{2P_1} \cdot \frac{X}{X_c}})^{2/3} \qquad (C.3)$$

The jet radius b_m is determined from Eqn. (5.9)

$$b_m = \frac{W}{2} = \frac{0.335}{2} \sqrt{d_n X} \qquad (C.4)$$

solving Eqns. (C.3), (C.4) and $R = X_c\ d_n$. The result is

$$\frac{W_e}{d_n\sqrt{R}} = 0.335 \sqrt{\frac{X}{X_c}} \left[1 - \sqrt{\frac{\sigma_c}{2P_1} \frac{X}{X_c}}\right]^{2/3} \qquad (C.5)$$

where $W_e = 2\ Y_{eff.}$

APPENDIX D

AVERAGE PRESSURE ACROSS JET EFFECTIVE WIDTH

The average pressure (P_a) over the jet effective width is determined from

$$P_a \cdot \pi \cdot Y_{eff}^2 = \int_0^{W_e/2} P \cdot 2\pi Y \, dY \qquad (D.1)$$

substituting for P from Eqn. (5.3) and putting $Y = b_m \xi$. The result is

$$P_a \cdot \pi Y_{eff}^2 = \int_0^{\xi_e} 2\pi P_m (1 - \xi^{3/2})^2 \, b_m^2 \, d\xi \qquad (D.2)$$

where $\xi_e = Y_{eff}/b_m$ and is given by Eqn. (C.3). The result of integration of Eqn. (D.2) is

$$P_a = 2 \frac{b_m^2}{Y_{eff}^2} P_m \left[0.5 \, \xi^2 - 0.57 \, \xi^{7/4} + 0.2 \, \xi^5\right]_0^{\xi_e} \qquad (D.3)$$

substituting from Eqn. (C.3) for (Y_{eff}/b_m) and from Eqn. (5.3) for P_m in Eqn. (D.3). The result is

$$P_a = \frac{2 \, P_1 \, (X_c/X) \left[0.5 \, \xi^2 - 0.57 \, \xi^{7/4} + 0.2 \, \xi^5\right]_0^{\psi^{2/3}}}{\psi^{4/3}} \qquad (D.4)$$

where $$\psi = \left(1 - \sqrt{\frac{\sigma_c}{2P_1} \frac{X}{X_c}}\right) = \xi_e \qquad (D.5)$$

Reduction of Eqn. (D.4) results in

$$P_a = 2 \, P_1 \left(\frac{X_c}{X}\right) \left[0.5 - 0.57 \, \psi + 0.2 \, \psi^2\right] \qquad (D.6)$$

or $$P_a = P_1 \, \phi \qquad (D.7)$$

where $$\phi = 2 \left(\frac{X_c}{X}\right) (0.5 - 0.57 \, \psi + 0.2 \, \psi^2) \qquad (D.8)$$

APPENDIX E

The depth of cut in Eqn. (4.16) can be expressed in terms of pressure rather than jet velocity by substituting

$$P = \frac{1}{2}\rho V^2$$

The result is

$$z = \frac{\sqrt{\pi}}{2}\frac{d_n}{C_f}\left(1 - \frac{\sigma_y}{2P}\right)\left(1 - e^{-\frac{4}{\sqrt{\pi}}\frac{C_f P}{n u}}\right) \qquad (E.1)$$

The effect of stand off distance on depth of cut can then be seen by substituting P_a for P and w_e for d_n where

$$P_a = P_1 \cdot \phi \qquad \text{from Eqn. (D.7)}$$

$$w_e = 0.335\, d_n\sqrt{R}\,\sqrt{\frac{X}{X_c}}\left[\psi^{2/3}\right] \qquad \text{from Eqns. (C.5) and (D.5)}$$

The result is

$$z = \frac{0.335\sqrt{\pi}}{2}\,\frac{d_n\sqrt{R}}{C_f}\,\left(\frac{X}{X_c}\right)\,\psi^{2/3}\left(1 - \frac{\sigma_y}{2P_1\phi}\right)\left(1 - e^{-\frac{4}{\sqrt{\pi}}\frac{C_f P_1}{n u}\phi}\right) \qquad (E.2)$$

Reducing the numerical values in Eqn. (E.2) and re-arranging; then

$$\frac{z\,C_f}{d_n\sqrt{R}} = 0.297\left(\frac{X}{X_c}\right)\psi^{2/3}\left(1 - \frac{\sigma_y}{2P_1\phi}\right)\left(1 - e^{-2.256\frac{C_f P_1}{n u}\phi}\right) \qquad (E.3)$$

APPENDIX F

Eqns. (6.33) and (6.34) are

$$\frac{dz}{dt} = \frac{K_J^2 \rho V^2 d_n - \sigma_y z}{\eta z^2} \qquad (F.1)$$

$$dt = \frac{d\ell}{V-\dot{z}} \quad \text{i.e.} \quad \frac{d\ell}{dt} = V-\dot{z} \qquad (F.2)$$

Substituting in these equations by the following transformations:

$$Z = \frac{z}{d_n} \qquad \text{i.e.} \qquad z = Z\, d_n$$

$$T = t \cdot \frac{V}{d_n} \qquad \text{i.e.} \qquad t = T\, d_n/V \qquad (F.3)$$

$$L = \ell/d_n \qquad \text{i.e.} \qquad \ell = L\, d_n$$

The result is

$$\frac{dz}{dt} = V \frac{dz}{dT} = \frac{K_J^2 \rho V^2 d_n^2 - \sigma_y Z^2 d_n^2}{\eta (Z\, d_n)^2}, \qquad (F.4)$$

$$V \frac{dL}{dT} = V - V \frac{dZ}{dT} \qquad (F.5)$$

Dividing both sides of Eqns. (F.4) and (F.5) by V and reducing; the result is

$$\frac{dZ}{dT} = \frac{K_J^2 \rho V - \sigma_y Z^2}{\eta Z^2} = K_J^2 \left(\frac{\rho V}{\eta}\right) \frac{1}{Z^2} - \left(\frac{\sigma_y}{\rho V^2}\right)\left(\frac{\rho V}{\eta}\right) \qquad (F.6)$$

$$\frac{dL}{dT} = 1 - \frac{dZ}{dT}$$